ELECTROCATALYTIC WATER SPLITTING WITH PRUSSIAN BLUE ANALOGUES UNDER EXTERNAL STIMULI

A THESIS SUBMITTED TO

THE GRADUATE SCHOOL OF ENGINEERING AND SCIENCE OF BILKENT UNIVERSITY

IN PARTIAL FULFILLMENT OF THE REQUIREMENTS FOR THE DEGREE OF

MASTER OF SCIENCE

IN

CHEMISTRY

By

Waqar Ahmad

September 2023

ELECTROCATALYTIC WATER SPLITTING WITH PRUSSIAN BLUE ANALOGUES UNDER EXTERNAL STIMULI

By Waqar Ahmad

September 2023

We certify that we have read this thesis and that in our opinion it is fully adequate, in scope and in quality, as a thesis for the degree of Master of Science.

_____

Ferdi Karadaş (Advisor)

_____

Burak Ülgüt

_____

Emren Nalbant

Approved for the Graduate School of Engineering and Science

_____

Orhan Arıkan

Director of the Graduate School

ABSTRACT

Electrocatalytic Water Splitting with Prussian Blue Analogues Under External Stimuli

Waqar Ahmad

M.S. in Chemistry

Advisor: Ferdi Karadaş

September 2023

The development of long-lasting and efficient catalysts for water splitting is crucial for the advancement of a carbon emission-free world. A well-known class of compounds called Prussian blue analogues (PBAs) offers several advantages such as high stability, diversity, and simple synthesis for the development of sustainable water-splitting devices. This thesis investigates the construction of PBA-based overall water-splitting electrolytic cells assisted with external stimuli.

Alsac et al. investigated the oxygen evolution reaction (OER) efficiency of various PBAs and concluded that Co-Co exhibits the best performance as an OER catalyst among the Co-M PBAs. Ahmad et al. studied the hydrogen evolution reaction (HER) performance of various PBAs and observed that Co-Ni stands out in performance. Furthermore, Chalil Oglou et al. elucidated the effect of the magnetic field on the OER catalytic activity of Co-Fe PBA electrodeposited on the surface of the FTO. His findings unveiled an enhanced catalytic activity under the influence of a magnetic field. To further explore these concepts, we aim to move one step ahead and combine all these studies to investigate overall water splitting (OWS) under the influence of magnetic field and solar light irradiation.

In this thesis, [Co-Co] was used for the OER reaction, while [Co-Ni] was utilized for the HER reaction. Both electrodes were prepared involving a two-step electrodeposition method and comprehensively characterized with SEM, EDAX, P-XRD, XPS, and ATR-FTIR. SEM images unveiled threat-like and needle-like grown particles with uniform sizes of 1-2 μm for [Co-Co] and [Co-Ni] formed on the fluorine-doped tin oxide (FTO) electrode respectively. The oxidation states of the pristine and post-catalytic electrodes and the stability during the electrocatalytic process were confirmed with XPS and FTIR studies.

The electrochemical characterization of these catalysts was thoroughly investigated with linear sweep voltammetry (LSV), chronoamperometry (CA), and cyclic voltammetry (CV) profiles.

The electrochemical performance was investigated in three chapters; OER, HER, and overall water splitting under magnetic and solar light irradiation.

(i) OER performance of FTO/[Co-Co] was evaluated with LSV, which shows prominent enhancement peaks under the influence of external stimuli. Under the influence of the magnetic field, it illustrated an enhancement of 11.9% with an overpotential of 949 mV, while in the presence of solar light, it showed an augmentation of 10.7% with an overpotential of 949 mV. CA profiles, recorded under magnetic field showed that there is a direct relation between magnetic field strength and the enhancement in the current density. On the contrary, an opposite trend is observed with the CA profiles under solar light irradiation, which suggests that the origin of the enhancement under the magnetic field is different from the one under solar light irradiation.

(ii) Similar to OER studies, HER activity of FTO/[Co-Ni] was investigated under the effect of solar light irradiation and magnetic field. The LSV profile showed enhancement only in the case of solar light, while no significant enhancement was observed under the magnetic field, contrary to the previous studies. Similar to OER, the CA profiles of FTO/[Co-Ni] illustrated the opposite trend with respect to overpotential applied. In the case of HER, CA under a magnetic field showed a small enhancement (1.4%) with an overpotential of 300 mV, which was attributed to the magnetohydrodynamic effect.

(iii) Two and three-electrode systems were used to conduct the investigation into overall water splitting. To achieve a current density of 1 mA/cm^2 in the two-electrode having FTO/[Co-Co] on the working/working sense electrode (W/WS) and FTO/[Co-Ni] on the counter/reference electrode R/C configuration, the system required an overpotential of roughly 1013 mV. The subsequent analysis of each electrode's unique voltage contributions helped explain this observation. OER takes around 1.3 V while it is 0.6 V for the HER side.

On the other hand, in the three-electrode configuration, the working electrode was FTO/[Co-Co], the counter electrode was FTO/[Co-Ni], and the reference electrode was Ag/AgCl. The observed profile notably showed significant improvement seen when solar light and magnetic fields were present.

Overall, this study indicates that there is still plenty of room for enhancement in catalysis, with slight modification in reaction conditions from another perspective i.e., external stimulus. This thesis takes a progressive step by raising the bar and adding a new dimension to the challenge of using PBAs in catalytic applications, building on earlier efforts.

Keywords: Prussian Blue Analogues, Oxygen Evolution Reaction, Hydrogen Evolution Reaction, Coordination Chemistry, External Stimuli, Spin Crossover, Magnetohydrodynamic, Overall Water Splitting, Photocatalysis,

ÖZET

Prusya Mavisi Analoglarıyla Dış Uyarıcıların Desteğinde Eletrokatalitik Suyun Parçalanması

Waqar Ahmad

Kimya Bölümü, Yüksek Lisans

Tez Danışmanı: Ferdi Karadaş

Eylül 2023

Suyun parçalanması için uzun ömürlü ve verimli katalizörlerin geliştirilmesi, karbon emisyonlarından arınmış bir dünyanın ilerlemesi için kritik bir öneme sahiptir. Prusya mavisi analogları olarak bilinen bir bileşik sınıfı (PBAs), yüksek kararlılık, çeşitlilik ve sürdürülebilir su bölünme cihazlarının geliştirilmesi için basit sentez gibi birçok avantaja sahiptir. Bu tez, dış uyarıcılar ile desteklenen PBA tabanlı genel su bölünme elektrolitik hücrelerinin inşasını araştırmaktadır.

Alsac ve iş arkadaşları, çeşitli PBAs'ın oksijen evrim reaksiyonu (OER) verimliliğini inceledi ve Co-Co'nun Co-M PBAs içinde en iyi performansı sergilediğini göstediler. Ahmad ve iş arkadaşları, çeşitli PBAs'ın hidrojen evrim reaksiyonu (HER) performansını incelemiş ve Co-Ni'nin performansta öne çıktığını gözlemlemişdiler. Ayrıca, Chalil Oglou ve iş arkadaşları, FTO yüzeyine elektrodepozite edilen Co-Fe PBA'nın OER katalitik aktivitesi üzerinde manyetik alanın etkisini açıklamaya çalıştılar. Bulguları, manyetik alan etkisi altında artan bir katalitik aktiviteyi öne sürmüştür. Bu fenomeni daha iyi anlayabilmek için, bu çalışmada manyetik alan ve güneş ışığı ışınımının etkisi altında tam su bölünme (OWS) olayını araştırmayı amaçlıyoruz.

Bu tezde, [Co-Co] OER reaksiyonu için kullanılmıştır, [Co-Ni] ise HER reaksiyonu için kullanılmıştır. Her iki elektrot da iki aşamalı bir elektro-depo yöntemi kullanılarak hazırlanmış ve SEM, EDAX, P-XRD, XPS ve ATR-FTIR ile kapsamlı olarak karakterize edilmiştir. SEM görüntüleri, [Co-Co] ve [Co-Ni] için sırasıyla florlu kalay oksit (FTO) elektrot üzerinde oluşan tehdit benzeri ve iğne benzeri büyüyen partiküllerin homojen boyutlarını ortaya koymaktadır. Pratik ve post-katalitik elektrotların oksidasyon durumları ve elektro-katalitik süreç sırasındaki kararlılıkları XPS ve FTIR çalışmaları ile doğrulanmıştır.

Bu katalizörlerin elektrokimyasal karakterizasyonu lineer tarama voltametrisi (LSV), kronoamperometri (CA) ve dönüşümlü voltametri (CV) profilleri ile ayrıntılı olarak incelenmiştir. Elektrokimyasal performans, OER, HER ve manyetik veya güneş ışığı ışınımı altında tam su bölünmesi olarak üç bölümde incelenmiştir.

(i) FTO/[Co-Co] OER performansı LSV ile değerlendirilmiştir ve dış uyarıcıların etkisi altında belirgin artış pikleri gösterilmiştir. Manyetik alan etkisi altında, aşırı gerilim 949 mV ile % 11.9'luk bir artış gösterirken, güneş ışığı varlığında, aşırı gerilim 949 mV ile% 10.7'lik bir artış göstermiştir. Manyetik alan altında kaydedilen CA profilleri, manyetik alanın şiddeti ile akım yoğunluğu artışı arasında doğrudan bir ilişki olduğunu göstermiştir. Tersine, güneş ışığı ışınımı altında kaydedilen CA profillerinde ters bir eğilim gözlemlenmiştir, bu da manyetik alan altında görülen artışın güneş ışığı ışınımı altındakinden farklı olduğunu önermektedir.

(ii) OER çalışmalarına benzer şekilde, FTO/[Co-Ni]'nin HER aktivitesi güneş ışığı ışınımı ve manyetik alanın etkisi altında araştırılmıştır. LSV profili, yalnızca güneş ışığının etkisi altında artış göstermiş olup manyetik alan altında ise önemli bir artış göstermemiştir. Önceki çalışmaların aksine HER için CA profilleri, manyetik alan altında küçük bir artış (1.4%) göstermiştir ve aşırı gerilim 300 mV'a ayarlanmıştır.

(iii) İki ve üç elektrotlu sistemler, tam su bölünme çalışmalarını yürütmek için kullanılmıştır. Bu çalışmada, iki elektrotlu sistem kullanılmıştır. İş-çalışma duyusu elektrodunda FTO/[Co-Co] ve karşı/referans elektrodunda FTO/[Co-Ni] kullanmak ve 1 mA/cm^2'lik bir akım yoğunluğu elde etmek için sisteme yaklaşık olarak 1013 mV'luk bir aşırı gerilim uygulanmıştır. Her elektrodun benzersiz voltaj katkılarının analizi, bu gözlemi açıklamaya yardımcı olmuştur. OER için yaklaşık 1.3 V gözlemlenirken, HER tarafı için bu değer 0.6 V'tur.

Öte yandan, üç elektrotlu yapıda çalışma elektrodu FTO/[Co-Co], karşı elektrot FTO/[Co-Ni] ve referans elektrodu Ag/AgCl'dir. Gözlemlenen profil, güneş ışığı ve manyetik alanın varlığında önemli bir iyileşme gösterdi.

Genel olarak, bu çalışma, katalizde hala iyileştirme için geniş bir alan bulunduğunu ve dış etkenler gibi reaksiyon koşullarındaki hafif değişikliklerin katalizdeki göstermektedir. Bu tez, katalitik uygulamalarda Prusya mavisi analoglarının kullanımı konusundaki mevcut çabaları temel alarak, çıtayı yükselterek ve zengin bir boyut ekleyerek bu zorluğa yeni bir boyut kazandırmaktadır.

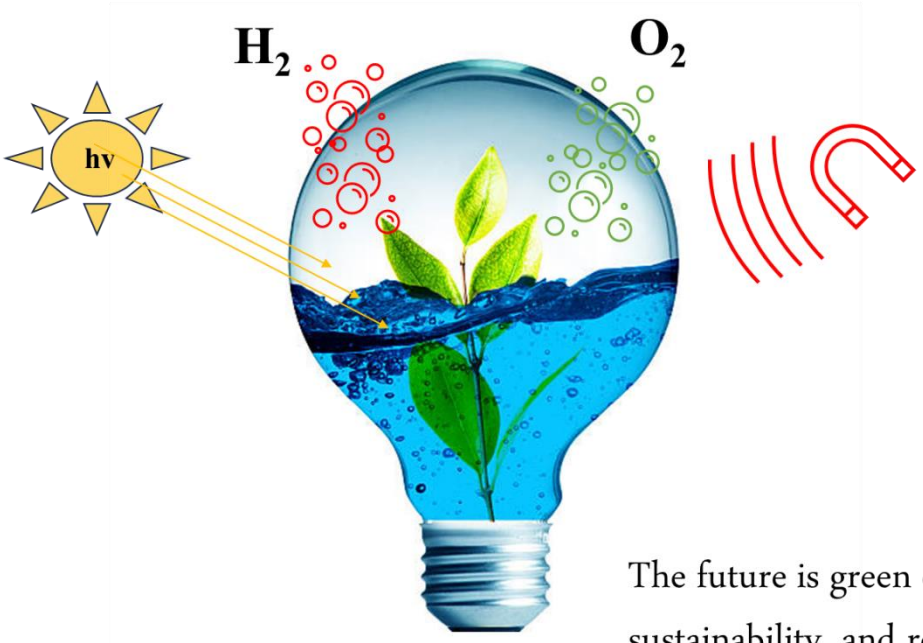

The future is green energy,
sustainability, and renewable energy.

Arnold Schwarzenegger

Acknowledgment

I would like to dedicate my whole work to Seher, without whose support it was almost impossible for me to complete the project. She has a very responsible and important role in my master's degree. I extend my heartfelt thanks to her, for unwavering support, patience, and understanding. Her constant belief in my abilities and continuous encouragement has been a constant source of strength.

Besides that, I would like to express my heartfelt gratitude to the foundational pillars of my life, my parents, with a special mention of my father, for their unconditional love, support, and encouragement throughout my academic journey. Your belief in me has been an invaluable source of motivation.

I am deeply indebted to my esteemed supervisor, Dr. Ferdi Karadas, for his invaluable guidance, expert insights, patience, and relentless dedication to nurturing my intellectual growth. Your mentorship has played a pivotal role in shaping the direction of this thesis and my academic pursuits. Besides that, I would like to show my humble gratitude towards Dr Halil Okur, and Dr Burak Ulgut. Indeed, their help and support were very much crucial in achieving this.

I extend my appreciation to the members of my Karadas research group with special thanks to Dr. Ruby, Ramadan, Sina, and Dr. Sara. Emir, Huseyin, and Yaren were helpful. The collaborative spirit has enriched my research experience. Your constructive feedback and shared insights have been instrumental in refining my work.

Lastly, to all my Pakistani, Bangladeshi, Turkish, and Arab friends, your companionship, and encouragement have provided solace during the demanding phases of this endeavor. Your presence has illuminated both my academic and personal journey. Special thanks to Hamid, Faruk, Muzaffar, Ahmad, Hilal, Wissam, Fahaar, Yunus, Yusuf and Ilyas.

This achievement is a result of the collective efforts, guidance, and support of all those mentioned and many others who have played a role in my academic voyage. Your contributions have enriched my life and academic pursuits immeasurably.

Contents

Table of Figures

LIST OF TABLES

Chapter 1: Introduction

1.1. Current Trends in Energy Technologies and Catalysis

The demand for energy is a critical factor in development and prosperity. Our conventional reliance on hydrocarbons as principal energy reservoirs has been beset by limitations particularly because of their finite nature and emission of polluting, gases, which deteriorate the decorum of our environment [1]. Energy is necessary for industrial activities, vehicle propulsion, residential institutions, medical facilities, and a variety of other vital life cycles, among many other life cycles [2]. Future energy resources should be renewable and sustainable, and should not generate methane, CO_2 [3, 4], etc. such as solar, hydroelectric, or wind energy. Thus, finding and establishing alternative energy sources is crucial to meet future energy demands with renewable and sustainable resources [4].

To address the aforementioned issues, catalysis is crucial in tackling the soaring energy needs of contemporary society [5]. The development of efficient catalysis using transition metals and photosensitizers is an attractive solution to address the world's energy demands sustainably [6]. This approach has shown promising results in converting solar energy into chemical energy, which can be stored and utilized in the future [7, 8]. Additionally, this technology can potentially replace conventional energy sources and reduce carbon emissions, mitigating the adverse effects of climate change [9]. Therefore, further research and development in this field are crucial to achieving a sustainable energy future.

Catalysis, which is a fundamental process in chemical transformations, provides detailed control over the reaction paths, and energy demands, resulting in accelerated and manipulatable controls over chemical reactions [10]. There are many parameters to manipulate while dealing with catalysis, and any small variation in the catalysis process has a great impact on its performance [11]. In turn, this makes it easier to produce the materials and energy carriers required for a variety of applications [12]. Catalytic processes enable energy-efficient technology by producing chemicals and fuels from renewable sources and purifying hydrocarbons [4]. In addition to its contributions to energy production, catalysis has numerous uses in a variety of scientific fields. Catalytic converters reduce harmful pollutants from vehicle exhaust [13] in the field of environmental science [14, 15], while catalysis allows the production of complex medicinal compounds in the field of pharmaceuticals [16]. Similarly, they play a role in the degradation of harmful organic dye pollutants and microbes to clean water [17]. A great deal of work is going on in regard to enhancing the performance of catalysis.

Solar energy is an abundant and renewable unlimited energy source that holds great potential for addressing the world's energy demands [18]. It uses photovoltaic and solar thermal technologies to capture sunlight and transform it into electricity and heat without creating any emissions. There is great work going on, in catalysis in regard to utilizing semiconducting properties with the help of solar light irradiation [19].

Moreover, catalysis has been studied for illustrating enhancement under the influence of magnetic fields. This section is discussed in detail in topic 1.3. Magnetic field-assisted Catalysis.

1.2. Water Splitting under Electricity and Light

Hydrogen is proposed as a future energy carrier due to its abundant nature, whose biggest precursor can be water, which covers 75% of our planet Earth [20]. Hydrogen as an energy carrier is also supported by the fact that this source is renewable [21]. Moreover, hydrogen is not only used as a fuel to produce heat but also can be used to generate electricity when treated with oxygen in optimized conditions producing water as a byproduct [22]. In addition to that, hydrogen also has low viscosity, which makes it easy to be transported through storage or pipeline systems [23, 24].

There are many ways to generate hydrogen e.g., steam methane reforming [25], and coal gasification [26] in which methane gas or carbon respectively is treated with water to produce carbon dioxide and hydrogen gas, but the drawback of this method is that it is carried out at a very high temperature, i.e., 1000 ^{o}C and that it gives carbon dioxide, which is harmful to our environment [27]. Although water splitting could be a benign approach toward green energy. It is a highly energy-demanding process, which should be overcome with an external stimulus thermochemical water splitting can require up to 2000 °C [28, 29].

Water-splitting has the potential to provide a sustainable path to produce hydrogen [30], which can simply be described as electrochemical [31] photocatalytic or photoelectrochemical conversion [32] of water into hydrogen and oxygen gases [33]. These reactions are made easier by catalytic materials since they can dramatically lower the activation energy barriers, speed up the reactions, and regulate the reaction paths. Catalytic materials play a key role in the corresponding anodic and cathodic half-reactions of the oxygen evolution reaction (OER) and hydrogen evolution reaction (HER). The development of effective catalysts for these processes,

such as transition metal oxides [34], metal chalcogenides, Prussian blue analogues, and molecular complexes [35], has advanced significantly in recent years [36].

Electrochemical water splitting has been regarded as one of the most convenient and efficient ways to get hydrogen with high purity and minimum pollution. This approach has shown promising results in converting solar energy into chemical energy, which can be stored and utilized in the future. The general demand for water splitting is 1.23 V or above with reference to Ag/AgCl electrodes as reference. Given the difficulty of this $4e^-$ process, the development of an efficient catalyst is critical to address the water-splitting process.

Platinum takes the crown for being the state of art catalyst for cathode/hydrogen production, while IrO_2/RuO_2 performs the best anodic reaction under basic conditions. However, the problem with catalysts such as Pt, IrO_2 Pt, IrO_2, and RuO_2 is that they are scarce and expensive.

Electrochemical water splitting consists of two half-reactions, called hydrogen evolution reaction HER and oxygen evolution reaction OER. Based on the medium of the reaction, the water-splitting reaction mechanism is different in an acidic medium than neutral or basic medium. In an acidic medium the reaction advents from the anode where the water molecule loses electrons and splits into two protons and an oxygen molecule, which is liberated.

1.2.1. Water Splitting in an Acidic Medium

I. Oxygen Evolution Reaction (OER)

Water molecules adhere to active sites on the catalyst (*), leading to their transformation into hydroxide ions (OH^-) and the release of an electron (e^-). These hydroxide ions (OH^-) then convert into oxygen ions (O), simultaneously emitting an electron (e^-). The oxygen ions (O*) interact with water molecules, producing oxygen gas (O_2) and releasing an electron (e^-).

1. $H_2O + {}^*(\text{Active site}) \longrightarrow OH^* + H^+ + e^-$ (1)
2. $OH^* \longrightarrow O^* + H^+ + e^-$ (2)
3. $O^* + H_2O \longrightarrow OOH^* + H^+ + e^-$ (3)
4. $OOH^* \longrightarrow O_2 + {}^*(\text{Active site}) + H^+ + e^-$ (4)

II. Hydrogen Evolution Reaction (HER)

In this procedure, electrons are removed from the liquid to attach hydrogen atoms (also known as adsorbed hydrogen atoms, or H_{ads}) that interact with the catalyst's active sites. These adsorbed hydrogen atoms react with incoming protons and electrons to form hydrogen gas

when only a small number of them are present. On the other hand, if there are too many hydrogen atoms adsorbed, they can combine to form hydrogen gas through a collective process.

The HER reaction may proceed in two different ways,

- **Volmer Step**

The proton goes to the cathode, receives an electron, and gets itself adsorbed.

$$H^+ + e \longrightarrow H_{ads} \quad (5)$$

- **Heyrovsky step**

Another proton comes and in the presence of an electron binds with the adsorbed hydrogen to form a hydrogen molecule.

$$H_{ads} + H^+ + e^- \longrightarrow H_2 \quad (6)$$

1.2.2. Water Splitting in Basic/Neutral Medium

I. Oxygen Evolution Reaction in Basic/Neutral Medium

In basic or neutral media, the OER goes through the following steps series of phases. OH, interacts with surface sites (*), releasing electrons (e^-). Then, through an electron transfer reaction, OH* combines with more OH to form surface-bound oxygen species (O*) and water (H_2O). The surface-bound per oxo species (OOH*) produced by this (O*) species' interaction with OH releases an electron (e^-). In the long run, OOH* reacts with OH to produce molecular oxygen (O_2), regenerate active surface sites (*), and release water (H_2O), while electron transport takes place. The OER reaction in basic media.

1. $OH + {}^* \longrightarrow OH^* + e^-$ (7)
2. $OH^* + OH \longrightarrow O^* + H_2O + e^-$ (8)
3. $O^* + OH \longrightarrow OOH^* + e^-$ (9)
4. $OOH^* + OH \longrightarrow O_2 + {}^*(\text{active sites}) + H_2O + e^-$ (10)

II. Hydrogen Evolution Reaction in Basic/Neutral Medium

Water molecules (H_2O) and electrons (e^-) combine to produce hydrogen gas (H_2) and hydroxide ions (OH^-).In the context of the basic medium, the reaction's modality varies as follows.

- **Volmer step**

$$H_2O + e^- \longrightarrow H_{ads} + OH^- \quad (11)$$

- **Heyrovsky step**

$$H_{ads} + H_2O + e^- \longrightarrow H_2 + OH^- \quad (12)$$

In case H_{ads} is highly concentrated, the H_{ads} react with another H_{ads}.

$$H_{ads} + H_{ads} \longrightarrow H_2 \quad (13)$$

Subsequently, the protons leave for the cathode, where they receive 2 electrons and are adsorbed on the anode surface and quickly convert into hydrogen molecules, which liberate from the anode. On the contrary, in a basic medium, the reaction begins with receiving 2 electrons from the cathode, forming hydrogen molecules and 2 OH^- ions [37].

In a heterogeneous catalytic system, the fermi level of the system can be raised high by applying the potential difference, which makes it easier to induce electron transfer into the conduction band of the catalyst [38].

In water splitting, comparatively, the OER part requires more overpotential due to the following three reasons [39].

i. The spin state of the O_2 molecule is a triplet as shown in Fig 1.1, however, the spin state of OH^- and H_2O both are singlet, which makes the kinetics of this reaction slower [40].

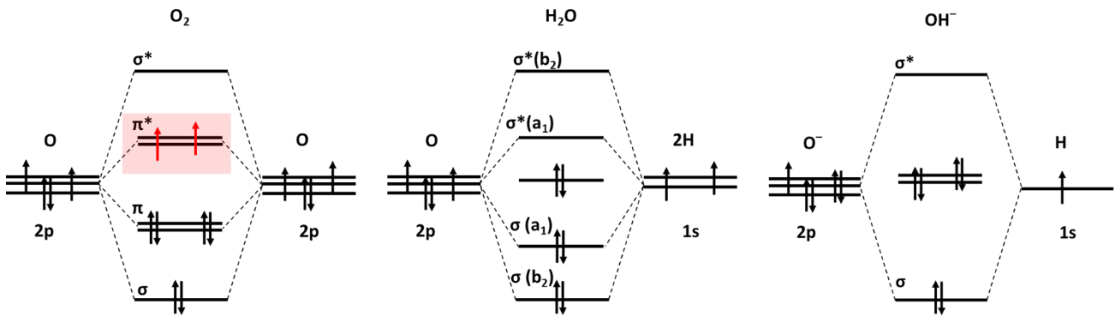

Fig 1.1 Spin state of O_2 is different from H_2O and OH^-.

ii. The electrons taken by the adsorbate during the OER reaction must flow through areas like electrocatalysts and external circuits [41].

iii. Electrical conductivity of the catalyst plays a vital role in the increased demand of overpotential for OER [42].

OER reactions in water splitting have been investigated with numerous numbers of inorganic catalysts, including simple structures like metal oxides [43], selenides [44], and some complicated structures like MOF [45], perovskites structures [46], and recently structures with surfactants [47] and liposomes [48] are introduced recently with enhanced electrochemical activity performance.

1.3. Prussian Blue Analogues

Prussian blue analogues (PBAs) are cyanide-based polymeric compounds that connect two metals through a cyanide bridge. The story of cyanide-based compounds back to 1704 when the first coordination compound was discovered by German Artist Diesbach [49]. The major precursor of cyanide-based coordination polymers, potassium ferrocyanide, or $K_4[Fe(CN)_6]$, is laboriously isolated by mixing animal waste with sodium carbonate in a pot of iron to produce Prussian blue [50].

Computational studies investigated the electronic distribution, their binding characteristics, and the resulting metal-ligand interactions in cyanide ligands. Because carbon-based HOMO and LUMO orbitals predominate, the monodentate binding nature of cyanide to metal centers is usually established through carbon [51]. As indicated by examples like iron in $[Fe(CN)_6]_4$ and cobalt in $(PPN)_2[Co(CN)]_4$, cyanide is categorized as a high-field ligand [52]. Due to HOMO and LUMO interactions, this interaction produces relatively weak π bonds, when they receive electrons from metal as shown in Fig 1.2, while also producing strong σ bonds with electron transfer from the ligand to the metal.

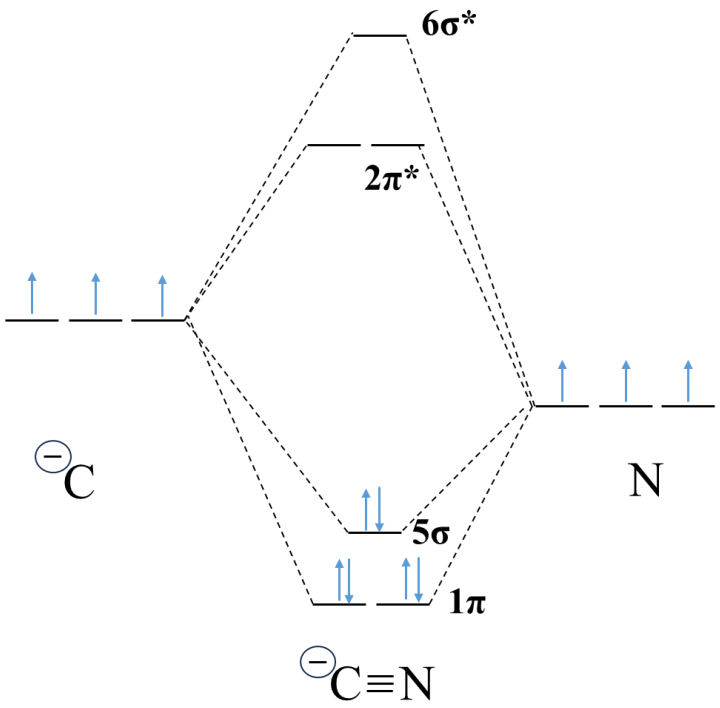

Fig 1. 2 Illustration of cyanide ion HOMO LUMO molecular orbital diagram.

Through FT-IR and X-ray diffraction spectroscopic techniques, the π back bonding can be well understood. Cyanide coordination with metal ions displays a shorter M-CN bond with more π back donation as illustrated in Fig 1.3 [53].

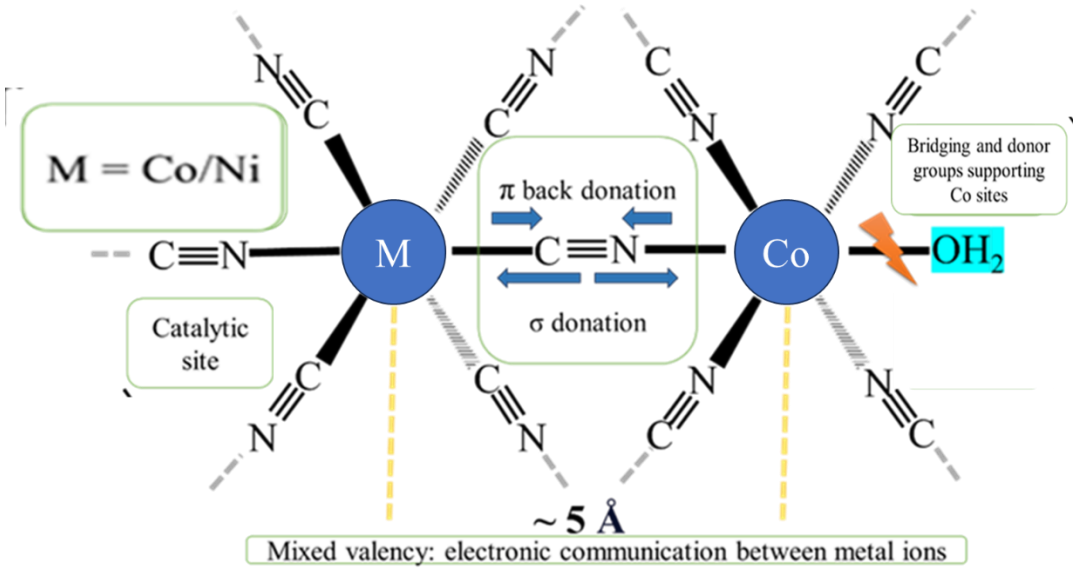

Fig 1. 3 Chemical structure of PBA FTO/[Co-M], (M = Co/Ni) illustrating the effect of σ donation and π back donation on bond length in [Co-M], (M =Co/Ni).

The cyanide bond is further weakened by coordination through nitrogen atoms because nitrogen's lone pair is antibonding. In infrared spectra, as illustrated by Fig 1.4 ν(CN) stretches that reflect electronic characteristics and are unable to pull off the electron pair due to electronegativity, coordination number, and metal oxidation state are reflected [54]. PBAs exhibit a variety of structural variations with promise for use in electrochromics [55], biosensing [56], energy conversion, and storage [57], among other fields. The active cobalt sites and switchable characteristics of cobalt hexacyanometallates make them adaptable candidates for photomagnetism- and catalysis.

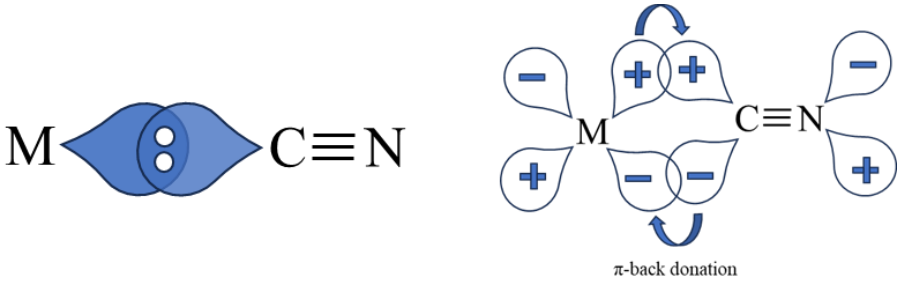

Fig 1. 4 Schematic diagram illustrating σ donation and π back donation.

PBAs offer a wide surface area, tunable metal active sites, and a vast variety of framework structures that make them very attractive for water-splitting technologies. [[58, 59, 49].

The electronic configuration of the cyanide ion $(1\sigma)^2$ $(2\sigma)^2$ $(3\sigma)^2$ $(4\sigma)^2$ $(1\pi)^4$ $(5\sigma)^2$, making it isoelectronic with molecular species like N2, CO, and NO+. This isoelectronic resemblance is explained by the occurrence of a triple bond formation with a bond distance of 1.16 Å between the carbon and nitrogen atoms in the structure [49, 60].

1.4. OER Mechanism on the Cobalt Site

The advancement of the OER encounters limitations due to the problems like linear scaling relationships [61] and high overpotential demand as discussed above inherent in its reaction intermediates. Several complicated factors play a role in the behavior of cobalt sites during water-splitting events. For coordination compounds, the cyanide group's vibration can serve as a distinctive marker. We can determine the cyanide group's connection, assess the oxidation states of metal ions, and comprehend their electron densities by examining changes in this vibration. The cyanide vibration moves to higher frequencies as the metal's oxidation state rises, showing electron shortages in Co^{II} centers [53]. Fig 1.5 shows how we can arrange the electron densities at Co^{II} sites in particular structures using this information. In turn, the

electron densities shed light on the rate-determining step (r.d.s.) in the catalysis of water oxidation. The oxidation stage and the water's nucleophilic attack have been identified as two competing steps. The [Co^{II}-Co^{III}] analog stands out as an effective catalyst among the many structures examined because of its reduced electron density. This correlation shows that the rate-determining step is the water's nucleophilic attack on the intermediate [58]. It is significant to notice that the difference in electron densities persists even when the electrical characteristics of the catalyst change when a voltage is applied. The study's conclusions are important.

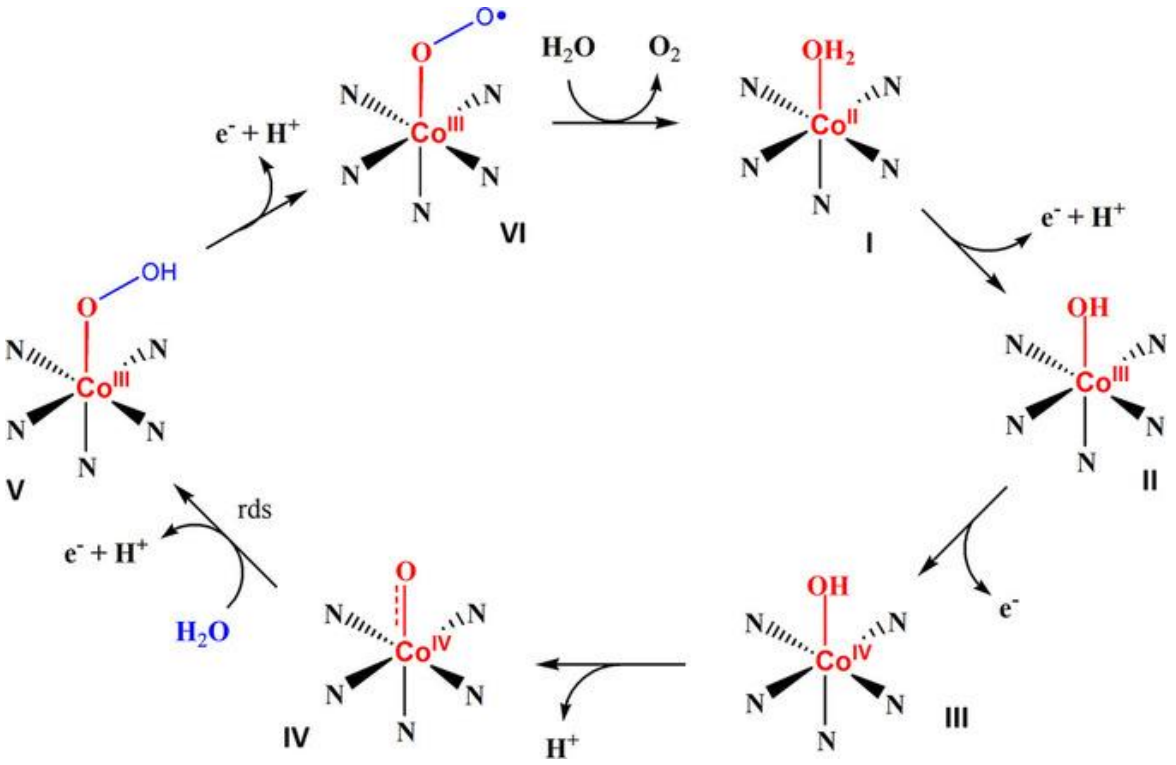

Fig 1. 5 Schematic diagram illustrating OER reaction on Co^{2+}. [Reprinted with permission from ref [58] (Alsaç et. al., Chem. Eur. J, 2018, 24(19), 4856-4863) WILEY-VCH verlag GmbH & Co. KGaA, Weinheim].

An important factor that has a significant impact on the electrocatalytic process of water oxidation is the electron density of Co^{II}. It is now clear that there is a direct correlation between the structural configuration and the electrical characteristics when the type of hexacyanometallates group is changed. The complicated interaction between oxidation state and electron density is strengthened as the metal's oxidation state is increased since this causes a decrease in electron density at Co^{II} sites. The nucleophilic attack of water on the cobalt-oxo intermediate is likely the rate-regulating step in water oxidation catalysis, highlighting the significance of this interaction pathway [58].

There are four crucial steps for the OER process as shown in (Equations 17-20). These steps are accompanied by transferring of protons and electrons between the molecules to produce oxygen ultimately. Here the most challenging step is equation 2, where a molecule with a negatively charged oxygen atom and a positively charged hydrogen atom (referred to as *Co–OH) transforms into a molecule with a negatively charged oxygen atom and a neutral hydrogen atom (referred to as *Co–O). This step is energetically demanding and requires a relatively high voltage to proceed.

Fig 1.6 shows the spin crossover effect is found to assist the OER reaction in step 2. The term "spin" describes the intrinsic angular momentum, or "spinning" motion, of electrons. Spin crossover is a phenomenon in which the spin states of the electrons alter because of outside influences such as temperature, pressure, or an applied magnetic field. Some chemicals involved in the OER may behave differently as a result of the SCO effect [62].

The SCO effect is proposed to occur between two spin states of a molecule called *Co–OH. In its initial state, this molecule has a certain spin configuration called the low-spin (LS) state. Through the SCO effect, it can transition to another spin configuration called the intermediate-spin (IS) state. This transition happens because of changes in the molecule's electronic environment caused by factors like an external electric field.

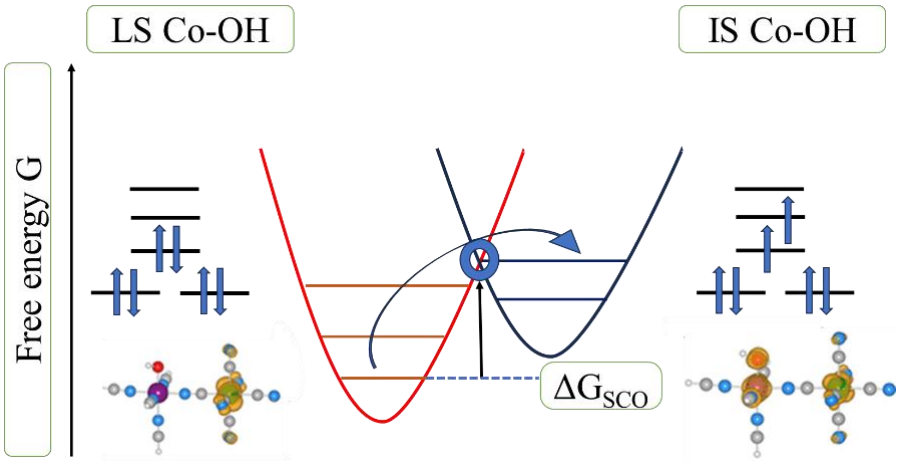

Fig 1. 6 Schematic diagram illustrating spin crossover effect from low-spin to intermediate-spin.

The IS state of the *Co–OH molecule is found to be more favorable for the OER process. In this state, the molecule is more efficient at transferring electrons during the OER, which makes the overall reaction require less energy.

This SCO-assisted pathway provides a new way to make the OER more efficient. By controlling the spin states of molecules involved in the reaction, scientists can reduce the energy needed for the OER to occur. This is a novel approach to improving electrocatalysis and enhancing the efficiency of processes like water splitting for clean energy production.

Equations 17-20 illustrate how the oxygen evolution reaction (OER) takes place in a series of steps, with a challenging step 2. It introduces the concept of spin crossover (SCO), where the spin states of certain molecules involved in the OER can change, leading to more efficient reactions. This SCO-assisted pathway offers a new strategy to enhance the efficiency of OER and other electrocatalytic processes.

$$*M-\square + H_2O \rightleftharpoons *M-OH + H^+ + e^- \quad (17)$$

$$*M-OH \rightleftharpoons *M-O + H^+ + e^- \quad (18)$$

$$*M-O + H_2O \rightleftharpoons *M-OOH + H^+ + e^- \quad (19)$$

$$*M-OOH \rightleftharpoons *M-\square + O_2\,H^+ + e^- \quad (20)$$

To address the overpotential and linear scaling relationship issues, stimuli like solar irradiation (favoring semi-conducting effect) and magnet (involving the manipulation of spin configurations) in water oxidation intermediates offer a means to surmount these constraints. Franziska et al. explained cobalt hexacyanoferrate (CoFe−PB), which not only demonstrates as a proficient and resilient water oxidation catalyst [58] but also presents magnetic switching capabilities. Capitalizing on its versatile electronic structure, CoFe−PB emerges as a promising contender for magnetic modulation of the OER.

This study employs first-principles density functional theory calculations to expound on the OER dynamics within two distinct CoFe−PB model systems and assesses the potential for spin-crossover (SCO) phenomena as shown in Fig 1.7 in their stable states. The findings unveiled a remarkable prospect: the incorporation of SCO during OER can appreciably decrease the overpotential by 0.7 V, resulting in an overpotential hovering around 0.3 V, which is in good agreement with experimental measurements. Moreover, under the influence of an external potential surpassing 1.5 V vs SHE, the SCO-assisted pathway garners substantial favor [63].

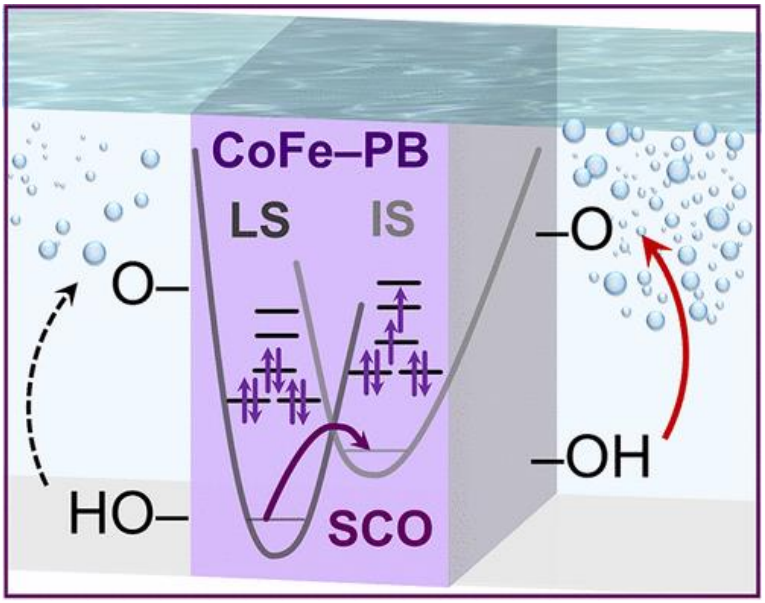

Fig 1. 7 Schematic diagram illustrating the assistance of spin-crossover in water splitting. [Reprinted with permission from ref [63] (Hegner. F. et. al., J. Phys. Chem. Lett. 2022, 13, 18, 4104-41102). Copyright (2022) American Chemical Society].

1.5. HER Mechanism on the Cobalt Site

Similar to OER reactions, the cobalt complexes can transform into different forms and interact with various external stimuli including acids and light to generate hydrogen in various ways.

Based on various forms of cobalt, the HER reaction may proceed in various ways as follows.

Fig 1.8 illustrates the formation of hydrogen through multiple sets of reactions, in which the cobalt acquires various oxidation states.

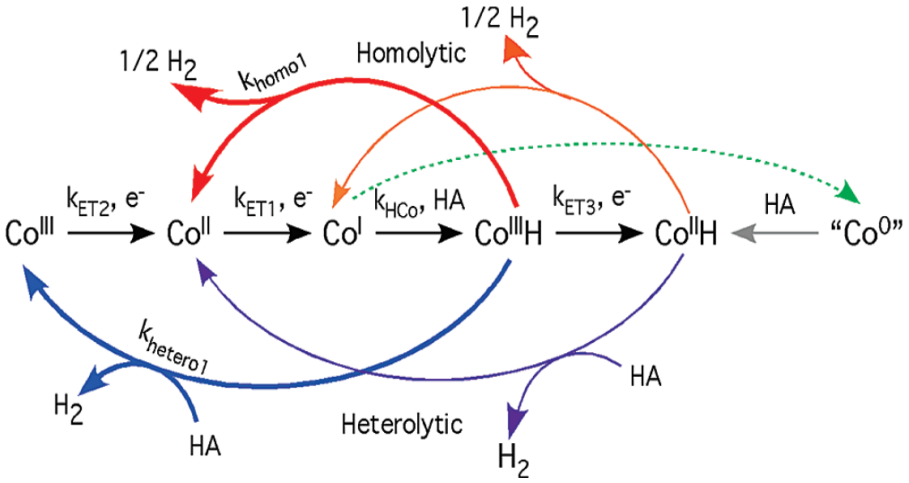

Fig 1. 8 Schematic diagram illustrating HER mechanism on cobalt complexes. [Reprinted with permission from ref [64] (L. Dempsey et. al., Acc. Chem. Res. 2009, 42, 12, 1995–2004). Copyright (2009) American Chemical Society].

- The cobalt complexes undergo reduction from Co^{3+}/ Co^{2+} to Co^{1+} which enable it to be protonated to become $Co^{3+}H$. After the formation of $Co^{3+}H$, the reaction may proceed through different pathways, a) Homolytic path: this hydride can be treated with another hydride ($Co^{3+}H$) to liberate H_2 indicated by the red path in Fig 1.9. b) Heterolytic path: Another way for the reaction to proceed is by getting extra hydrogen to form H_2 while $Co^{3+}H$ is converted into Co^{3+}.
- $Co^{3+}H$ can also be turned into $Co^{2+}H$ which again can be treated with $Co^{2+}H$ to get H_2 following a similar path as above.
- Another scenario is, that if Co^{1+} is not provided with hydrogen, it can be reduced directly to Co^{0} which in turn can get hydrogen to be converted into $Co^{2+}H$, which can undergo a similar path mentioned above.

According to this study, an acidic medium accelerates this reaction, as this reaction is continuously consuming hydrogen which makes an acidic environment favorable for such reactions. The reaction may be controlled with the amount and concentration of the acid, the reaction can be manipulated. The reaction path followed in the case of strong and weak acids is very different.

Apart from medium, another factor that can potentially change the reaction parameters is light energy.

Since, the cobalt complexes for HER reaction lack the step where (Co-OH) to (CoO^{-}), where the spin state is convertible from low spin to intermediate spin, the reaction cannot undergo spin crossover, and there will be no enhancement under the effect of the magnetic field [64].

1.6. Magnetic Field-Assisted Catalysis

The pursuit of improved catalyst materials has been coupled with the emergence of innovative strategies involving external fields such as gravity, light, ultrasound, and electric fields. These external stimuli have demonstrated the capability to enhance mass transfer at the electrode surface and alter reaction kinetics, opening new avenues in electrochemistry. Particularly intriguing is the recent exploration of coupling magnetic fields with electrochemistry [65], presenting a promising and novel approach to boost electrochemical reactions [66]. The effect of the magnetic field on catalysis has been known for decades, the effect of which has been under debate [67]. Magnetic fields can affect intricate electrocatalytic systems in a variety of

ways. For instance, forces like the Lorentz force and Kelvin force allow them to directly affect the electrolyte's electric currents and specific magnetic particles. Furthermore, the localized heating that can result from a rapidly changing magnetic field can actually aid electrochemical reactions. The behavior of electrochemical reactions can also be affected by other magnetic field effects, such as the Maxwell stress effect and the spin selectivity effect [68].

First studies indicate that the enhancement mainly roots due to the Lorentzian force [69], which describes the force experienced by a charged particle moving through an electromagnetic field, backed by the diffusion of reagents or gas bubbles liberation but necessarily it cannot always increase the efficiency, but also can negatively affect the catalytic activity [70, 71] This was immediately rejected when some technical explanations were put forward [72].

The magnetohydrodynamic (MHD) effect, magnetothermal effect, spin polarization effect, and magnetoresistance (MR) effect are able to improve the diffusion, surface temperature of the catalysts, reaction path, and spin electrons transport efficiency, respectively, in a variety of electrochemical reactions [73]. Later, much study has been pursued in order to find out the real nature of catalysis and magnetic field relation [74]. The theories behind this enhancement are briefly discussed herein.

1) ***Magnetohydrodynamic effect*:** In processes like OER or HER, electrogenerated bubbles present a significant problem because they affect energy and mass transfer in gas-evolving electrodes. The reaction at the electrode surface that causes the solution to become supersaturated and subsequently bubble formation and growth is linked to the development of gas bubbles. These bubbles may enclose active areas, interfere with the distribution of current, and result in undesirable outcomes like significant overpotentials [75]. Strategies for removing bubbles have been investigated as a means of reducing these effects [76]. These strategies can be divided into two types: those requiring an additional energy source to change behaviour and those that use external sources like magnetic fields. Investigations into the impact of magnetic fields on bubble dynamics have revealed increased electrocatalytic activity [77]. Applying an external magnetic field can help remove bubbles, reduce overpotentials, and improve electrocatalytic performance. This magnetic-field-induced bubble removal affects ohmic resistance and overall electrocatalysis, driven by forces like Lorentz and Kelvin forces, and even by current distortion within the catalysts themselves [77]. MHD effect mainly enhances mass transport on the catalytic interface needed during the catalytic process under the magnetic field [77]. Contrary to initial

expectations, empirical evidence suggests that the observed OER enhancement is not predominantly attributed to the Lorentzian force. This conclusion is substantiated through two primary lines of investigation. Firstly, the study examines non-ferromagnetic catalysts, specifically Co_3O_4 and IrO_2, where the Lorentzian movement is not pronounced due to weak magnetic interactions. Secondly, there was hardly any difference observed in the OER performance of $Co(acac)_2$ and $Fe(acac)_3$ with and without a magnetic field. However, species like OH^- and $H3O^+$ partake in transport through sequential proton transfer processes, known as the Grotthuss dynamics/magnetohydrodynamic effect [78].

2) ***Spin Polarization effect*:** In this study, spins with preferential orientation exhibit a more dominated direction in which both the possible states may not be equally populated. The effects of a magnetic field on the ferromagnetic and non-ferromagnetic materials $CoFe_2O_4$ (spin polarizer), Co_3O_4, and IrO_2 were investigated. In comparison to Co_3O_4 and IrO_2, which showed little magnetic susceptibility, $CoFe_2O_4$ among them showed improved performance when exposed to a magnetic field. Notably, the Tafel slope of $CoFe_2O_4$ significantly decreased, dropping from about 120 to 90 $mV.dec^{-1}$. This improvement was attributed to the catalyst's ability to act as a spin polarizer when a magnetic field is present. This ferromagnetic catalyst promotes the production of oxygen with parallel spins by aligning electron spins. The underlying cause of this phenomenon is "quantum spin-exchange interactions." These interactions lead to the oxygen evolution reaction (OER) experiencing facilitation, where the initial step of the reaction Fig 1.9, which was previously rate-determining under a magnetic field, is no longer the limiting factor [79, 80]. This important finding highlights the need of maintaining total spin on active sites during OER, a key idea that makes use of quantum spin-exchange interactions to enhance reaction kinetics [63, 81, 82, 83]. Galan-Mascaros et a. studied the growth of catalytic materials (magnetic or non-magnetic) on magnetic substrates such as Ni foam has shown promise in enhancing reactions like the Oxygen Evolution Reaction (OER) attributing the effect to spin polarization effect [84].

3) ***Spin Crossover effect*:** The process of switching between configurations distinguished by d^4 and d^7 electron counts within a metal complex from the first two rows of the periodic table is subject to modification by outside forces like magnetic fields, variations in temperature, or shifts in pressure. This phenomenon also involves the conversion of the spin state of the metal complexes, either high-spin (HS) or low-spin (LS). Co-Fe Prussian

blue analogues are prone to undergo spin crossover easily. Co-NC-Fe is a switchable molecular magnet that can function in a wide pH range and in step 2 of OER reactions as shown in (Eq. 18) [63]. Besides this, a similar study was pursued by Ramadan et al. who found a 10.7 % enhancement in OER reaction under magnetic field.

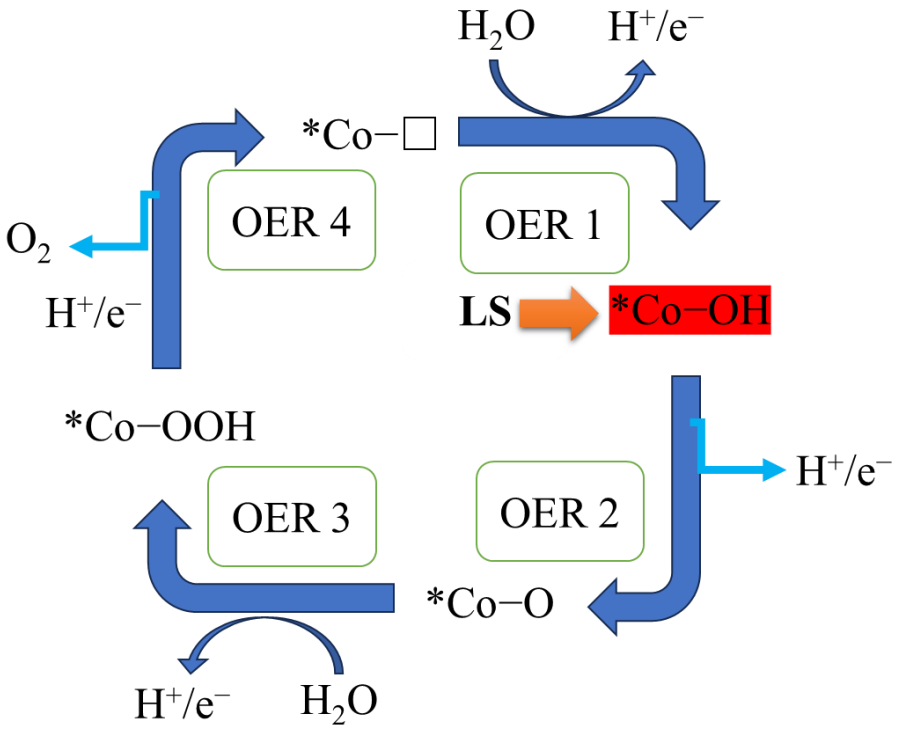

Fig 1. 9 Scheme illustrating the importance of spin crossover effect for Cobalt-based catalyst during a water splitting reaction.

The application of magnetic fields to catalytic processes has garnered significant attention due to their potential to enhance various reaction aspects. Table 1 provides a comprehensive summary of catalytic processes that can be augmented through magnetic field assistance, accompanied by the underlying rationales. In the context of the HER, the application of a magnetic field is anticipated to enhance HER activity. This enhancement is usually due to mechanical changes in the reaction particularly MHD, or Lorentz force, resulting in higher catalytic activity. Similarly, the OER (being spin dependent reaction) can benefit from magnetic field assistance, primarily due to its influence on oxygen adsorption and activation, and also influencing the reaction mechanism through spin pining/polarization or spin crossover effect, thereby facilitating quicker oxygen evolution kinetics. Furthermore, charge transfer processes are influenced by magnetic fields, which can lead to altered charge transfer rates and

mechanisms. This effect is attributed to the magnetic field's capability to influence charge distribution and modify electron transfer mechanisms in redox reactions.

Table 1. 1 Summary of Magnetic Field Assisted Water Splitting catalysis

S. No	First Author	Material	Catalytic Activity	Credit for enhancement	Enhancement	Year
1	Yuanyuan	NiFe-LDH/Co3O4/NF	OER	Synergy	Decrease of overpotential by 25 mV	2022
2	Steven R. Ragsdale,	Pt and Au microdisk electrodes	Electrochemical reduction of acetophenone (AP)	Magnetic field-induced convective fluid flow altering mass transfer	100% efficient	1996
3	Liang Cai	Fe–Co–Ni–P–B magnetic catalyst	HER	Lorentz interaction enhancing charge-transfer efficiency	27% increase in current density at 20 mT	2022
4	Jose Ramon	NiZnFe4Ox on Ni Foam	Alkaline water electrolysis	Spin Polarization	Current density 100% / intrinsic activity 40%	2019
5	Liju Elias	Electroactive Ni–W alloy coating with a specific composition	HER	MHD-induced convection and H_2 bubble disentanglement	Reduction in high overvoltage towards HER	2017
6	Lorena M A	Fe, Co, Zn electrodeposited on (PANI) coated gold electrodes	ORR	Zn MHD, Fe, Co Lorentz interaction	Zn = 3% Fe = 12% Co = 8%	2012

7	Yuanyuan Zhang	($Ni(OH)_2$, NiO, and Ni)	OER	MR + MHD + Charge transfer	Overpotential decrease by 20 mV to produce 10 mA/cm^2	2022
8	Xiao Ren	$CoFe_2O_4$, Co_3O_4, and IrO_2	OER	Spin Polarization during 1^{st} step of OER	Tafel decrease from 109 mV/dec to about 87.8 mV/dec	2021
9	Jiawei Chen	$NiFe_2O_4$@MOF-74	HER	Lorents + MHD	Overpotential decreased by 31 mV for 10 mA, 7.7% enhancement	2020

1.7. The Motivation of This Thesis Study

While various electrochemical reactions have exhibited positive responses to magnetic fields through mechanisms like the magnetohydrodynamic effect and spin polarization effect, challenges still persist. Common magnetic materials suffer from issues like agglomeration and limited active sites, impacting their catalytic activity. Many "magnetization effect" catalysts struggle to ensure both catalytic activity and magnetic field enhancement. Additionally, the precise mechanism underlying the enhancement of catalysts supported on magnetic substrates under magnetic fields remains unclear. As there could be three possible reasons for the enhancement under magnetic field, mentioned as MHD effect, spin polarization effect, and spin crossover effect as summarized in Fig 1.10.

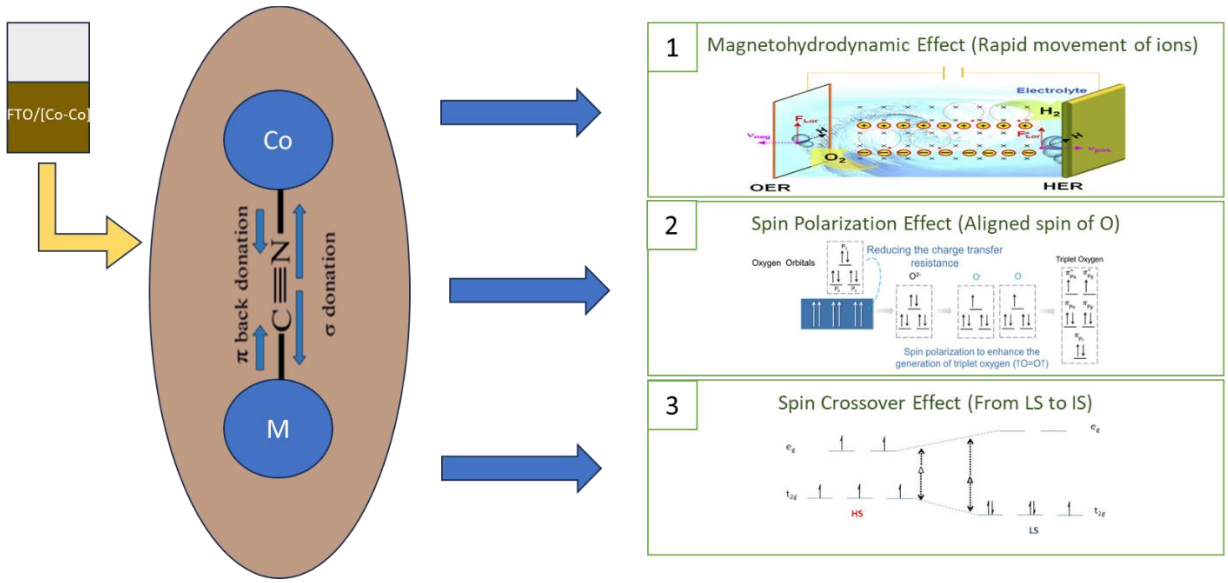

Fig 1. 10 Summary of the possible effect of magnetic field on the enhanced catalysis.

To address these challenges, our work takes a comprehensive approach, focusing on taking full advantage of the external stimulus but combing HER and OER making an over-all water splitting reaction under the influence of magnetic field using PBAs, which are one of the finest IMCT , and spin crossover effect illustrating catalyst [85]. This architecture leverages enhanced conductivity and increases catalytic performance resulting in promising OWS activity.

Co-Fe PBAs, have recently been shown to be active catalysts for numerous applications, i.e., CO_2 conversion, alcohol splitting, HER and OER, etc. Alsac et al. investigated a series of PBAs for the OER process as summarized in Fig 1.11 and found that FTO/[Co-Co] gave the highest productivity in OER generation. The study is minimized in the following graph, which compares the OER activity of various Prussian blue analogues [58]. From this graph, it is obvious that [Co-^{II}Co^{III}] is the best OER catalyst reaching over 3.7 mA/cm^2 of current density. According to the study,- [Co-^{II}-Co^{III}] reaching 1 mA current density with the lowest overpotential compared to other PBAs of 565 mV, has the highest TOF of 5.0 x 10^{-2}/s.

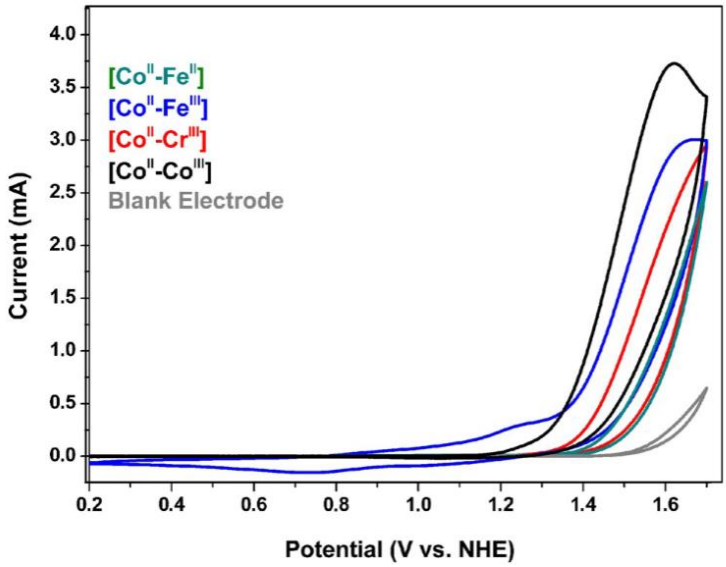

Fig 1. 11 Relative activity of PBAs comparing OER current density. [Reprinted with permission from ref [58] (Alsaç et- al., Chem. Eur. J, 2018, 24(19), 4856-4863) WILEY-VCH verlag GmbH & Co. KGaA, Weinheim].

Furthermore, Ahmad et al. investigated a series of PBAs for the photocatalytic HER process shown in Fig 1.12. In this study [Co-Ni] PBA, which has a two-dimensional network structure, exhibits a high HER activity in the presence of a ruthenium photosensitizer. In this study, photocatalytic hydrogen evolution was performed in a three-component system that included the catalyst, the photosensitizer $[Ru(bpy)_3]Cl_2$, and the sacrificial electron donor ascorbic acid. This was done in an aqueous medium with a pH of 5.0. A noteworthy aspect was the [Co-Ni] catalyst's extraordinary hydrogen evolution reaction (HER) efficacy, which was measured at 4229 µmol/gh. This performance is about 20 times better than that of [Co-Fe] (216 µmol/gh) and [Co-Co] (617 µmol/gh).

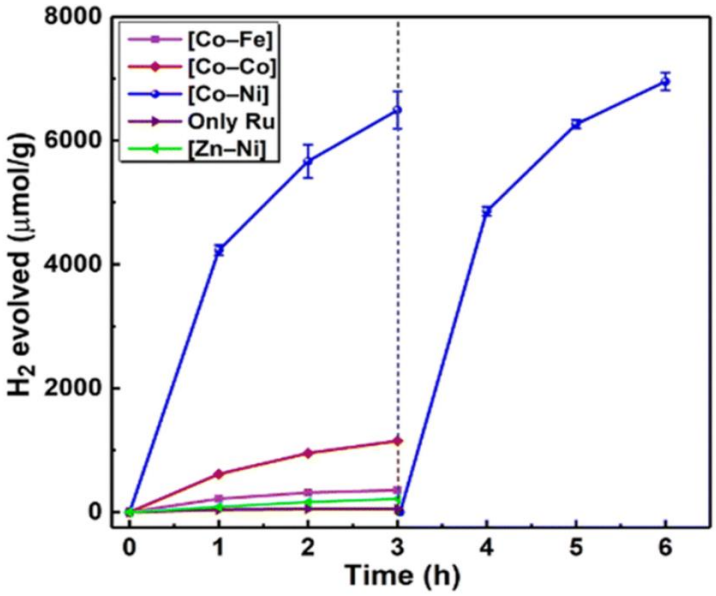

Fig 1. 12 Relative activity of PBAs comparing HER evolution. Reprinted with permission from ref [59] with permission of Royal Society of Chemistry, London.

Chalil Oglou et al. advanced one step ahead and investigated the catalytic properties of PBAs for the application of oxygen evolution reaction of cobalt nickel Prussian blue analogues FTO/[Co-Fe]. He observed an interesting property of Prussian blue analogues, that is, some PBAs show enhancement in OER reactions under the influence of a magnetic field.

Cobalt and nickel-based catalysts are the two famous non-platinum grouped metal (PGM) based catalysts explored. Previous studies indicate that cobalt surfaces have a high propensity for the Tafel/Heyrovsky processes, which concludes that the recombination of 2 hydrogen atoms on the cobalt surface to make a hydrogen molecule is a very feasible process. Water dissociation from oxygen and hydrogen is a challenging and rate-determining step.

Given the aforementioned studies, my thesis focus is on catalysts synthesized with elements that are abundant on Earth, such as cobalt and nickel [86, 87, 88]. The main goal is to build an integrated experimental framework that combines the knowledge gained from the mentioned research projects. Notably, by including the simultaneous analysis of the hydrogen evolution reaction (HER) and oxygen evolution reaction (OER), this work adds a new dimension to external stimuli-assisted water-splitting devices as summarized in Fig 1.13. Beyond this, a ground-breaking step is performed by researching the whole process of water splitting in the context of external stimulants like solar light irradiation and magnetic fields, successfully addressing both HER and OER.

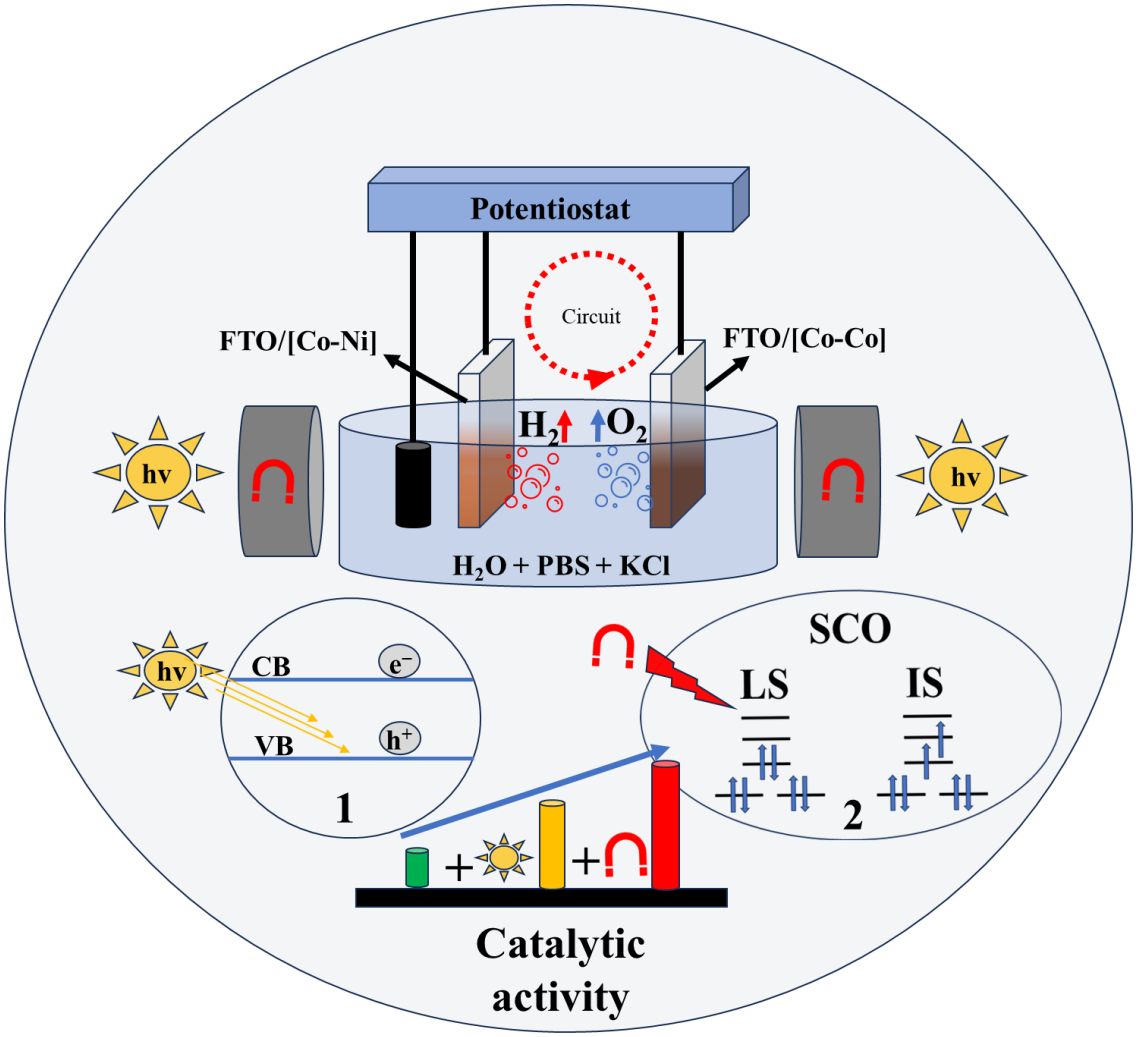

Fig 1. 13 Investigation of overall water splitting under solar light irradiation + magnetic field to enhance the catalytic activity featuring the 1) semiconducting effect and 2) spin crossover effect.

Chapter 2: Methods and Instrumentations

All the necessary characterizations were pursued at UNAM and the Chemistry Department of Bilkent University.

2.1. Synthesis Procedure For FTO/[Co-M], (M = Co, Ni)

2.1.1. Chemicals

All the chemicals were purchased from established commercial suppliers and used without any further purification. Potassium hexacyanoferrate(III) ($K_3Fe(CN)_6$), potassium hexacyanoferrate(II) trihydrate ($K_4Fe(CN)_6 \cdot 3H_2O$), and potassium chloride (KCl) were acquired from Sigma Aldrich. Cobalt(II) nitrate hexahydrate ($Co(NO_3)_2.6H_2O$) was sourced from Fischer Scientifics and Alfa Aesar. The precursors of potassium phosphate buffer solution (PBS), Potassium phosphate monobasic (KH_2PO_4), and Potassium phosphate dibasic (K_2HPO_4) were sourced from Sigma Aldrich. For all the experiments discussed below Millipore deionized water with a resistivity of 18 MΩ.cm. was utilized. The glass substrates utilized in the experiments were covered with fluorine-doped tin oxide (FTO), having a sheet resistance of 20 Ω/sq. and 2mm thickness.

All the experiments are performed with a three-electrode system, Gamry software. In this setup the FTO is connected to the working electrode, Ag/AgCl is used reference electrode while the counter electrode is platinum (Pt) wire of 15 cm. This Pt wire was provided in the official package of Gamry.

2.1.2. Preparation of FTO/[Co-Co] and FTO/[Co-Ni]

Before FTO/PBA preparation, an FTO electrode cleaning operation is carried out. Each FTO electrode is sequentially submerged for 15 minutes in a sonication fluid made up of deionized water, acetone, and ethanol. Then, for one hour prior to usage, the FTO electrode is maintained at 100 °C.

FTO/[Co-Co] and FTO/[Co-Ni] electrodes were prepared with two methods:

i) ***Hydrothermal technique***: [89] In this method, a 30 mL 20 mM cobalt nitrate solution was mixed well with 30 mL 0.1 M hexacyanocobaltate solution with the help of a sonicator at room temperature. An aqueous solution of PBA and FTO electrode having its conducting side downwards is immersed in a Teflon-lined stainless-steel autoclave. The sealed autoclave was kept in the oven for 1 h at 120 °C. The autoclave was left to cool down to room temperature,

and the FTO was collected and rinsed multiple times with deionized water. The as-prepared FTO was dried for 24 h at 50 °C.

ii) ***Electrodeposition technique***: [90] The 2-step electrodeposition method was employed to prepare FTO/PBA. After experimenting with a spectrum of parameters, the following procedure is developed:

First, 30 mL of 20 mM cobalt nitrate solution, supplemented with a supporting electrolyte KCl (0.1 M) was prepared in a 50 mL beaker and the solution is treated with cathodic bias of −0.9 $V_{Ag/AgCl}$ for a time span of 200 s to deposit metallic Cobalt on FTO electrode. A blue color on the FTO surface is obtained which indicates the formation of FTO[Co] Fig 2.1. Subsequently, the FTO electrode is rinsed thoroughly to eliminate any residue of KCl or any other potential impurity, and FTO[Co] was immersed in 0.1 M hexacyanocobaltate solution with KCl (0.1 M) under an anodic potential of 0.9 $V_{Ag/AgCl}$ for FTO/Co-Co, or in 0.1 M tetracyanonickelate with KCl (0.1 M) under the anodic potential of 1.02 $V_{Ag/AgCl}$ for FTO/CoNi. Both, the FTO/[Co-Co] and FTO/[Co-Ni] give brown color. The whole process is summarized in Fig 2.1. From SEM studies we concluded that this approach provides a controlled and refined method related to the roughness of the surface.

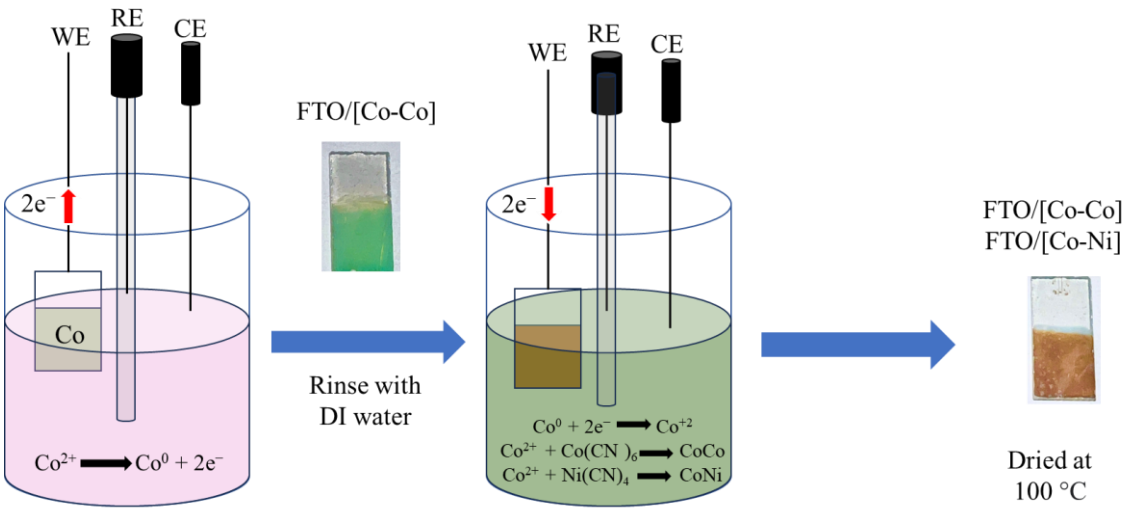

Fig 2. 1 Schematic diagram illustrating 3 electrode system for electrochemical deposition of PBA on FTO surface.

2.2. Scanning Electron Microscopy (SEM) Coupled with Energy Dispersive X-Ray Analysis (EDAX)

SEM-EDAX, combining scanning electron microscopy with energy dispersive X-ray spectroscopy, was skilfully utilized to provide an insight into surface morphology of the microscale characteristics of FTO/[Co-Co] and FTO/[Co-Ni] and measure the atomic ratio respectively. These analyses were executed through FEI – Quanta 200 FEG at 5 kV for SEM and 15 kV for EDAX analysis. For each study, multiple points were chosen, to get uniform analysis.

2.3. Powder X-ray Diffraction (P-XRD) Analysis

X-ray diffraction (XRD) analysis was investigated to elucidate the structural characteristics of the FTO/[Co-Co] composites and compared them to FTO and FTO[Co] samples. To employ these analyses Panalytical X'pert Multi-Purpose apparatus was utilized. This study aimed to elucidate the phase structures and attributed phase structures of FTO and electrodeposited PB composites on FTO.

2.4. Xray-Photoelectron Spectroscopy (XPS) Analysis

Xray-Photoelectron Spectroscopy (XPS), with Al K-Alpha radiation and a photon energy (hυ) of 1486.6 eV was used in the survey mode with an activated flood gun to neutralize the surface charge to determine the sample's elemental composition. The pass energy and step size for the flood gun were 30 eV and 0.1 eV, respectively. Peak positions were calibrated precisely by reference to the location of the C1s peak at 284.8 eV and then adjusting other peaks throughout the spectrum in accordance.

2.5. Fourier Transform Infrared Spectroscopy (ATR-FTIR) Analysis

This analytical method makes use of a Bruker ALPHA Platinum-ATR spectrometer, which can record spectra with wavenumbers between 4000 and 400 cm^{-1}. With a noteworthy resolution of 4 cm^{-1}, the spectral acquisition was carried out, ensuring precise spectral feature discrimination. To improve the reliability and precision of the data, 64 scans were gathered while the measurement was being done. The thorough examination of the FTIR spectra revealed important information about the complex chemical interactions and structural changes related to the development of the FTO/[Co-Co] and FTO/[Co-Ni].

2.6. Electrochemical Setup

To carefully investigate the water splitting performance of FTO/[Co-M], (M = Co,Ni), a broad spectrum of electrochemical techniques was utilized. These methods included two-electrode and three-electrode system electrocatalysis studies, cyclic voltammetry (CV), linear sweep voltammetry (LSV), chronoamperometry (CA), and cyclic voltammetry (CV) A Gamry Instruments Interface 1000 Potentiostat/Galvanostat was utilized in the electrochemical setup Fig 2.2a.

In this configuration, the reference electrode (RE) was Ag/AgCl (sat.), the counter electrode (CE) was 15 cm Pt wire in the official package with Gamry, and the working electrode (WE) was FTO/[Co-Co] for OER reactions and FTO/[Co-Ni] for HER reactions. Notably, all potentials were designated as $V_{Ag/AgCl}$ and referred against Ag|AgCl|KCl(sat.) as shown in (Fig 2.2b and c). Electrochemical studies were performed at pH 7, maintained by 0.1 M PBS solution as their electrolytic medium, together with 0.5 M KCl as a supporting electrolyte.

To account for the standardization, the potentials were converted into values relative to the reversible hydrogen electrode (RHE), abbreviated as VRHE, using the Nernst equation to adjust for standardization:

$$V_{RHE} = V_{Ag/AgCl}(V) + 0.059 \times pH + V^{o}_{Ag/AgCl}(V) \quad (21)$$

Here, $V_{Ag/AgCl}$ (V) stands for the standard potential applied vs the Ag/AgCl reference electrode, V_{RHE} stands for the potential applied vs RHE, and $V^{o}_{Ag/AgCl}$ (V) stands for the standard potential of the reference electrode, which is measured at (0.197 V_{RHE}).

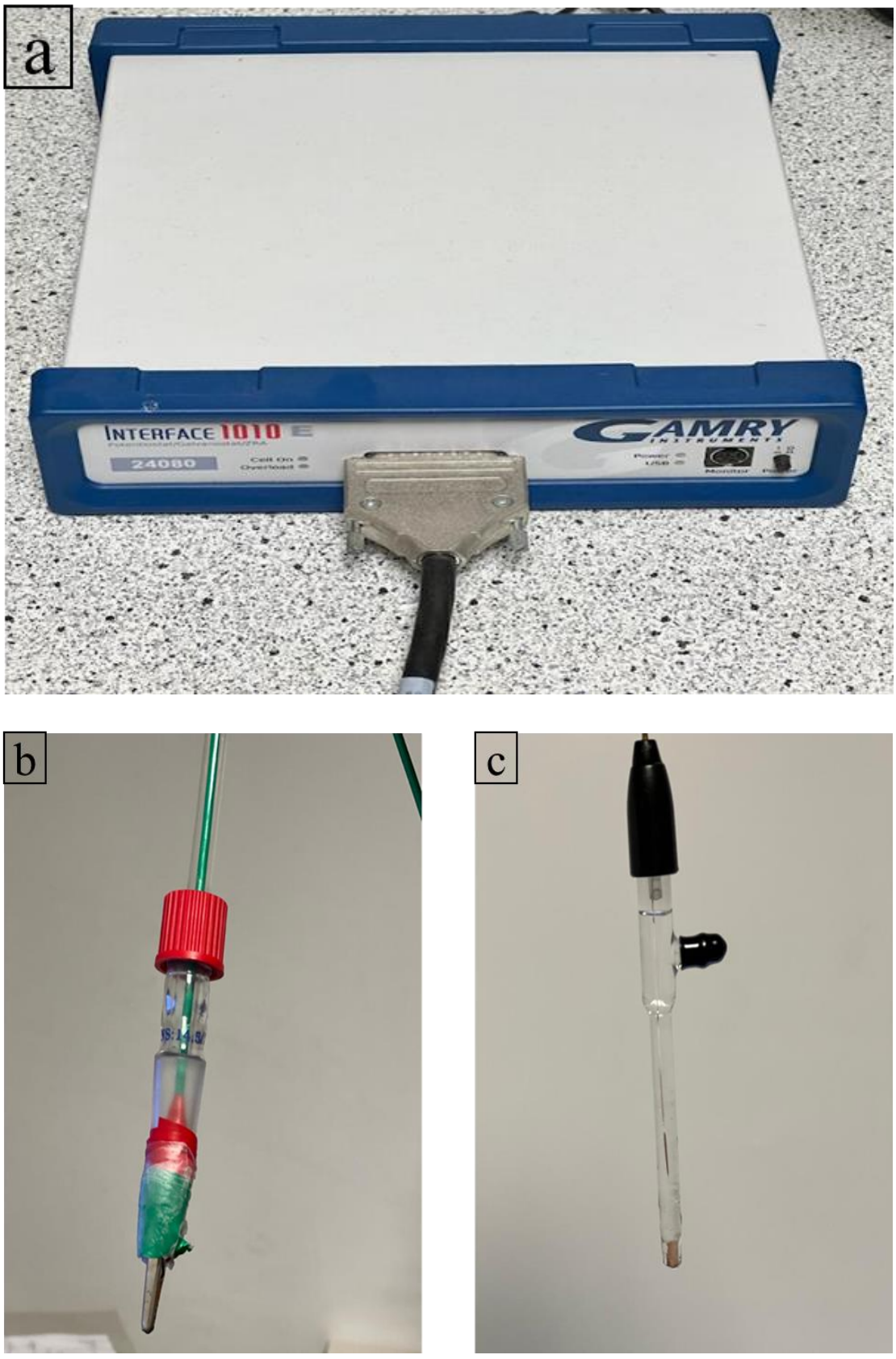

Fig 2. 2 a) Electrochemical set up with gamry featuring b) working electrode and c) reference electrode. (Karadas Research Group).

2.7. Magnetic Setup

Vibrating sample magnetometer (VSM) technology shown in (Fig 2.3) was utilized to conduct the study of catalyst performance under a magnetic field using the physical properties measuring system (PPMS-Quantum Design). The measurements of temperature-dependent magnetization (M-T) were made using an applied magnetic field of 500 Oe and temperatures ranging from 2 K to 300 K. The magnetic field strength provided by the system could range from 30 mT to 290 mT, and we studied a vast spectrum of investigation for Oxygen Evolution Reaction, (OER), Hydrogen Evolution Reaction, (HER) and Overall Water Splitting (OWS).

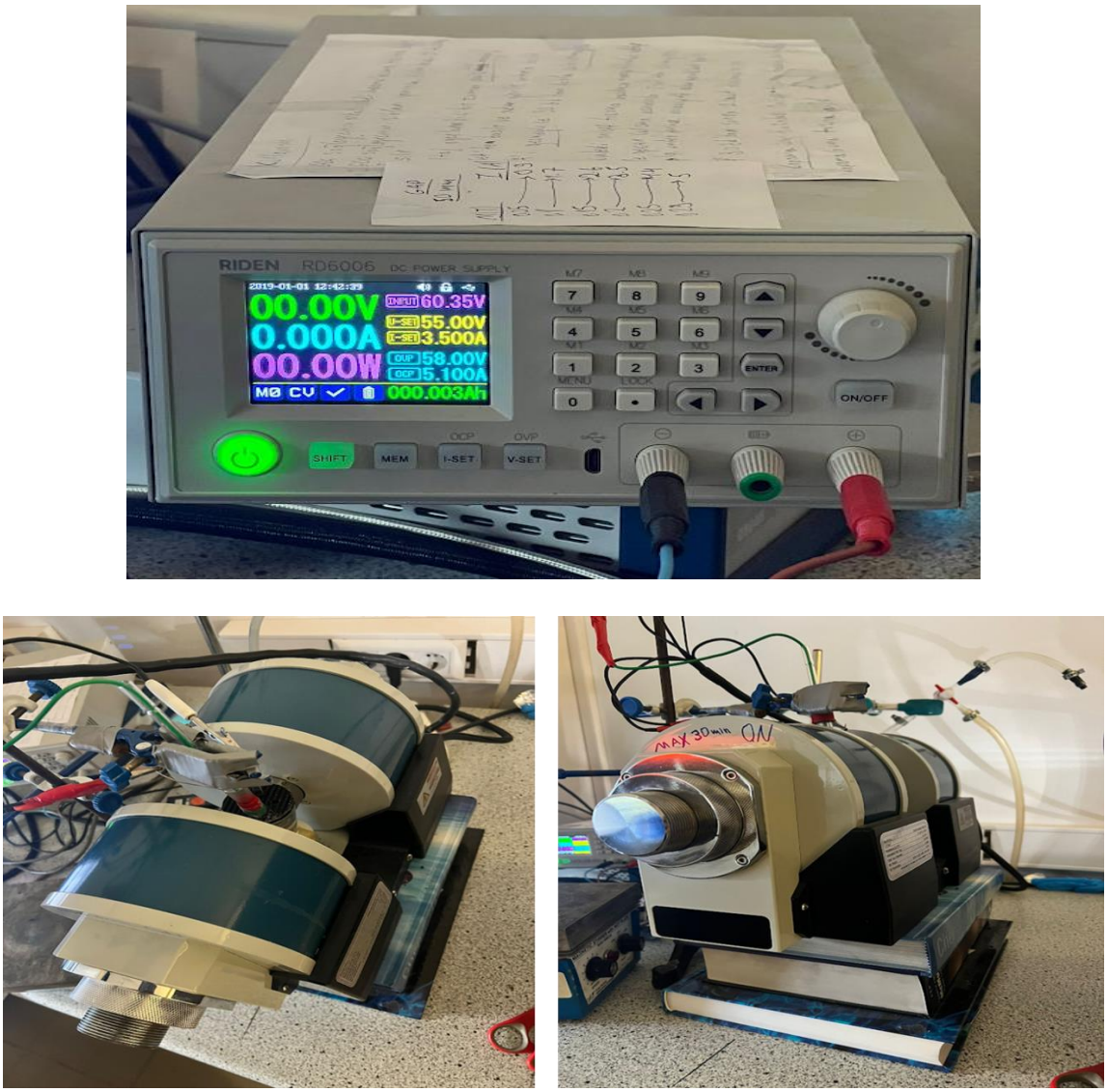

Fig 2. 3 Magnetic Setup utilized for our experiment (Karadas Research group).

2.8. Photocatalytic Setup

A 300 W Xenon lamp and an AM 1.5 global filter were installed in the solar light simulator (Sciencetech, Model SLB-300B) used in the experiment. This simulator was carefully calibrated to emit light at a rate of 100 milliwatts per square centimeter (mW/cm^2), representing the brightness of one sun. This arrangement was created to look at how sunlight affects the efficiency of the catalytic process.

Notably, no new filter was added at any point during the experimental processes. The Oxygen Evolution Reaction (OER), Hydrogen Evolution Reaction (HER), and Oxygen-Water Splitting (OWS) were among the reactions that used this arrangement. To establish repeatability and validate the recyclability of the experimental system, each of these reactions was carried out in a minimum of three cycles.

2.9. Calculating Surface Concentration of the Active Catalyst

By examining the relationship between the oxidation peak current (I) in milliamperes (mA) and the sweep rate (v) in millivolts per second (mV s1), the surface concentration of active catalytic sites present on the electrodes was identified. This was accomplished using a computation based on the equation below.

$$Slope = \frac{n^2 F^2 A \Gamma}{4RT} \tag{22}$$

In the provided equation

- n: Indicates how many electrons are involved in the redox process. It is set to 1 in this situation, denoting a one-electron transfer.
- F: the Faraday constant, has a value of 96485 s A/mol. It describes the electric charge that one mole of electrons carries.
- A: Refers to the coated electrode surface area, measured in square centimeters (cm^2). It indicates the extent of the electrode's active surface available for catalytic reactions.
- Γ: Signifies the surface concentration of active catalytic sites on the electrode's surface, expressed in moles per square centimeter (mol/cm^2).
- R: Ideal gas constant, has a value of 8.314 Kg m^2 s^{-2} K^{-1} mol^{-1}
- T: Temperature of the reaction, which is 298, the room temperature.

Chapter 3: Results Section

3.1. Synthesis Procedure For FTO/[Co-M], (M = Co, Ni)

3.1.1. Hydrothermal technique:

FTO/PBA prepared through hydrothermal technique [89] method affords an uneven coating of PBA on the FTO surface. (Fig 3.1) depicts the unnecessary peaks and low current density due to the rough surface of the catalyst on FTO posing the challenges.

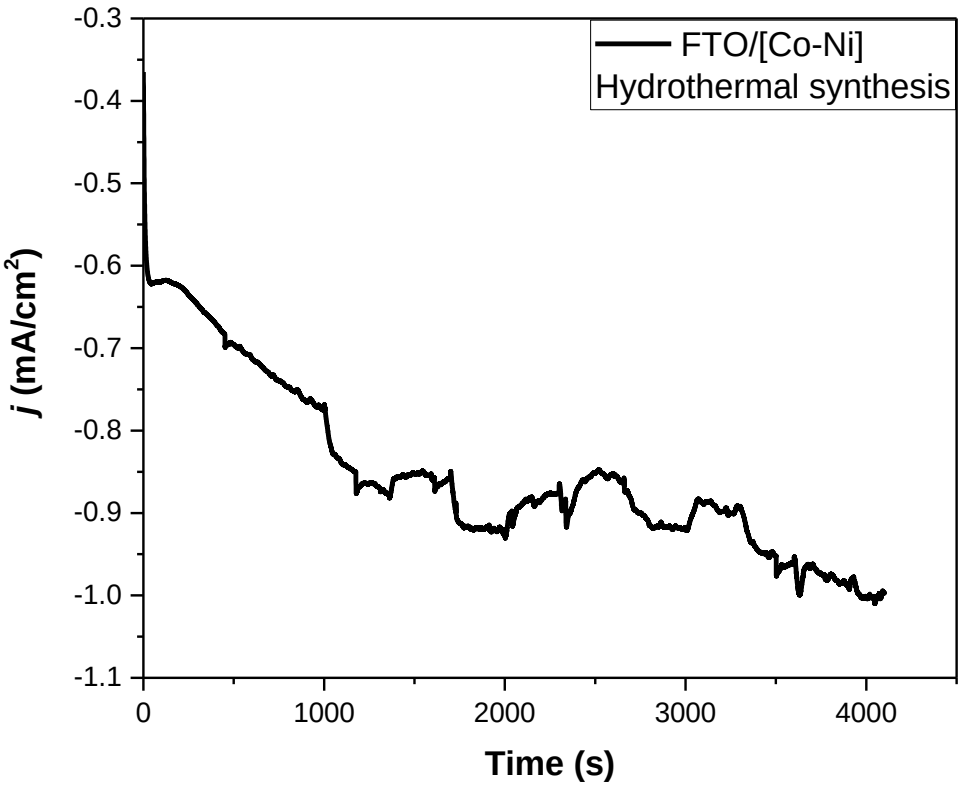

Fig 3. 1 CA profile of FTO/[Co-Ni] illustrating relatively low current density and undesired peaks.

3.1.2. Electrodeposition technique:

FTO/[Co-M], prepared through the electrodeposition technique [90] afforded a relatively smoother, uniform, and high-activity catalyst, compared to those prepared by the hydrothermal method. This is confirmed by all the characterization techniques and all the electrochemical experiments coming up in chapters 3, 4, 5, and 6. Therefore, all the electrodes used in this thesis are prepared with the electrodeposition method.

3.2. FTO/[Co-M] (M = Co, Ni) Characterization

In order to comprehend the electronic and surface morphological attributes inherent in the FTO/[Co-Co] and FTO/[Co-Ni] electrodes, a number of characterization techniques including SEM, EDAX, XRD, ATR-FTIR, and XPS were employed.

3.2.1. Scanning Electron Microscopy and EDAX Analysis

Fig 3.2 shows scanning electron microscopy (SEM) pictures of the FTO electrode with electrodeposited metallic cobalt coating, abbreviated as FTO/[Co]. A highly developed microporous flower-like morphology with layered layers was revealed by the SEM investigation. These structures had sub-micron diameters between 1 and 2 μm, and they were evenly distributed across the whole FTO surface. FTO/[Co] preparation step is similar in both FTO/[Co-Co] and FTO/[Co-Ni] cases. EDAX analysis of FTO/[Co] illustrated in Fig 3.3 confirms the presence of cobalt.

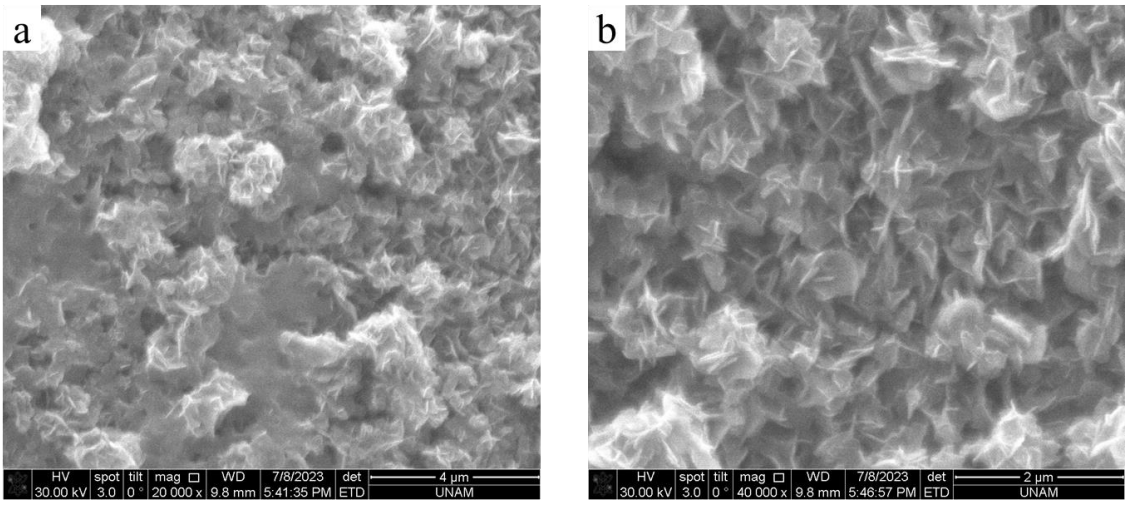

Fig 3. 2 SEM images of FTO/[Co] (a) 20,000x magnification and (b) 40,000x magnification.

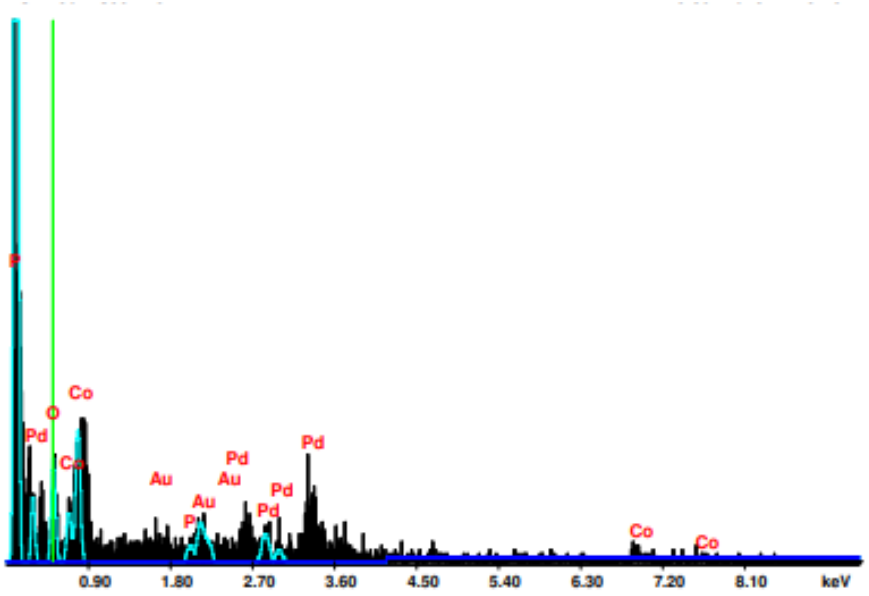

Fig 3. 3 EDAX analysis of FTO/[Co]**.**

SEM images for electrodeposited PBA FTO/[Co-Co] illustrated in Fig 3.4a and b and PBA FTO/[Co-Ni] Fig 3.4c and d were achieved to probe the surface morphology. They showed uniformity in particle size ranging from 1-2 μm and layered structures grown in thread-like shapes. On the contrary, for FTO/[Co-Ni], porous needle-like structures were grown with a huge range of 100 nm to 3 μm. The EDAX analysis shown for FTO/[Co-Co] in Fig 3.5 and for FTO/[Co-Ni] in Fig 3.6 respectively confirms the presence of cobalt in FTO/[Co-Co], and Co and Ni in FTO/[Co-Ni] in the equimolar ratio of 3.21% Co to 3.34% Ni, between the two elements.

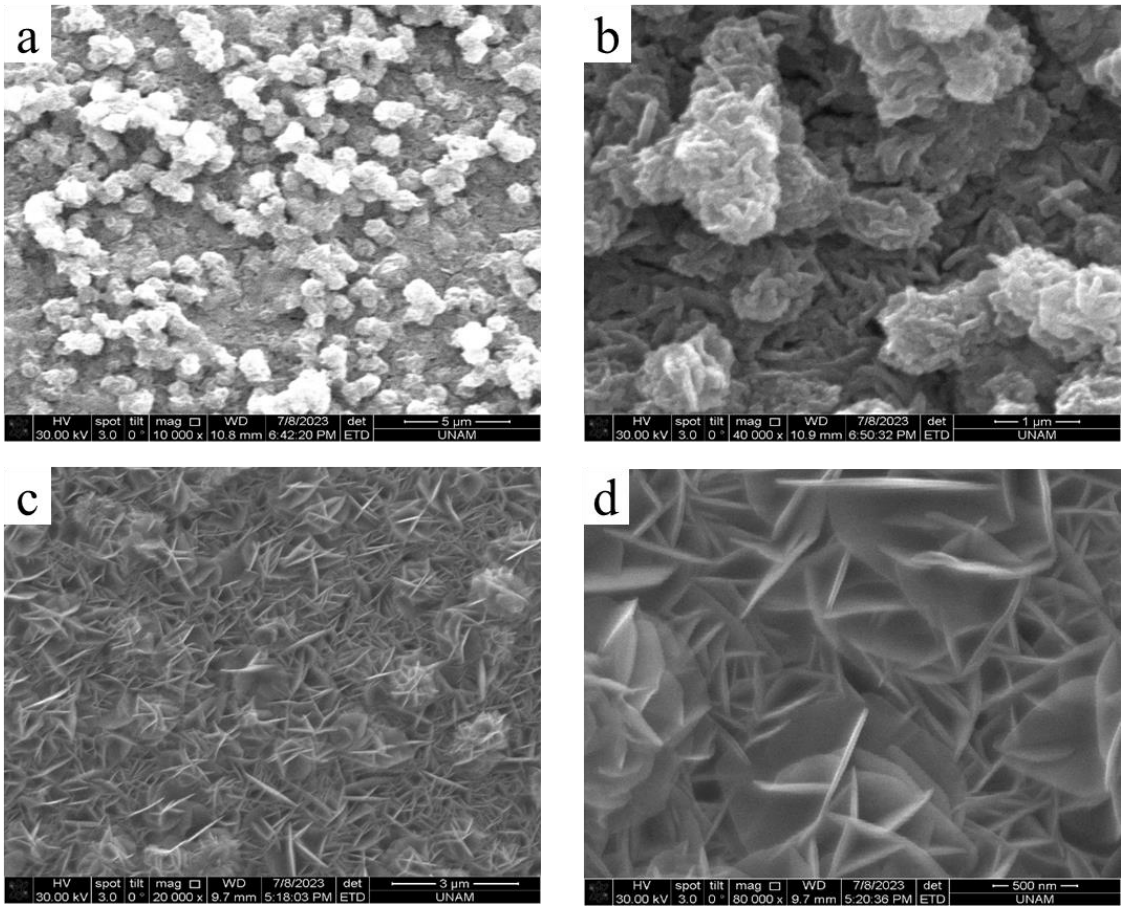

Fig 3. 4 SEM images of fresh FTO/[Co-Co] (a) 10,000x magnification, (b) 40,000x magnification and SEM images of fresh FTO/[Co-Ni] (c) 20,000x magnification, (d) 80,000x magnification.

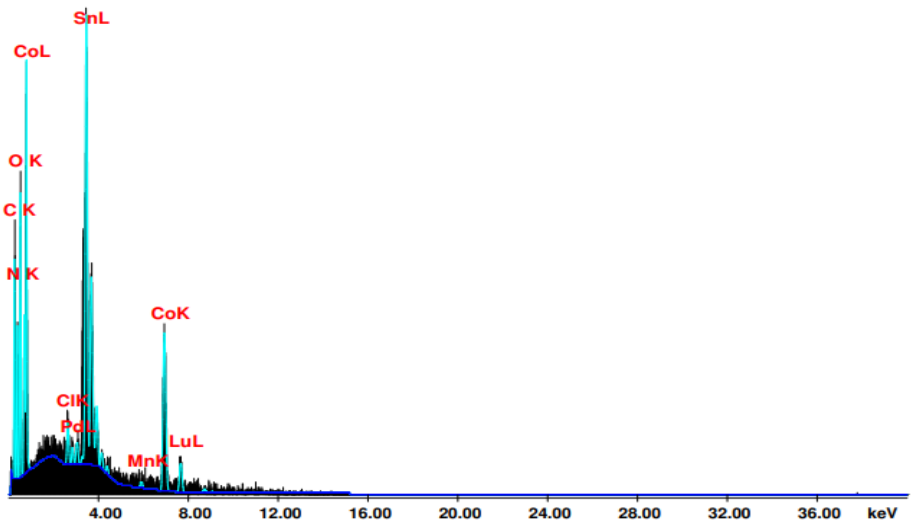

Fig 3. 5 EDAX analysis, the elemental insights of FTO/[Co-Co].

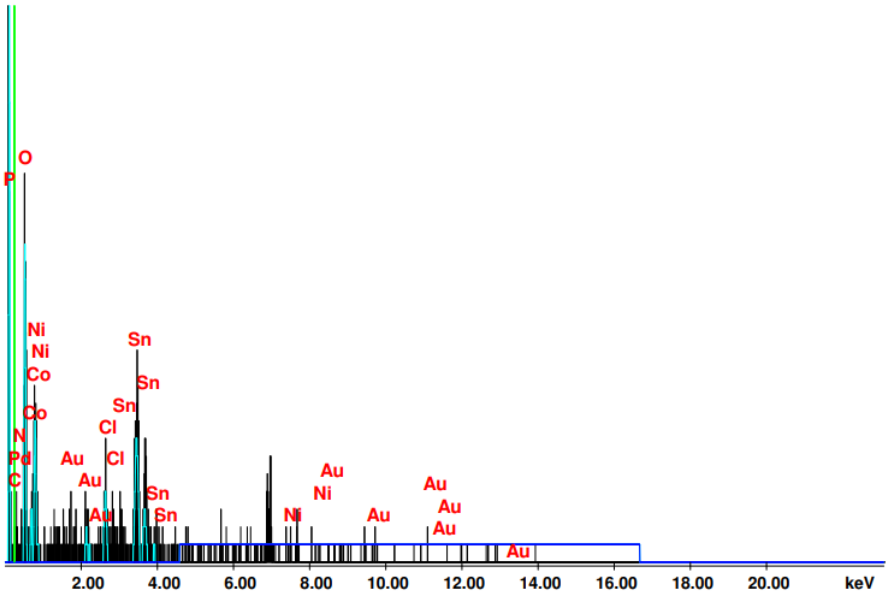

Fig 3. 6 EDAX analysis, the elemental profile of FTO/[Co-Ni].

3.2.2. XRD Analysis

All the electrodes exhibit characteristic diffraction patterns of FTO labeled as circles. Notably, the metallic cobalt exhibits two relatively weaker diffraction features at 11° and 29°. In contrast, these features are not observed for FTO/[Co-Co] and FTO/[Co-Ni], indicating that the metallic cobalt is completely oxidized to yield [Co-Co] PBA (Co^{II}-Co^{III}). Remarkably the asterisk-annotated peaks shown by FTO/[Co-Co] in Fig 3.7a and FTO/[Co-Ni] in Fig 3.7b, correspond to the characteristic patterns of cubic Prussian blue structure. XRD profiles thus confirm the formation of face-centered cubic (fcc) PB lattice structure, closely aligned with the Fm3m space group. The XRD pattern of the FTO[Co-Ni] discernible diffraction peaks occurring at approximately 25°, 32°, 36°, and 43°. These distinctive peaks are ascribed to the diffraction characteristics of the Co-Ni PBA [26]. Similarly, XRD patterns of FTO/[Co-Co] features prominent peaks around 17°, 24°, 35°, 39°, 51°, 58° and 60° are attributed to Co-Co PBA[[58, 59].

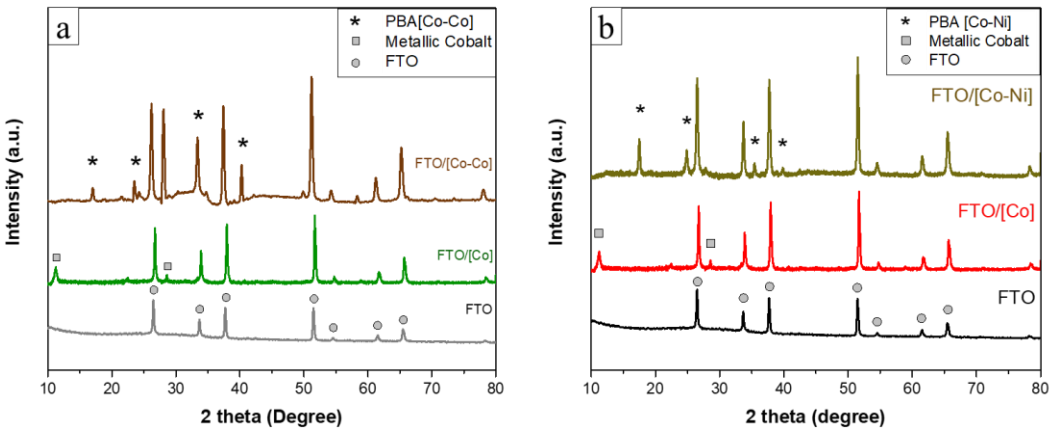

Fig 3. 7 XRD patterns compared to FTO and FTO/[Co] for (a) FTO/[Co-Co], and (b) FTO/[CoNi].

3.2.3. XPS Analysis

To check the oxidation states of the elements in the materials XPS analysis (X-ray Photoelectron Spectroscopy) was performed for FTO/[Co-Co] and FTO/[Co-Ni].

Fig 3.8a illustrates the XPS spectra of C-1s and K-2p while Fig 3.8b represents the Co-2p. Our focus was on researching the metal sites in a networked structure connected by cyanide groups. Previous studies have demonstrated that there is typically a partial oxidation effect when metal ions are connected by cyanide bridges [76]. The metals in PBA i.e., cobalt and nickel feature their 2p peaks in the binding energy region of 770 eV to 880 eV [91]. C-1s and K-2p give prominent peaks in the binding energy regions of 285 eV and 293.4 eV. Two distinct peaks at energies 781 eV and 797 eV, which correspond to various cobalt states, can be seen in the Co-2p spectrum. The research reveals that the material's structure is preserved throughout the electrochemical process in the instance of the PB (Prussian Blue) layer in FTO/[CoFe] [92].

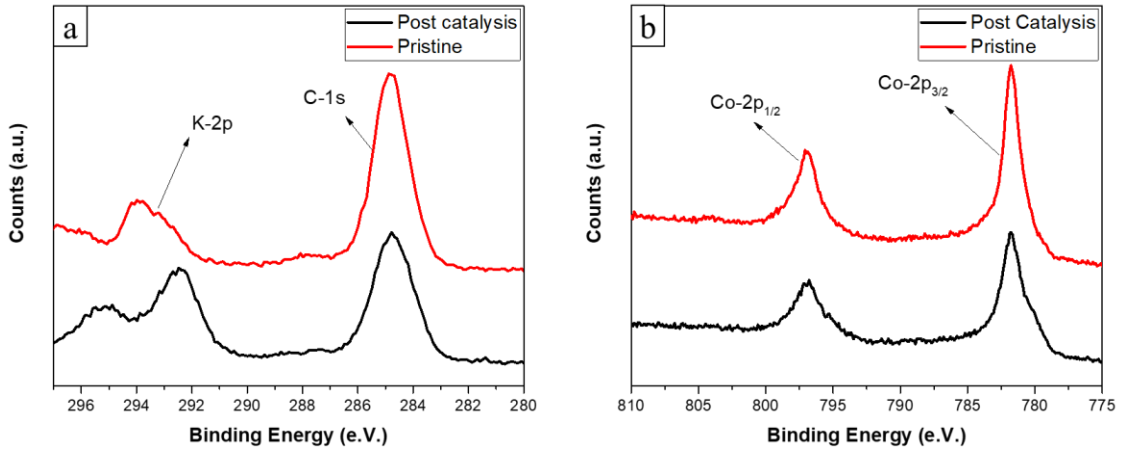

Fig 3. 8 XPS analysis for pristine and post-catalytic FTO/[Co-Co] (a) C-1s and K-2p peaks and (b) Co-$2p_{3/2}$ and Co-$2p_{1/2}$ peaks.

Similarly, XPS analyses were performed for the FTO/[Co-Ni] before and after the catalytic performance as shown in Fig 3.9a and b. Fig 3.9a corresponds to the Co-2p peaks in the binding energy region of 782 eV in Co-$2p_{3/2}$ and 796 for Co-$2p_{1/2}$. However, Fig 3.9b features the characteristic peaks for Ni $2p_{3/2}$ at around 856 eV and Ni-$2p_{1/2}$ at around 874 eV [93].

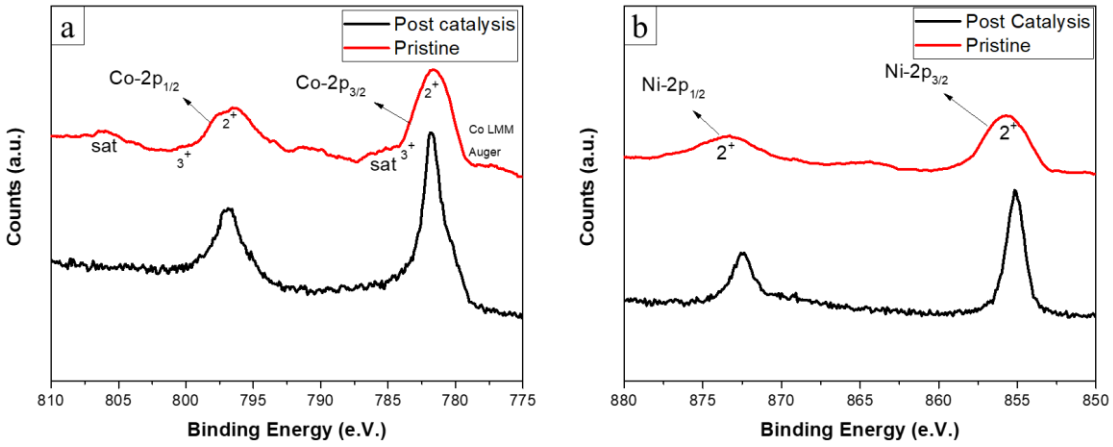

Fig 3. 9 XPS analysis for pristine and post FTO/[Co-Ni] (a) Cobalt peaks and (b) Nickel peaks.

3.2.4. ATR-FTIR Analysis

A systematic FTIR-ATR analysis was executed to confirm the synthesis of FTO/[Co-Co] and FTO/[Co-Ni] PBA as depicted in Fig 3.10. The FT-IR data unveils distinct peaks at around 2176 cm^{-1} attributed to the Co^{II}-CN-Co^{III} in FTO/[Co-Co] and 2164 cm^{-1} attributed to the Co^{II}-CN-Ni^{III} in FTO/[Co-Ni] coordination motif within the structural arrangement. The peak at around 1610 cm^{-1} and broadband at 3385 cm^{-1} observed by both samples are ascribed to H_2O bending modes and O-H bending modes, respectively. Notably, the presence of sharp peaks within the fingerprint region at around in ATR spectra at around 580 cm^{-1} and 430 cm^{-1} correspond to the Co^{II}-N and Co^{III}-C/Ni^{II}-C bond stretches distinctly elucidating the chemical connectivity within the structure [90].

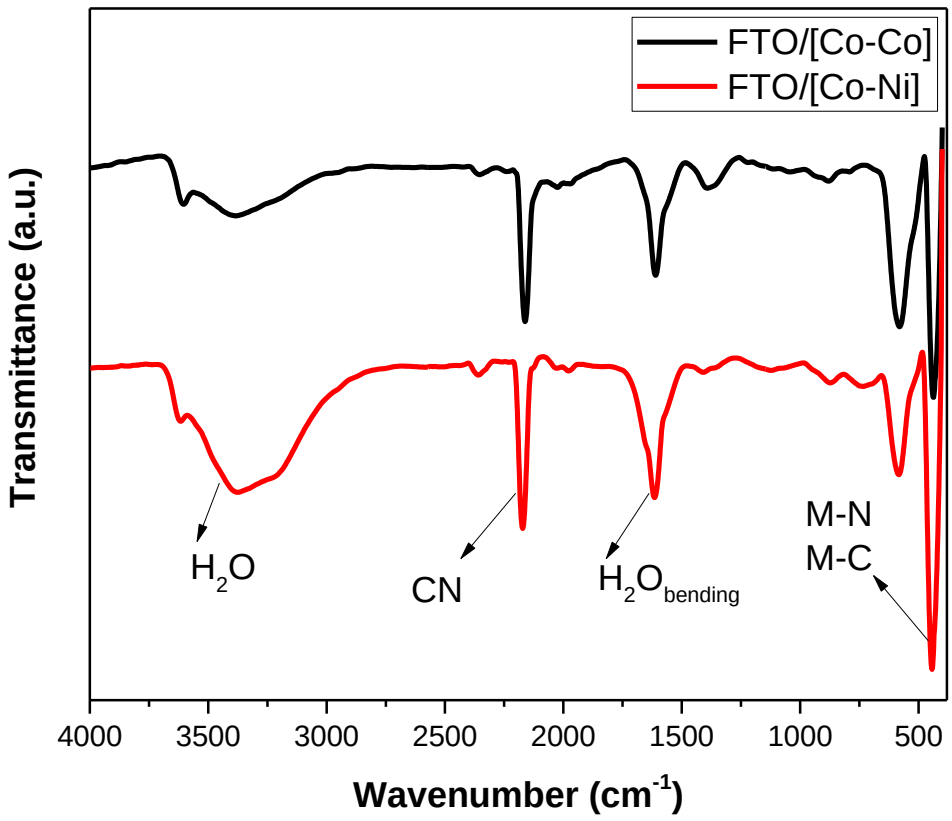

Fig 3. 10 ATR-FTIR spectrum of FTO/[Co-Co] and FTO/[Co-Ni] featuring prominent stretches.

3.2.5. Calculating the Surface Concentration of the Catalyst

The surface of the catalyst is consistently maintained to be 1 cm^2 throughout the thesis, however, the actual parameter to understand the catalytic performance is the surface concentration of the active catalyst on the surface of FTO/[Co-Co]. By investigating the relation between current (I), and sweep rate, (equation 2 chapter 2.9) we were able to find the active surface concentration to be, 53.01 $nmol/cm^2$ for FTO/[Co-Co] and 63.41 $nmol/cm^2$ for FTO/[Co-Ni] which is comparatively better than previously reported electrodeposition depending upon the size of ligands for example Ahmad et al. synthesized the catalysts through co-precipitation techniques the active surface concentration to be 0.53, 10.01 and 0.32 $nmol/cm^2$ for [Cobpy-Fe], [Co-Fe], and [Cophen-Fe] [94]. Fig 3.11 illustrates the aforementioned values of current (I) and sweep rate potential in mV for both FTO/[Co-Co] and FTO/[Co-Ni]. Similarly, Chalil Oglou et al. through electrodeposition method achieved almost similar active surface concentration of 49 $nmol/cm^2$, 34 $nmol/cm^2$ and 43 $nmol/cm^2$ for

FTO/[Co−Fe^{II}−NO], FTO/[Co−Fe^{II}] und FTO/[Co−Fe^{III}] because of following the same *protocols [85].

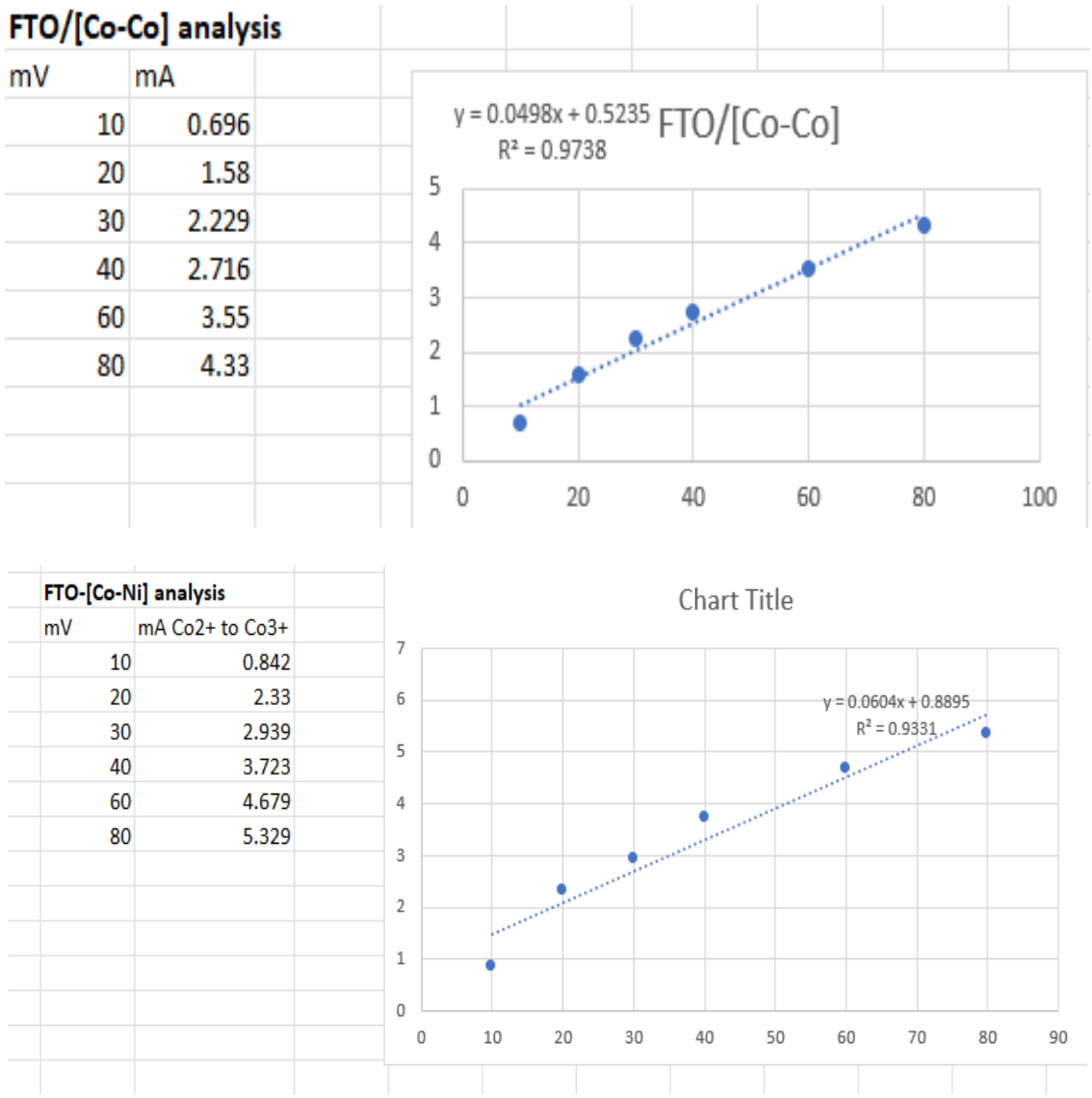

Fig 3. 11 Statistical data relating current (I) and sweep voltage aimed to measure Active surface area with equation 2 Chapter 2.9.

Chapter 4: Electrocatalytic water oxidation under magnetic and light field with FTO/[Co-Co]

A three-electrode setup was employed in the experimental technique for the oxygen evolution reaction (OER) studies. All the experiments were performed at pH 7, in a phosphate buffer solution (PBS 0.1 M) KCl was used as an electrolyte at room temperature. In all three-electrode experiments, Pt wire is used as the counter electrode, and an Ag/AgCl electrode was used as the reference electrode, which was used to create a constant electrochemical potential reference point so that the working electrode and counter electrode could have their electrochemical behavior quantitatively compared. The prepared FTO electrodes are used as working electrodes.

The stability of the FTO electrode presented a substantial difficulty during our electrocatalytic studies that were carried out under the influence of a magnetic field. A solution was required since our FTO electrode is inherently vulnerable to magnetic field displacement. We came up with a unique 3D-printed stage to solve this problem, which is shown in Fig 4.1. This stage's careful positioning and construction ensured the electrode's immobility throughout the trial. Notably, the stage's measurements were adjusted to ensure that the electrode would fit perfectly. The height of the 3D-printed stage is 0.2 centimeters, which is the same as the electrodeposit we were using to cover the electrode's 1-centimeter height.

Fig 4. 1 Image of the 3D-printed stage for all the HER and OER reactions under magnetic field.

4.1. Magnetic Field-Assisted OER Studies

4.1.1. Linear Sweep Voltammetry Studies

Linear sweep voltammetry (LSV) curves were obtained to acquire distinct profiles as shown in Fig 4.2 in which the black trace depicts the OER current density in the absence of the magnetic field the red profile indicates the catalysis under a magnetic field of 200 mT (milli tesla). This investigation encompasses a potential range from 0.2 V to 1.6 V. There is an enhancement of 0.34 mA/cm^2 at an overpotential of 997 mV (which is 1.6 V, the LSV limit for our studies) in the current under the magnetic [63]. The overpotential required to achieve 1 mA/cm^2 current density is recorded as 570 mV and remains the same under the magnetic field of 200 mT as well. Overall, an enhancement of 3.3% is achieved under magnetic field.

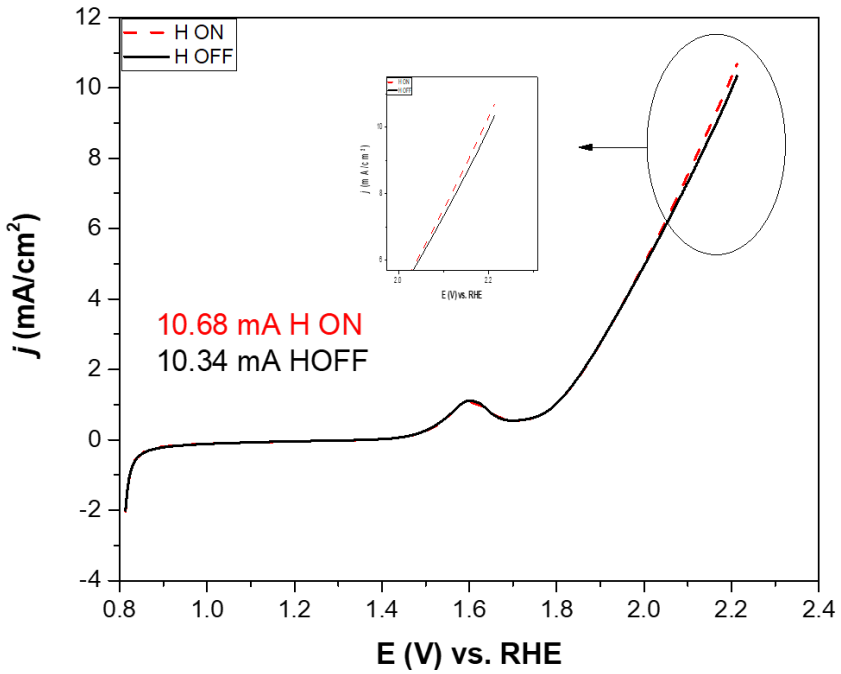

Fig 4. 2 LSV Profile of FTO/[Co-Co] illustrating magnetic enhancement (Inset: Magnified image of the enhancement zone).

Similarly, the enhanced current density was also confirmed through the Tafel slope shown in Fig 4.3, which is 88 mV/dec for FTO/[Co-Co] with no stimulus, and 87 mV/dec under the influence of magnetic field. Tafel plots were constructed for OER mechanisms by conducting LSV measurements under different external stimuli Fig 4.3 and Fig 4.8, aiming to figure out the nature of enhancement from the two external stimuli is different.

Notably, we observed a linear correlation between the logarithms of steady-state current densities and over-potentials, spanning the overpotential range of 560 mV to 580 mV. Within this range, we calculated Tafel slopes, which fell within the range of 88 to 95 mV per decade illustrating the lowest for solar light irradiated LSV.

Comparing our obtained Tafel slopes for FTO/[Co-Co] and FTO/[Co-Ni] with those previously reported by Alsac et al. [58] We observed minute differences. These disparities can largely be attributed to distinct preparation methods, Specifically, PBA-modified electrodes on FTO surface, prepared method exhibited slightly lower Tafel slopes.

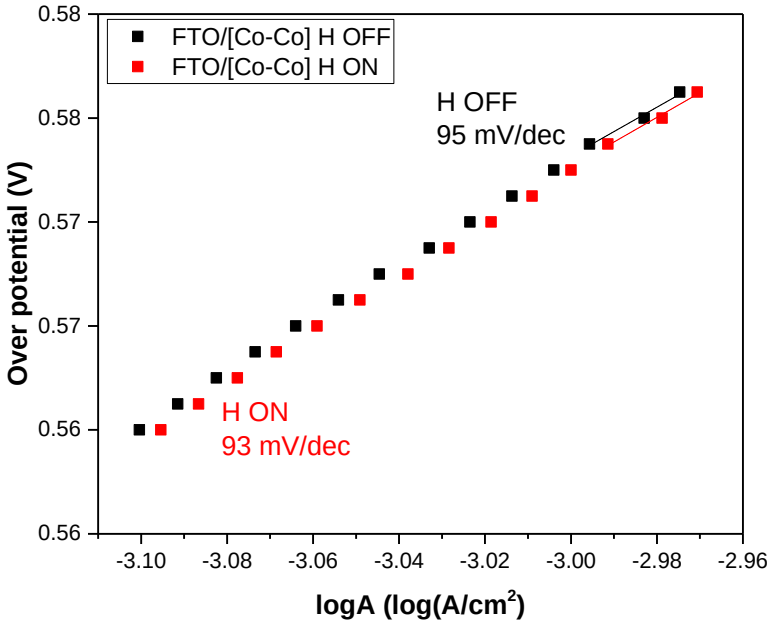

Fig 4. 3 Tafel slope FTO/[Co-Co] under magnetic field.

4.1.2. Chronoamperometric Studies

Chronoamperometry measurements were performed to investigate the stability of the catalyst and to further investigate the effect of the magnetic field on the catalytic activity. An overpotential of 949 mV was applied for 2100 seconds. As could be seen from Fig 4.4, the CA profile initially reveals a steady state current density for around 500 seconds, and a magnetic field of 200 mT was applied for 300 seconds. This process was repeated subsequently, and the pattern of CA measurements continued until the experimental endpoint at 2100 seconds. A steady profile obtained indicates the stability of the catalyst. The maximum current density achieved during this CA profile at 949 mV overpotential was 4.6 mA/cm^2. From the given profile it is evident that the results are reproducible and an enhancement of 10.7 % is achieved.

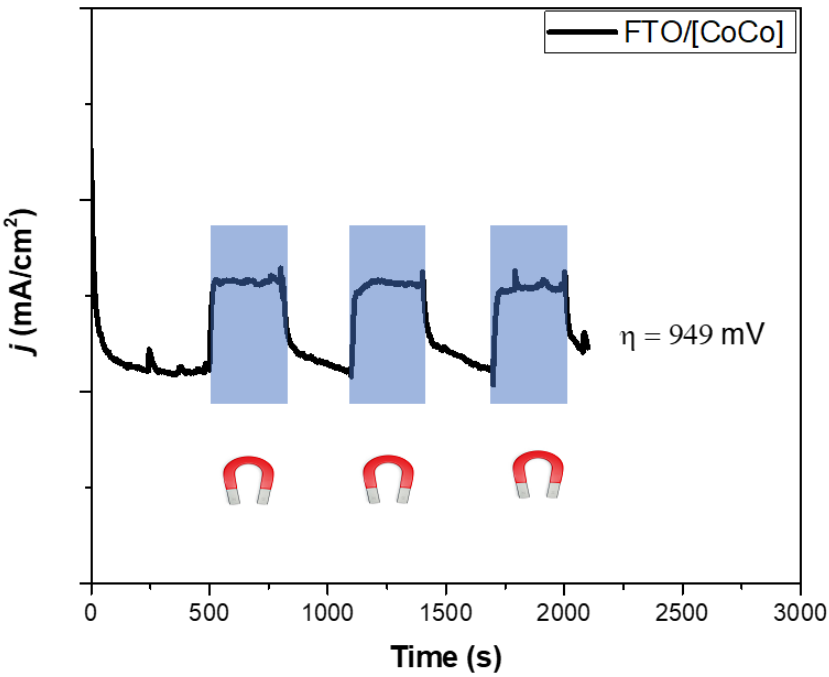

Fig 4. 4 CA profile obtained for FTO/[Co-Co] OER at η = 949 mV.

Following this, CA profiles as shown in Fig 4.5 were investigated at various overpotentials under a magnetic field of 200 mT under the same conditions. Interestingly we observed that as the overpotential decreases, the relative enhancement in the current density also decreases.

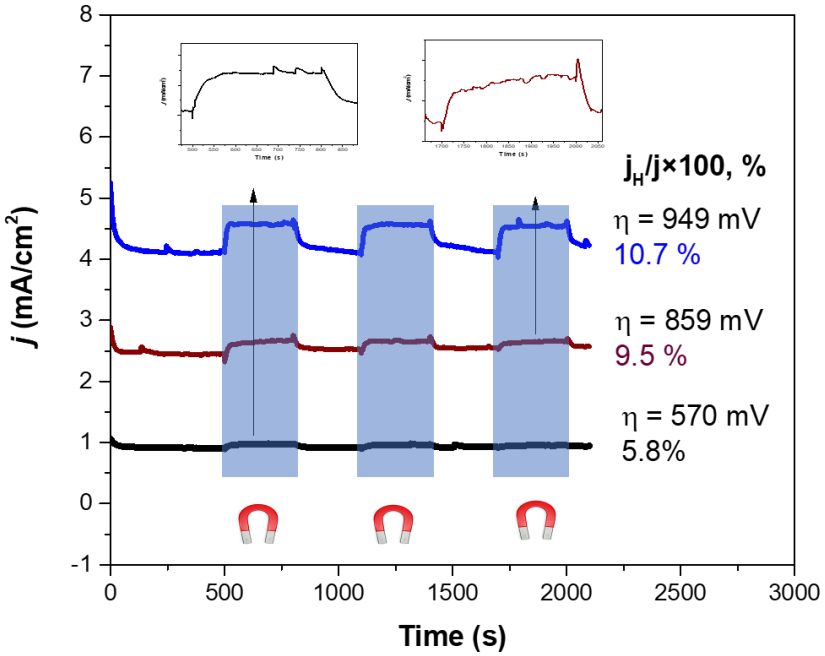

Fig 4. 5 CA Profile obtained for FTO/[Co-Co] at different overpotential (Insets: zoomed images of graphs that are not clear in the main graph).

After this, a CA measurement profile was obtained at varying magnetic fields shown in Fig 4.6, which reveals a direct relationship between the applied magnetic field and current density.

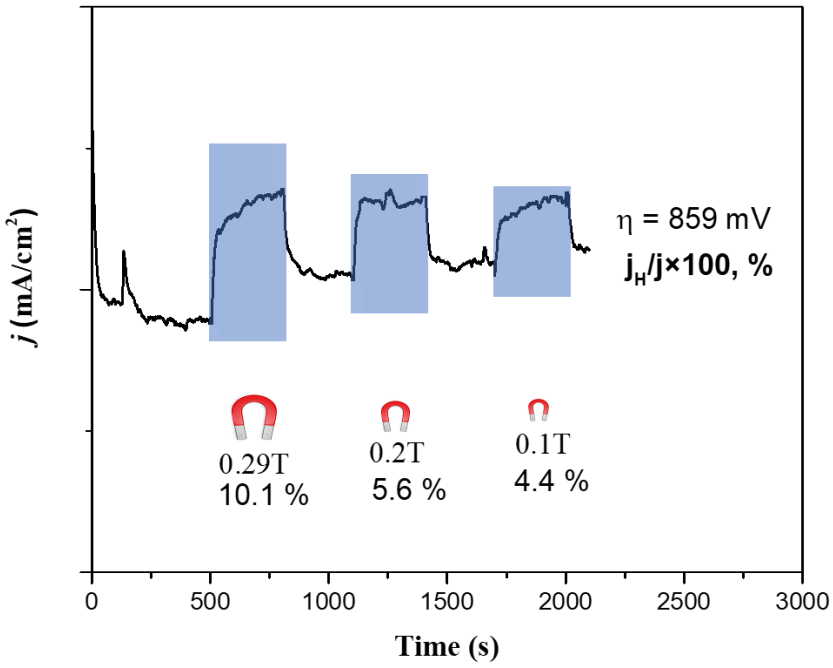

Fig 4. 6 CA profile obtained for FTO/[Co-Co] OER at η = 859 mV various magnetic field.

4.2. Solar Light-Assisted Studies

4.2.1. Linear Sweep Voltammetry Studies Under Light Irradiation

Linear sweep voltammetry profile was performed to investigate the effect of solar light on the catalytic performance of FTO/[Co-Co] as shown in Fig 4.7. The experiment was performed from 0.2 V to 1.6 V vs Ag/AgCl. A xenon lamp (300 W-100 mW/cm^2) was used as the light source. Under solar light irradiation, an enhancement of 0.74 mA/cm^2 is achieved in the current density while the overpotential required to achieve 1 mA/cm^2 current density is 570 mV. The peak at around 1 V is attributed to the $Co^{+2}/^{+3}$ redox process [58].

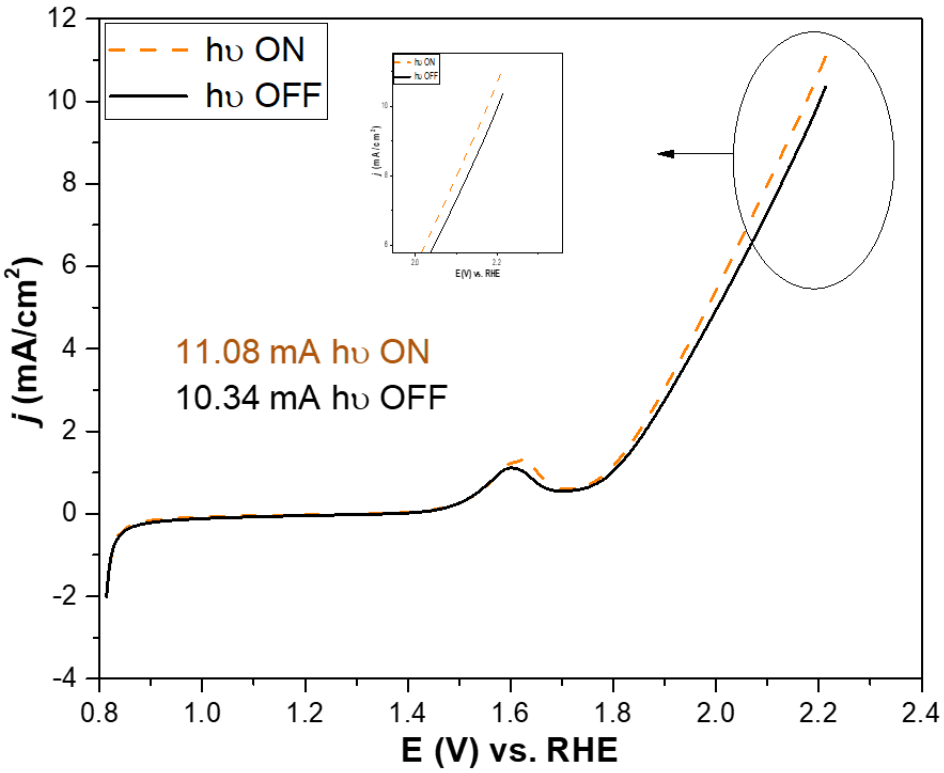

Fig 4. 7 LSV Profile of FTO/[Co-Co] with and without solar light irradiation (Inset: Magnified the enhancement zone).

As the similar Tafel slopes indicate similar OER kinetics, we observed difference in Tafel slopes for the one under magnet and solar light, as could be seen in Fig 4.8. This indicates that the OER reaction kinetics under solar light are different and faster from the one under magnetic field.

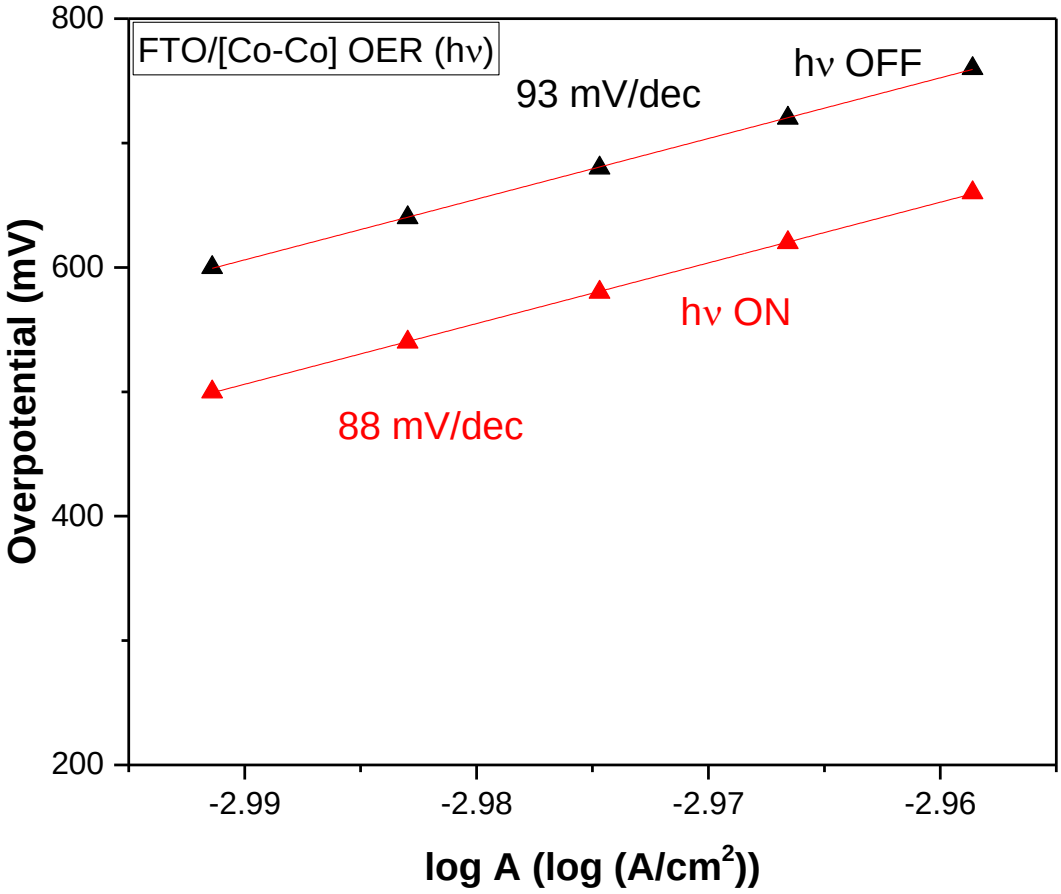

Fig 4. 8 Tafel slope FTO/[Co-Co] under magnetic field.

4.2.1.1. Relative LSV Profile

Under solar light irradiation, we observed a permanent enhancement in the catalytic performance of PBA FTO/[Co-Co]. This fact is in good agreement with Fig 4.8 where the last LSV profile (rightmost) illustrates the difference between i) the black-colored LSV without light, ii) the orange with light, and iii) the red without light after a long CA measurement. This behavior is backed by the CA profile of FTO/[Co-Co] shown in Fig 4.8 and 4.10

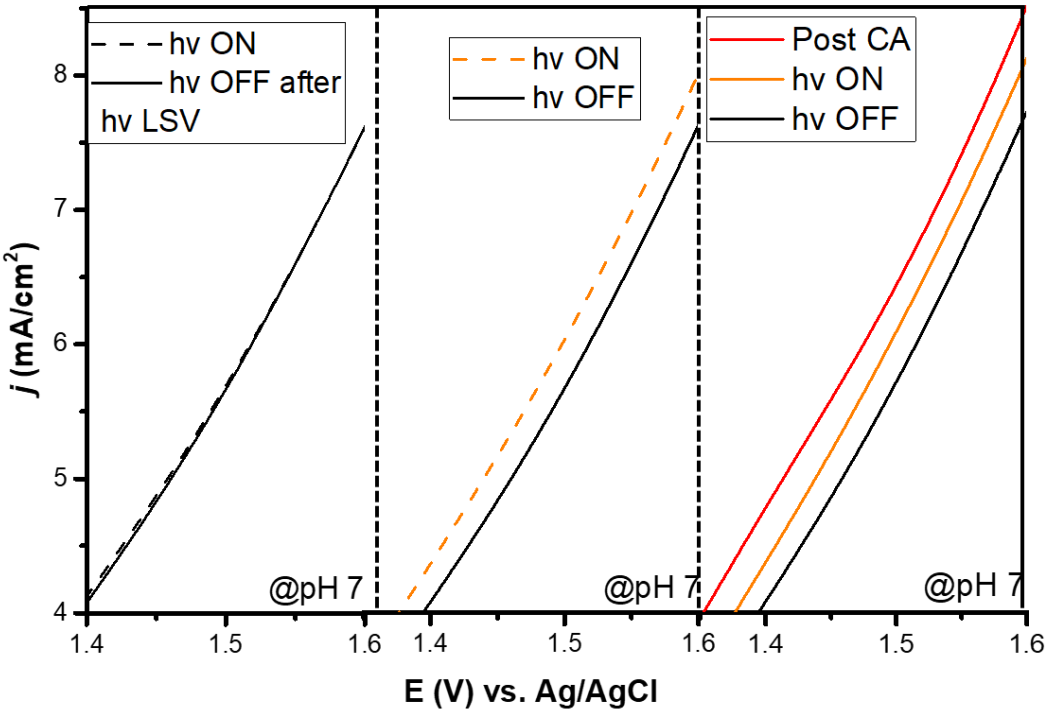

Fig 4. 9 Relative LSV profile of FTO/[Co-Co] with and without solar Light irradiation.

4.2.2. Chronoamperometric Studies Under Solar Light Irradiation

In order to investigate the stability and long-term behavior of solar light irradiation, a CA profile was obtained with FTO/[Co-Co] at 859 mV overpotential shown in Fig 4.9. The CA profile was initially stabilized in the first 500 seconds and then the system was exposed to solar light. The profile showed an average enhancement of 9.03% and the results are reproducible as could be seen from the three repeated cycles.

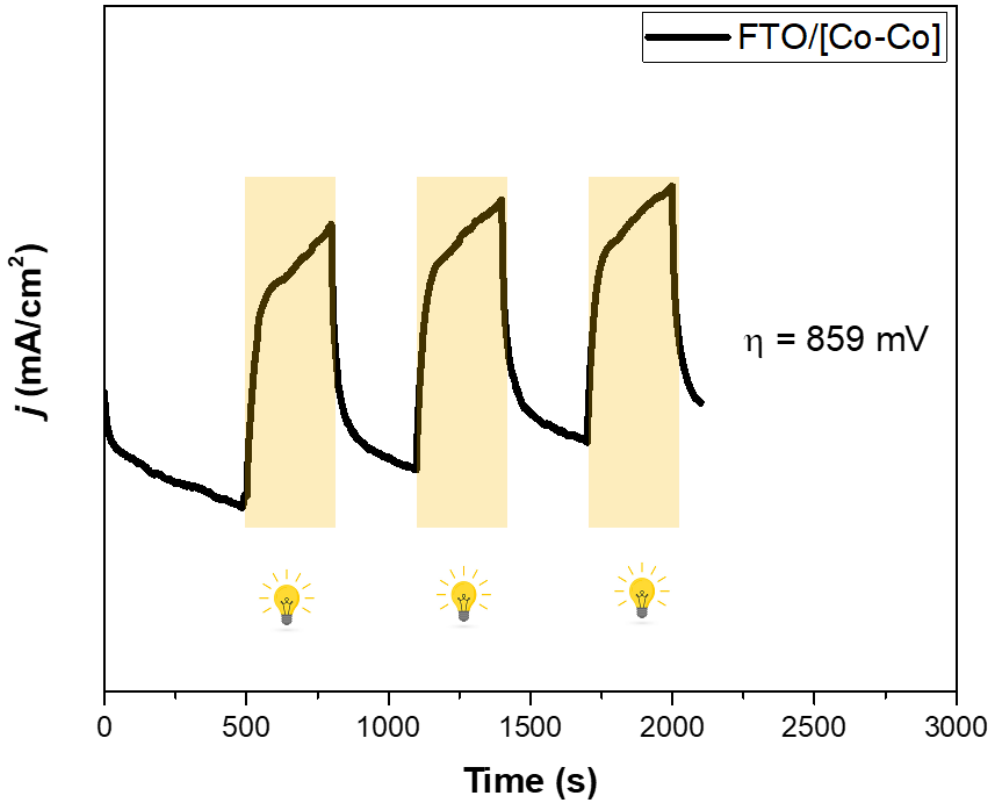

Fig 4. 10 CA profile of FTO/[Co-Co] under light irradiation.

CA experiments at varying overpotentials were performed, which interestingly reveals an inverse relationship between the overpotential and the relative enhancement. Furthermore, a permanent enhancement due to solar light irradiation is obtained, which indicates that the catalytic activity of the post-catalytic electrode is enhanced Fig 4.10. This effect was not seen when the catalyst was exposed to the magnetic field. The results are summarized in Table 4.1.

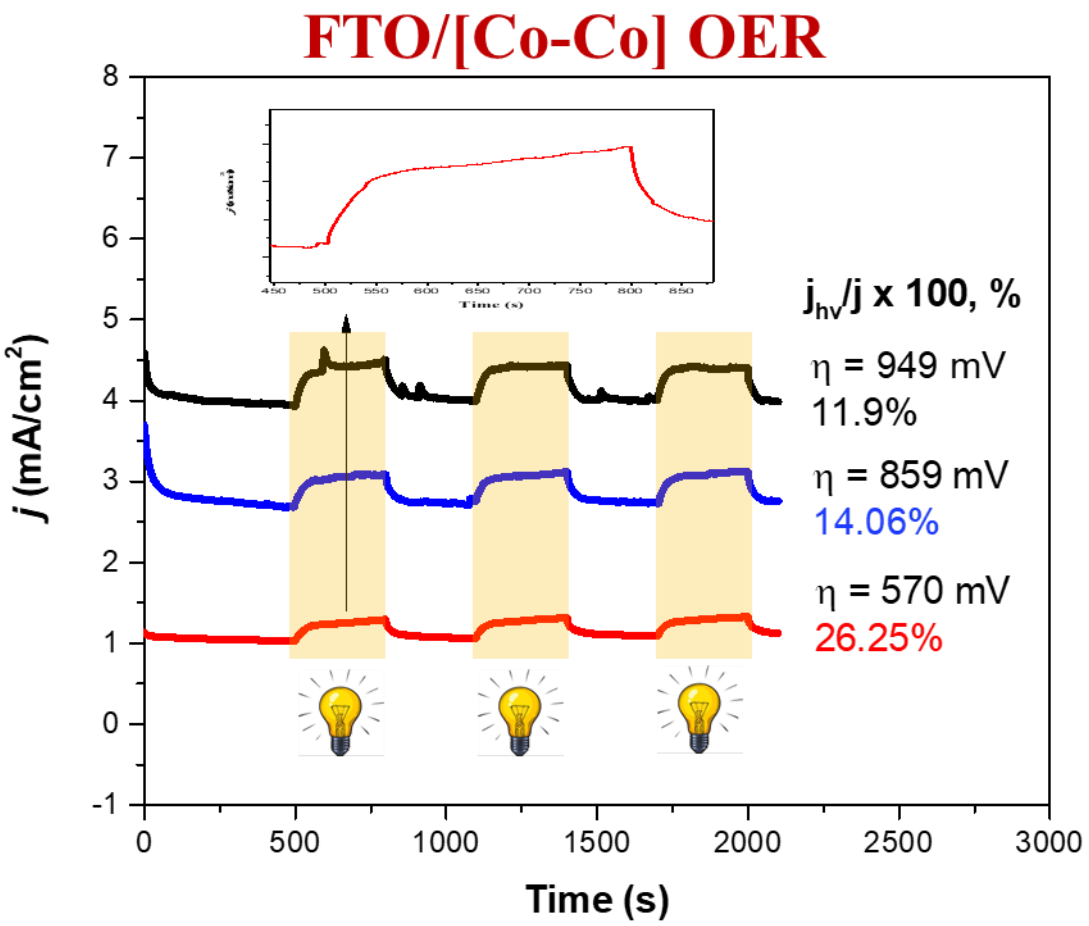

Fig 4. 11 CA Profile of FTO/[Co-Co] illustrating Light enhancement at different overpotentials(inset: Showing the red graph enhancement which is not very prominent in the main graph)

We also performed a long-term chronoamperometric experiment to combine the effect of both stimuli. As can be seen from Fig 4.11 with a magnet, an average enhancement of 10.7% is achieved under a magnetic field of 200 mT, while it is 11.9% under solar irradiation Furthermore when the light was switched on during the application of magnetic field i.e., at 3400 seconds, the profile clearly indicates that they exhibit a combined effect to yield an overall enhancement of 22.5%.

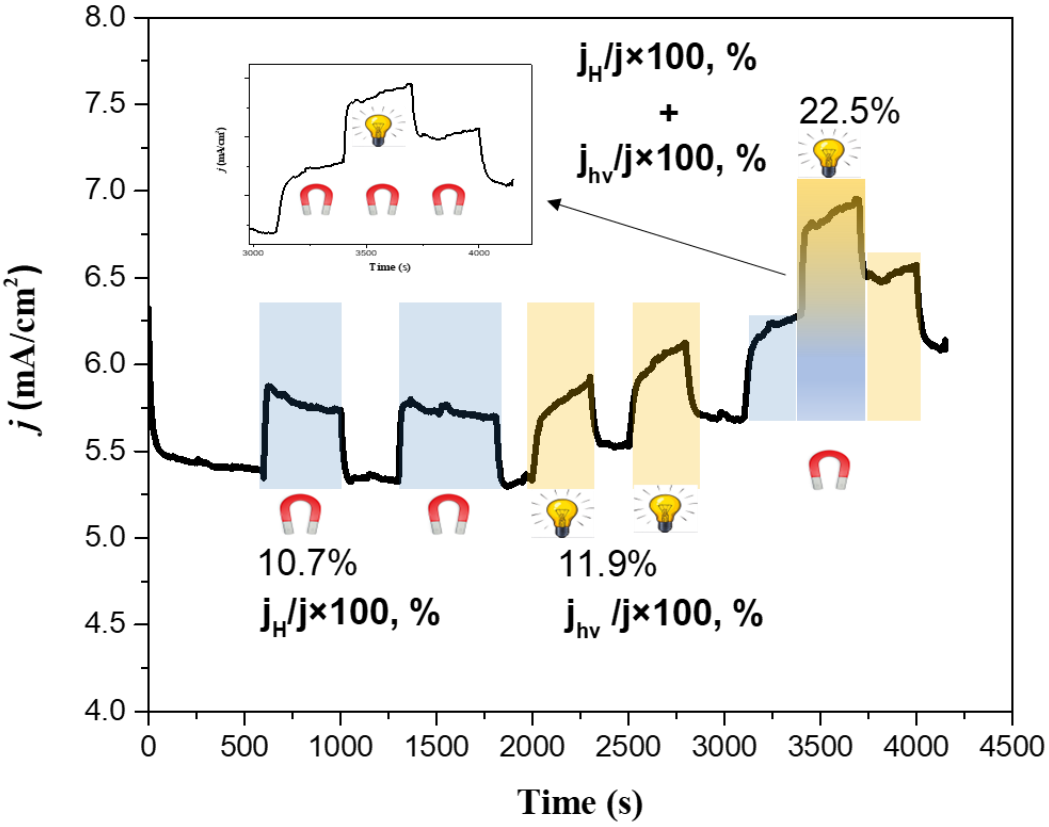

Fig 4. 12 CA Profile of FTO/[Co-Co] illustrating the combined effect of light and magnet.

4.2.2.1. Catalyst Stability

In order to evaluate the catalyst's stability and confirm the catalyst's continued improvement in catalytic performance a long-term experiment was designed. As could be seen in Fig 4.12 The duration of this prolonged experiment included two hours of light exposure followed by six hours of no light. This experiment was carried out at a rather low overpotential of 570 mV, which was specifically designed to give the catalyst plenty of time to improve its effectiveness. This tactical decision was influenced by earlier research as shown in Fig 4. 10, which showed an inverse relationship between the magnitude of the overpotential, and the degree of the enhancement attained under solar light irradiation.

Exciting results were achieved from the entire study's findings. In particular, a striking net improvement of 193%, as graphically shown in Fig 4.12, was unquestionably attained. The continuous nature of this improvement, as shown by the constant current attained over an extended period, is particularly significant. It was noted that the attained current density did

not return to its initial value, which is significant since it shows that the FTO/[Co-Co] system's catalytic performance has continued to improve.

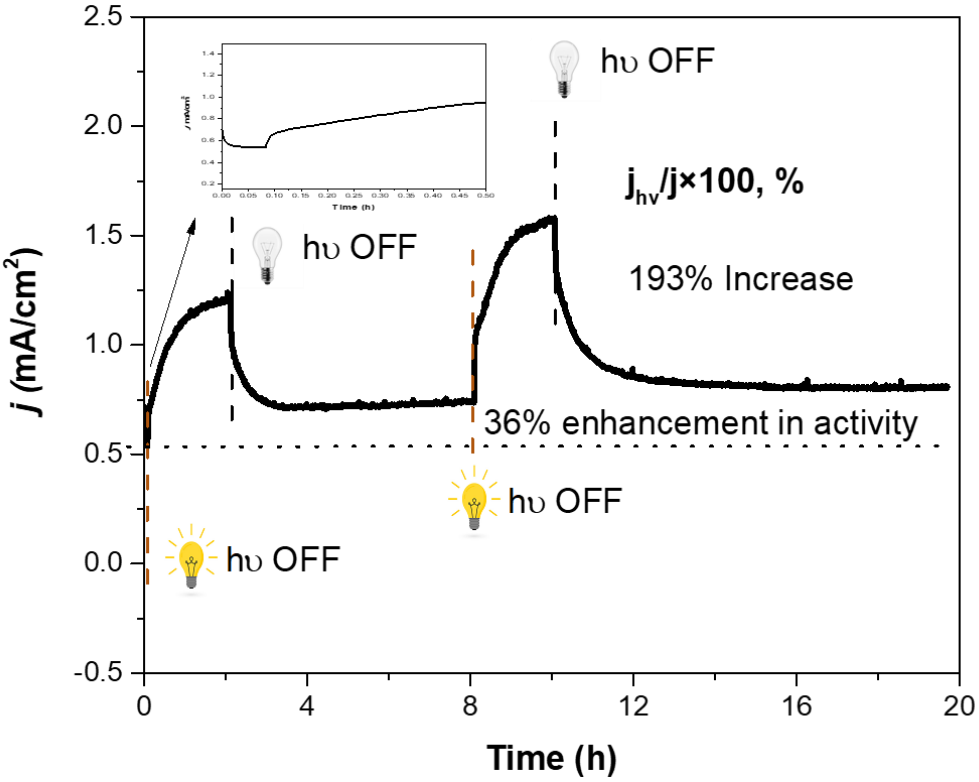

Fig 4. 13 CA profile of FTO/[Co-Co] under light for 2 h and dark 6 h.

These results were confirmed by the LSV profile as seen in Fig 4.13, where the black LSV profile leads the rest as it was done after a long time CA profile.

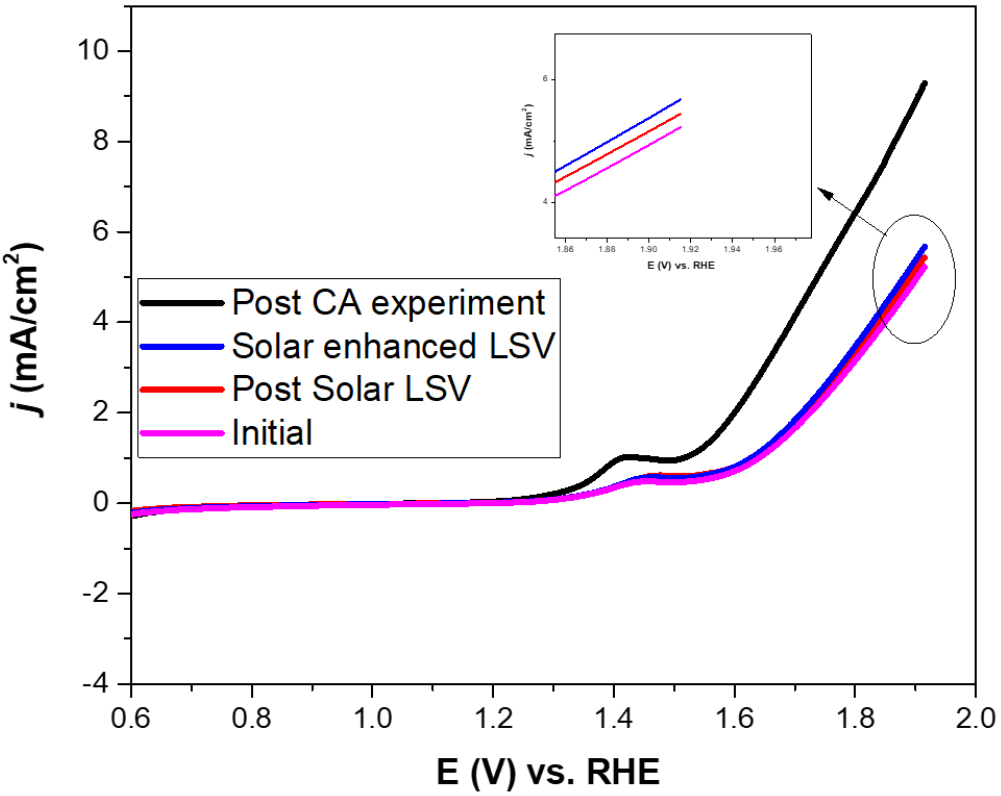

Fig 4. 14 LSV profile of FTO/[Co-Co] before and after 8 h experiment.

4.2.3. Temperature Profile for CA Under Solar Light Irradiation

In order to thoroughly examine how solar light irradiation affects the reaction's temperature dynamics, and thereby gain deeper insights into the underlying mechanisms governing light-induced enhancement, the temperature of the reaction at 570 mV overpotential was monitored using the previous experimental procedure that consists of two hours of exposure to light and six hours of darkness as illustrated by Fig 4.14. The principal findings of this experiment are that when the catalytic system was exposed to light, the temperature showed a gradual, unidirectional increase of about 5 to 6 ^{o}C, which was then followed by a decrease when the light source was blocked. An obvious correlation between temperature changes and reaction kinetics was established by the phase of temperature elevation, which stood out for exhibiting noticeably accelerated kinetics. Additionally, the overall temperature changed from the initial 25 ^{o}C to a maximum of 31 ^{o}C lowered back to 26 ^{o}C instead of 25 ^{o}C. A consistent improvement of 36% persisted even after the solar light was stopped, highlighting the significant impact that

temperature has on reaction kinetics. The complex interaction between temperature and the underlying reaction dynamics is the reason for the persistent increase in current density.

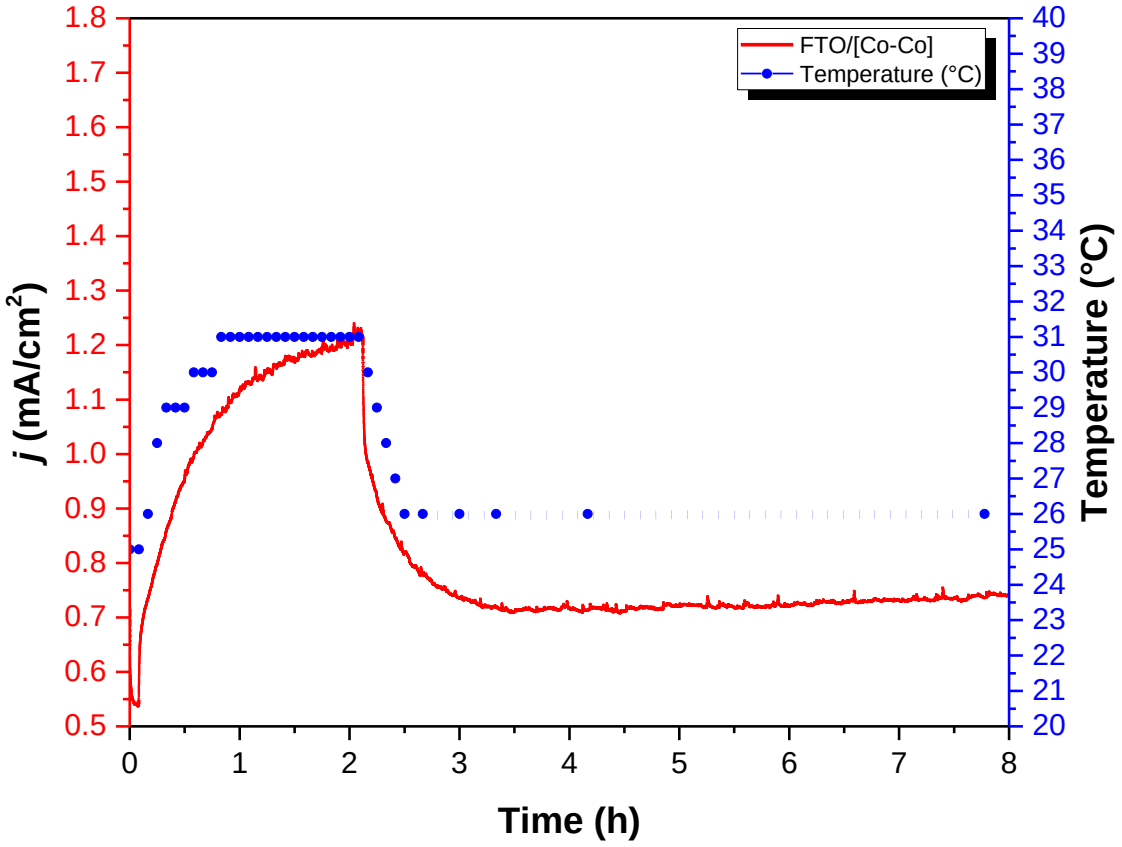

Fig 4. 15 Temperature recorded profile during (FTO/Co-Co) CA.

Table 4. 1 Summary of solar irradiated and under magnetic field OER studies.

Ƞ (mV/cm²)	j_m **mA/cm²**	$j_m/j\times100$, **%**	j_s **mA/cm²**	$js/j\times100$, **%**
997 (LSV)	0.34	3.3	0.74	7.1
949 (CA)	4.91	10.7	5.69	11.9
859 (CA)	2.42	9.5	3.96	14.1
570 (CA)	7.2	5.8	2.68	26.1

Chapter 5: Electrocatalytic hydrogen evolution reaction (HER) studies under magnetic field and solar light irradiation with FTO/[Co-Ni]

A three-electrode system utilized for OER reaction was used, also for HER studies. The FTO electrode was used as a working electrode and Pt wire was used as a counter electrode. Similarly, Ag/AgCl was used as a reference electrode. All experiments were conducted in KCl (0.5 M) solution as a supporting electrolyte at pH 7 in PBS (0.1 M) solution.

5.1. Magnetic Field-Assisted HER Studies

5.1.1. Linear Sweep Voltammetry Studies

The LSV profile was obtained to investigate the difference between the catalyst performance with and without a magnetic field. LSV profile was obtained from 0 to −1.6 V vs Ag/AgCl as illustrated in Fig 5.1. In both cases, i.e., the current density reached −1 mA/cm^2 at an overpotential of 114 mV. However, there is nearly no enhancement under the magnetic field.

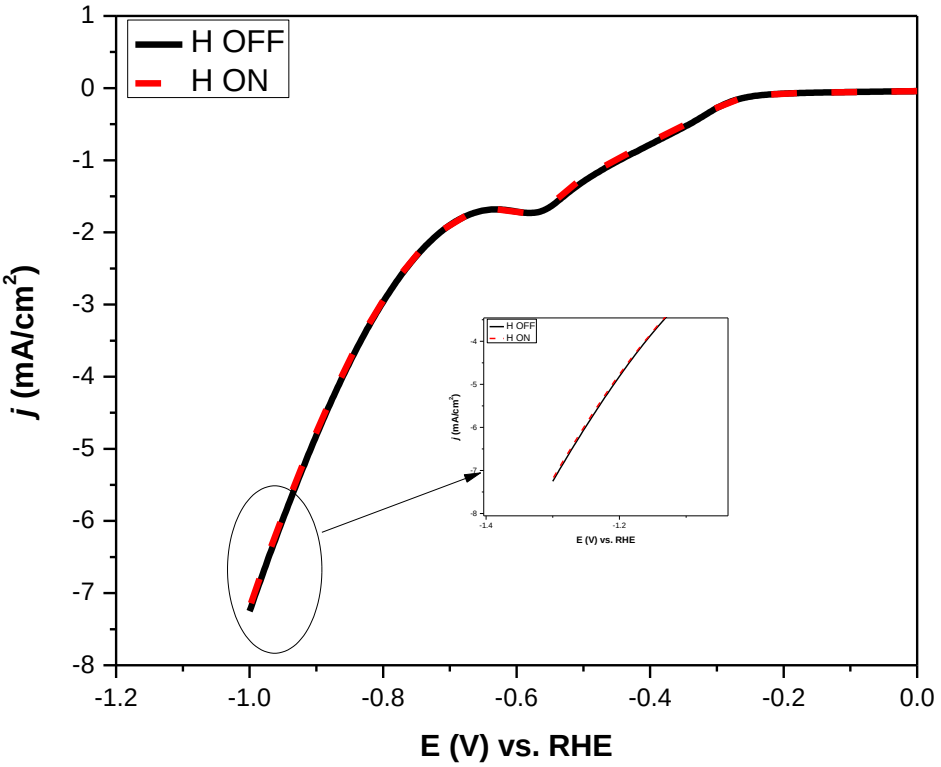

Fig 5. 1 LSV Profile of FTO/[Co-Ni] with and without magnet field.

5.1.2. Chronoamperometric Studies

Unlike OER reactions, an enhancement under a magnetic field was not anticipated since the HER process does not involve a spin crossover effect [80]. To confirm this, a long-term experiment of 2100 seconds was performed at a constant overpotential of 300 mV as shown in Fig 5. 2. There was a very small change of 1.4% in the current density under the magnetic field, which is attributed to the magnetohydrodynamic effect caused by the random accelerated motion of ions under the influence of the magnetic field [73]. Similar study was pursued by Hang-bo et al. by utilizing directly ferromagnetic materials such as CoNi@C as catalyst and discovered very small and unstable enhancements in catalytic activity [94]. Moreover, Jiawei et al. attributed the magnetic effect of HER enhancement under magnetic effect to using ferromagnetic material [95].

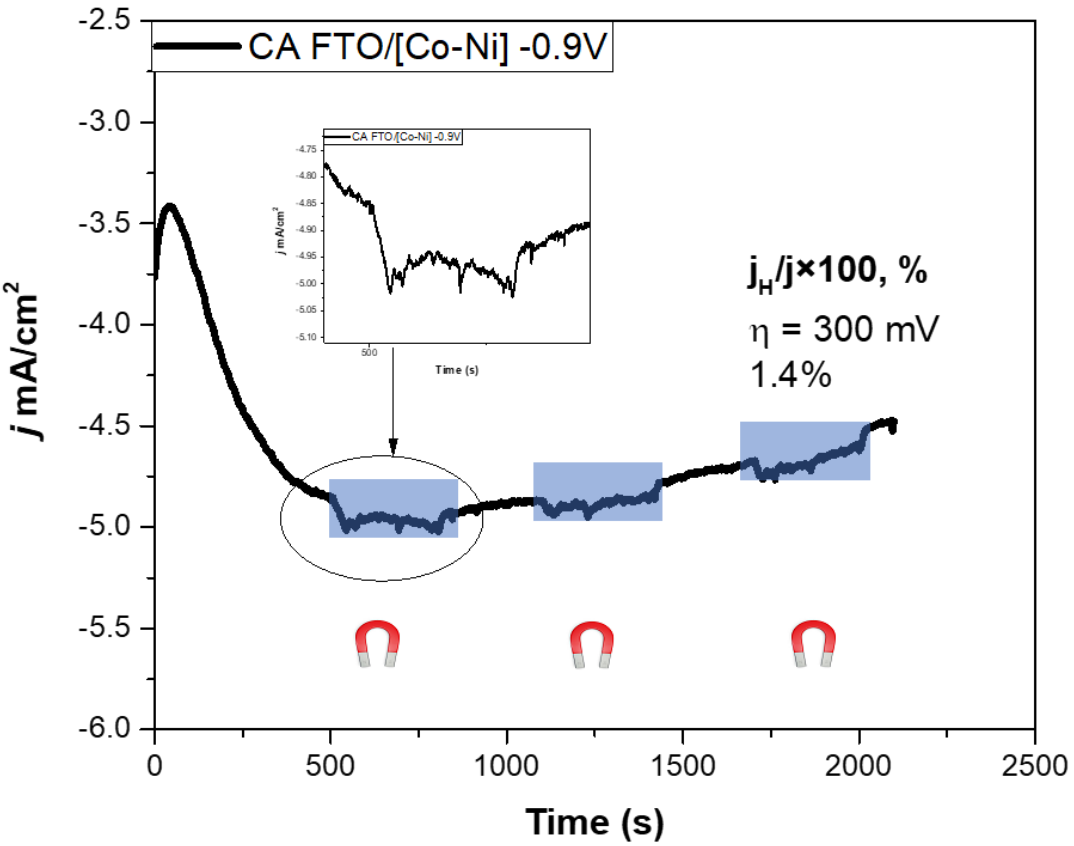

Fig 5. 2 CA profile of FTO/[Co-Ni] for HER reaction.

5.2. Solar Light Assisted HER Studies

5.2.1. Linear Sweep Voltammetry Studies Under Light Irradiation

As shown in Fig. 5.3, linear sweep voltammetry (LSV) curves were used to acquire distinct profiles, with the black trace representing the HER current density in the absence of solar light irradiation, and the red profile representing catalysis under solar light irradiation. The potential range for this investigation is between −0.2 and −1.6 volts against Ag/AgCl. The current under solar light irradiation is enhanced by 0.42 mA/cm2 at a 42 V overpotential (which was the selected zone for HER LSV's) [63]. 54 mV is recorded as the overpotential needed to achieve −1 mA/cm2 current density, and in the presence of solar light due to the early reduction of Ni from Ni^{2+} to Ni^{1+}, the overpotential was very slightly less than without solar light with a difference of decimals as could be seen in Fig 5.3. Under solar light irradiation, 6.2% enhancement was achieved in HER activity.

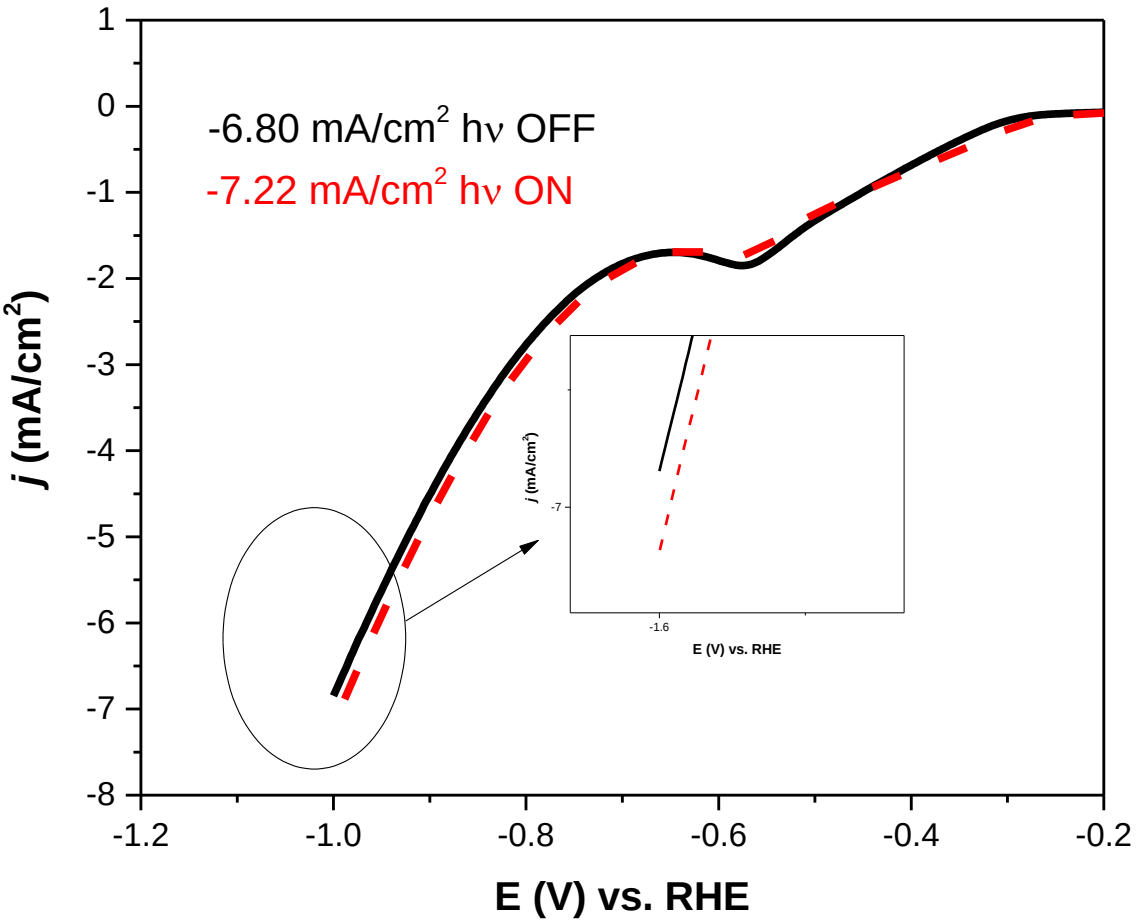

Fig 5. 3 LSV Profile of FTO/[Co-Ni] illustrating enhancement under solar light irradiation (Inset: Magnified the enhancement zone).

5.2.2. Chronoamperometric Studies

Unlike the magnetic field profile for HER, we were expecting enhancement for HER profile under solar light irradiation due to the semiconducting nature of PBA. Initially, a current density of −0.11 mA/cm^2 with −0.7 V, corresponds to an overpotential of 100 mV as could be seen in Fig 5.4. The current density was led to stabilize within 500 seconds which was later exposed to solar light irradiation. The solar light irradiation was subsequently switched off, and the CA pattern was allowed to continue, until the experimental endpoint at 2100 seconds. From the graph, it is evident that an enhancement is under light irradiation which is reversible. Furthermore, similar to FTO/[Co-Co] an enhancement under solar irradiation (38%) is obtained, which is reversible.

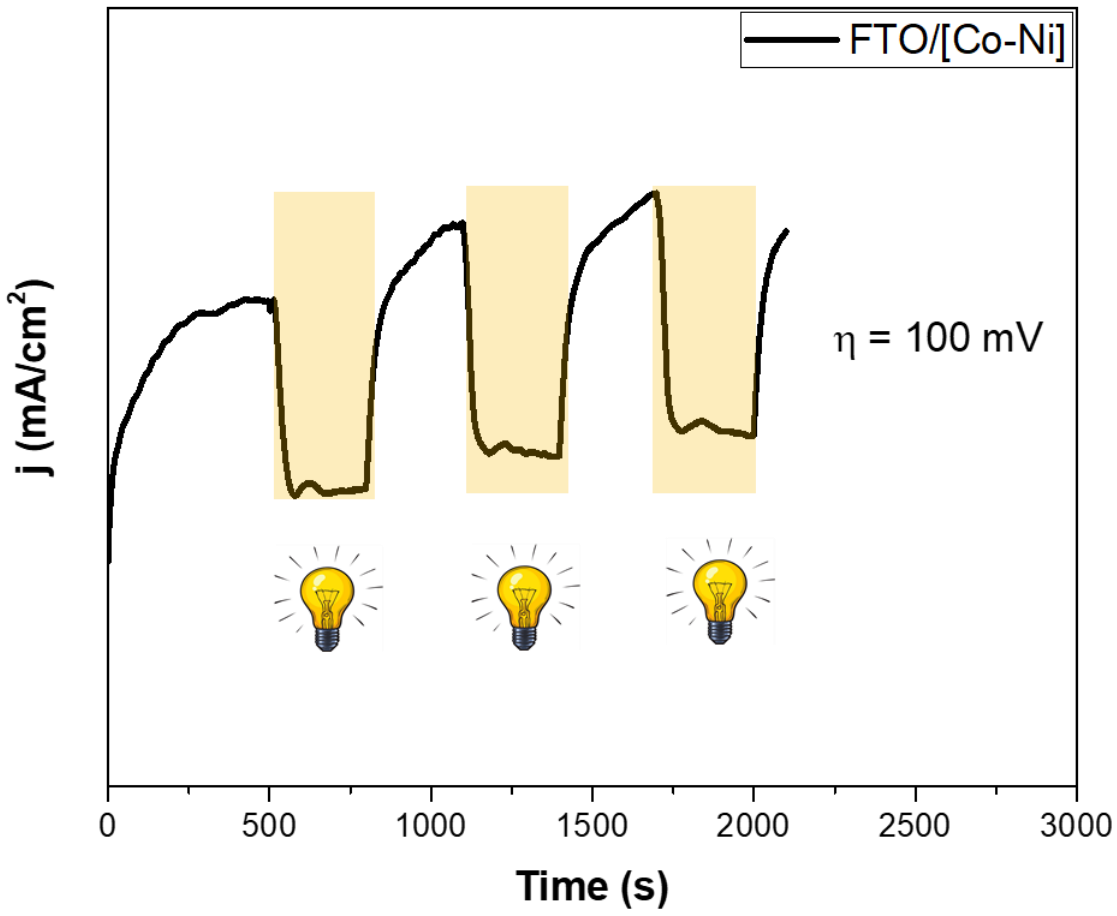

Fig 5. 4 CA Profile of FTO/[Co-Ni] under solar light irradiation.

Following this, once again the photocatalytic activity of the FTO/[Co-Ni] was investigated at various overpotentials as illustrated in Fig 5.5. Similarly, when the overpotential increases, % enhancement decreases revealing an inverse relationship between % enhancement and overpotential.

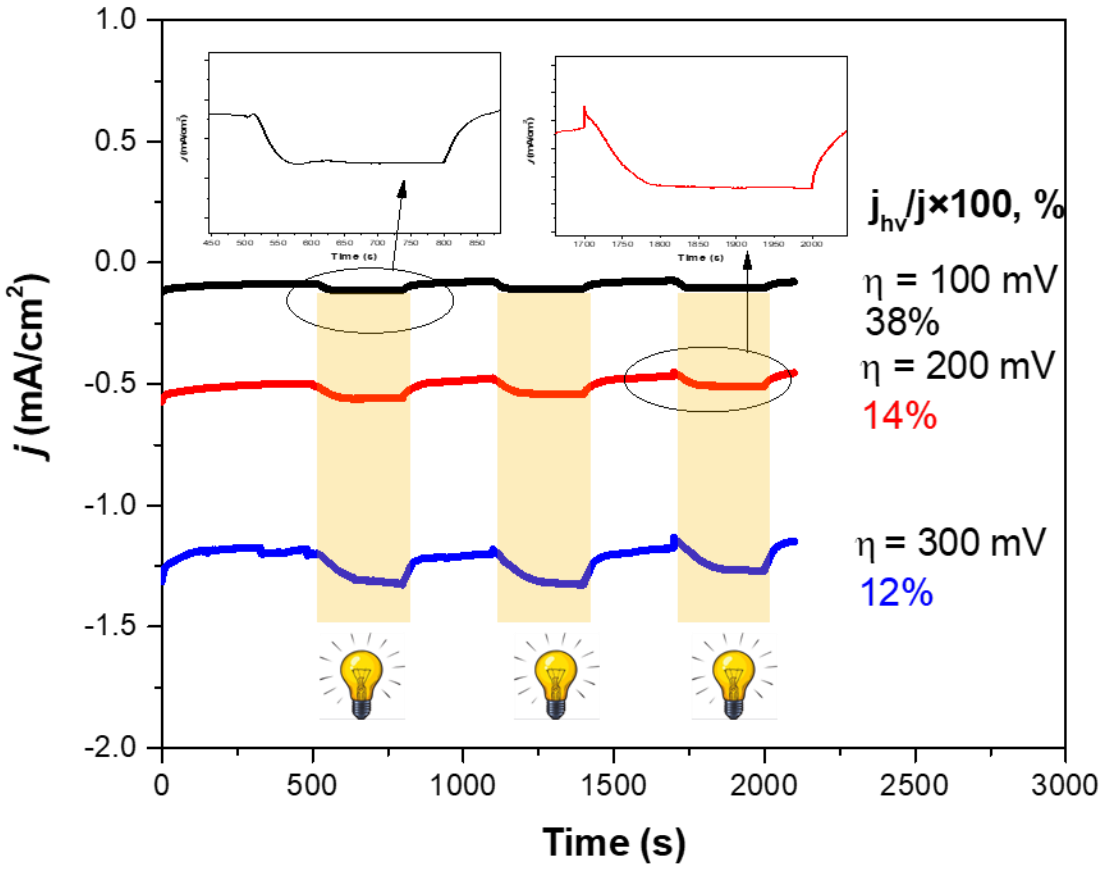

Fig 5. 5 CA profile of FTO/[Co-Ni] at various overpotentials.

Table 5.1 summarizes the FTO/[Co-Ni] HER activity depicting the negative trend in overpotential vs solar light irradiated catalytic performance.

Table 5. 1 Summary of solar irradiated HER studies.

η (mV/cm^2)	***j*$_s$ mA/cm^2**	***js*/*j*×100, %**
433 (LSV)	-0.42	6.7
300 (CA)	-1.28	12
200 (CA)	-0.61	14
100 (CA)	-0.24	38

Chapter 6: Electrochemical overall water splitting (OWS) under magnetic field and solar light irradiation

After studying carefully OER and HER with FTO/[Co-Co] and FTO/[Co-Ni] respectively, we concluded that the spin cross-over effect exclusively takes place in OER reactions. Since the gamry potentiostat is built in a design to prioritize the working electrode, thus allowing it to experience any level of overpotential compared to the counter electrode. Fig 6.1 summarizes the previous findings obtained in chapters 4 and 5.

In this chapter, we aimed to combine these findings to build a magnetic field and light-assisted overall water-splitting device, which has not been reported up to now.

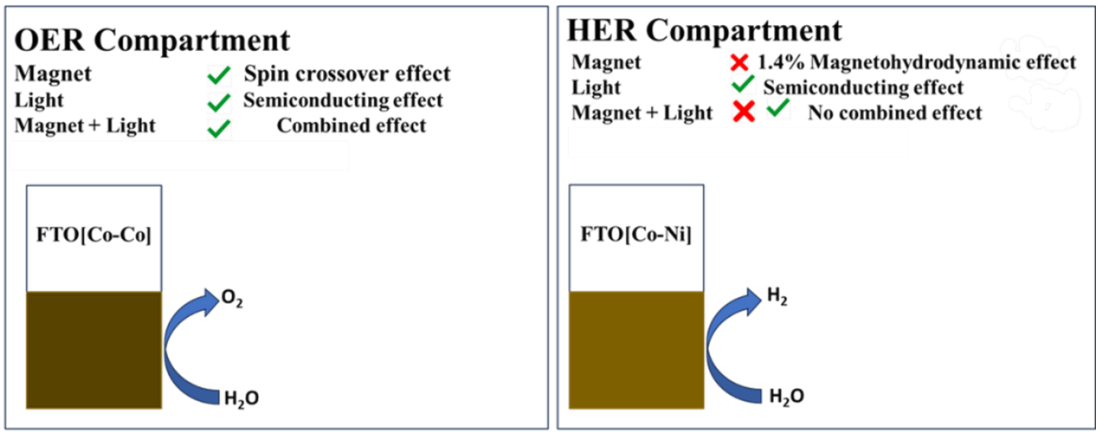

Fig 6. 1 Compilation and Overview of Current Research Findings.

6.1. Novel Experimental Configuration for Conducting Oxygen and Hydrogen Evolution Reaction in One Setup Studies

The design of the OWS was one of the most challenging parts of this thesis since two 3D-printed electrode holders were used in the OWS experiment rather than one electrode holder for OER and HER experiments. Keeping the electrode holders, firm and static under a magnetic field was difficult. It should also be noted that alligators are also sensitive to magnetic fields. In our optimization experiment, we found out magnetic field-assisted experiments reveal the highest activity when the electrodes are face to face (f2f) while for solar light-assisted studies, electrodes are placed side by side to ensure that both electrodes are exposed to solar light also illustrated in Fig 6.7.

Another additional concern was regarding the experimental setup. The issue was that if we remove the 3D-printed stage Fig 4.1, which was used to hold electrodes firmly under magnetic field studies, the experiment is not possible, since the electrodes held by alligators are prone to moving under magnetic field studies, and due to these reasons, we decided to use nonmagnetic conducting set up.

To address this issue, we tied platinum wires to the FTO electrode and stuffed it with extra platinum foil, to maximize the conductivity as shown in Fig.6.2.

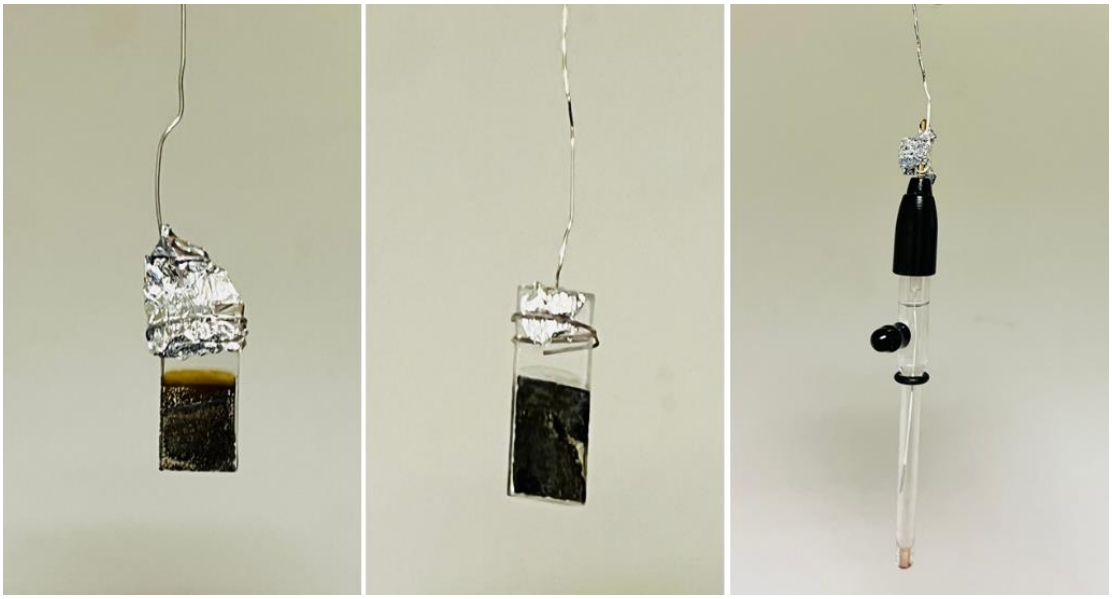

Fig 6. 2 Novel Experimental Setup for Conducting Overall Water-Splitting Experiments.

To perform the experiments, we came up with 2 designs, a two-electrode system, and a three-electrode system.

6.1.1. Two Electrode System

In a two-electrodes system, the reference electrode was removed, and combined the alligator of the reference electrode with the counter electrode. This Reference/Counter electrode was used to accommodate FTO/[Co-Ni] while on the working electrode we put FTO/[Co-Co] as shown in Fig 6.3. In 2 electrode system, gamry potentiostat adds the overpotential of both electrodes and combines them providing a very high overpotential. In our experimental setup, we used 2 V of potential which corresponds to an overpotential of 1013 mV with respect to the working electrode to get the following graph. To understand each electrode is taking how much

overpotential, we tried to run a chronopotentiometry experiment in which 1 mA/cm^2 current density was selected to be pursued. Hereby, we pursued 2 experiments.

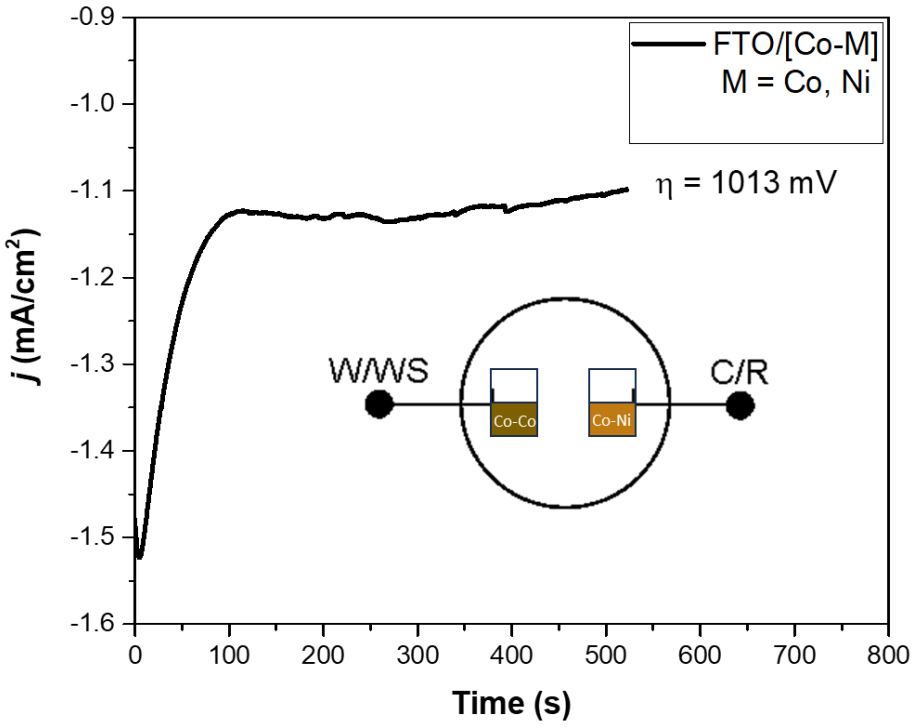

Fig 6. 3 CA profile obtained for OWS in a two-electrode system.

A) In the first experiment, FTO/[Co-Co] was accommodated as a working electrode, and FTO/[Co-Ni] as a counter electrode, with Ag/AgCl as a reference electrode. During the chronoamperometry experiment, a current density of 1 mA/cm^2 was pursued at 1.35 V, which corresponds to the potential between the working electrode and the reference electrode. By looking at the 2-electrode experiment, it should be a a potential difference of 0.54 V between the reference electrode and counter electrode Fig 6.4.

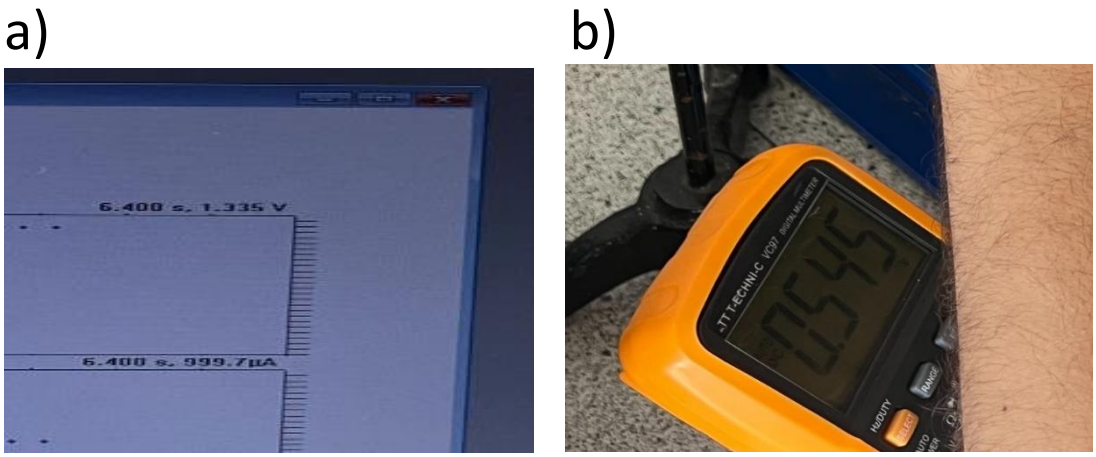

Fig 6. 4 a) Images of overpotential reading at working electrode displayed on the screen b) Image of overpotential displayed between counter and reference electrode with potentiometer.

B) To confirm this, the electrodes were swapped, i.e., the FTO/[Co-Co] was shifted to the counter electrode, however, the FTO/[Co-Ni] was shifted to the working electrode and a negative current density of −1 mA/cm^2 was given in chronopotentiometry study. This time the gamry was showing 0.6 V of potential difference, and to make sure, the potential difference between the reference and the counter was measured to be 1.298 V with a potentiometer. Hence confirmed, that the OER part was taking 1.3 V, however, HER is taking 0.6 V potential to achieve 1 mA/cm^2 of current density. The stats are displayed in Fig 6.5.

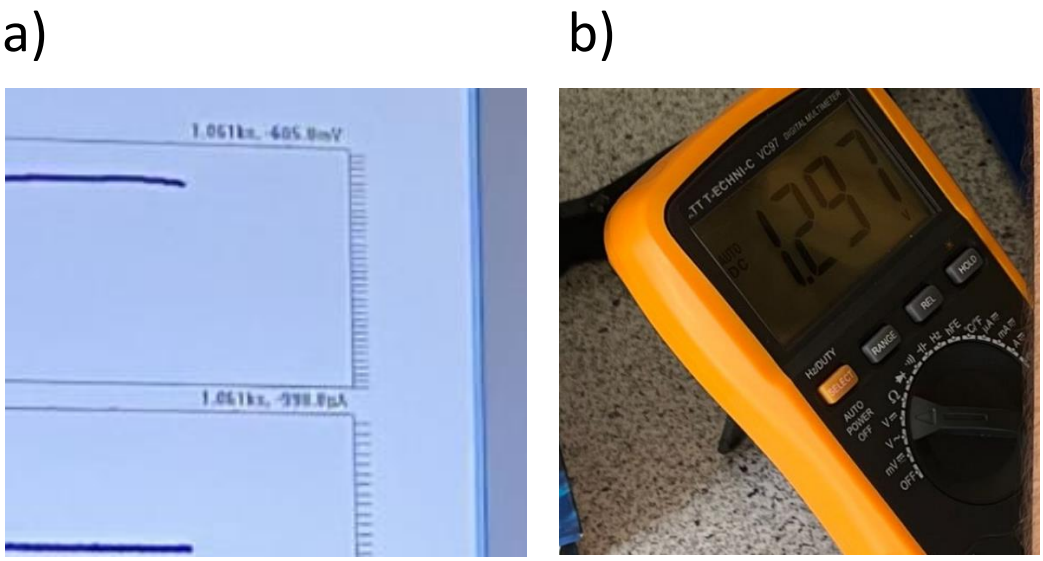

Fig 6. 5 a) Images of overpotential reading at working electrode displayed on the screen b) Image of overpotential displayed between counter and reference electrode with potentiometer.

6.1.2. Three-Electrode System

In three electrodes same protocols as used for separate OER and HER reactions were followed, however, the counter electrode C was replaced by FTO/[Co-Ni] instead of platinum wire while FTO/[Co-Co] was used in the working/working sense W/WS electrode. Fig.6.6 and 6.7 illustrates the three-electrode design utilized for the OWS.

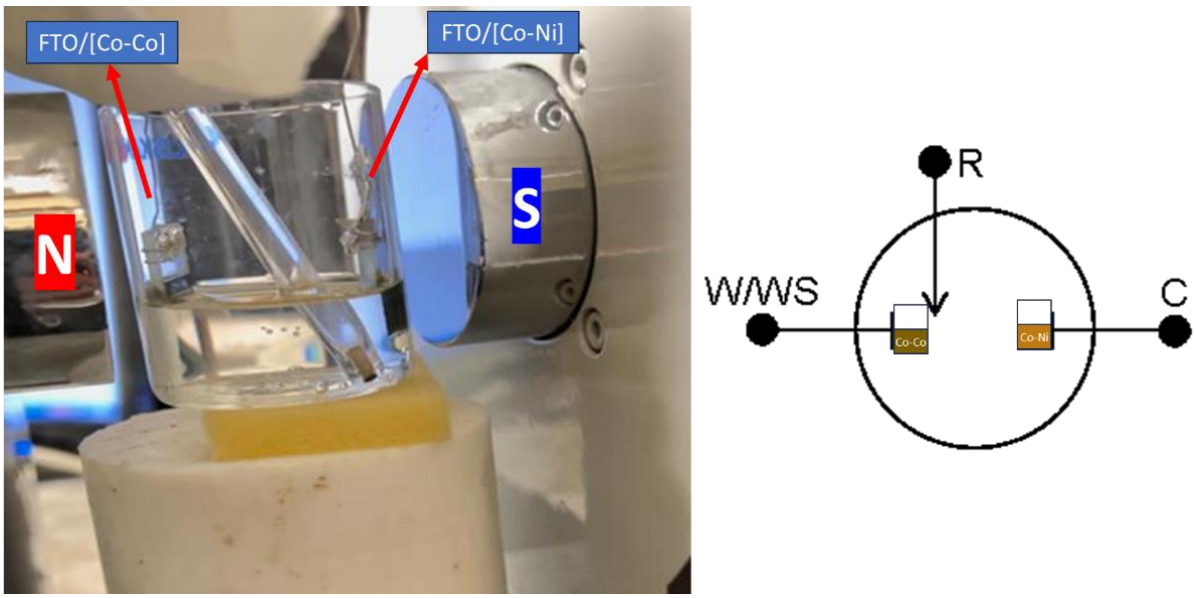

Fig 6. 6 Three-electrode system real image planted inside the magnetic field, with a schematic representation.

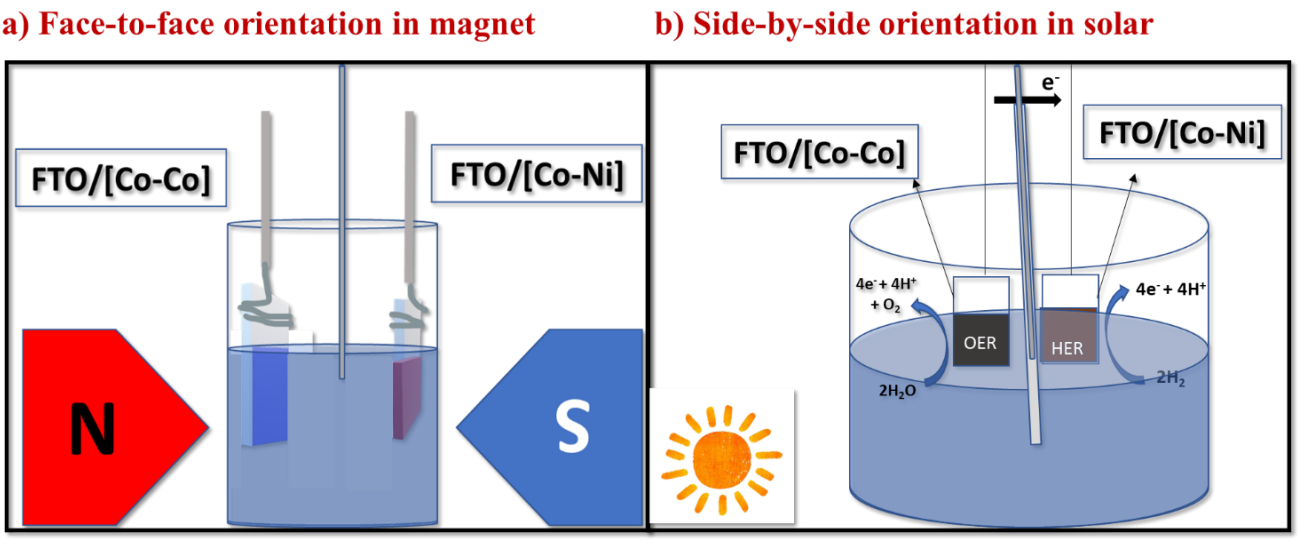

Fig 6. 7 Schematic diagram illustrating the three-electrode system utilized for OWS a) Face-to-face configuration for studies under magnetic field b) Side-by-side configuration for solar light irradiated studies.

6.2. Magnetic Field-Assisted Studies

6.2.1. CA Profile Of FTO/[Co-Co] And FTO/[Co-Ni] For OWS

Chronoamperometric measurements were made to evaluate the catalyst's stability, how a magnetic field affected it, and how well it performed as a catalyst. Over the course of 2100 seconds, a 949 mV of overpotential was applied. The chronoamperometric (CA) profile, shown in Fig 6.8, shows a steady current density for the first 500 seconds or so. After that, a 200 mT magnetic field was applied for 300 seconds. CA measurements continued throughout this sequential process of iterations until the experiment's predetermined endpoint at 2100 seconds. The catalyst's ongoing stability is indicated by the profile's consistency throughout. Under the 949 mV overpotential condition, the CA profile's peak current density was 5.1 mA/cm^2. The profile displays an impressive level of reproducibility in the findings, demonstrating an enhancement of 9.2%.

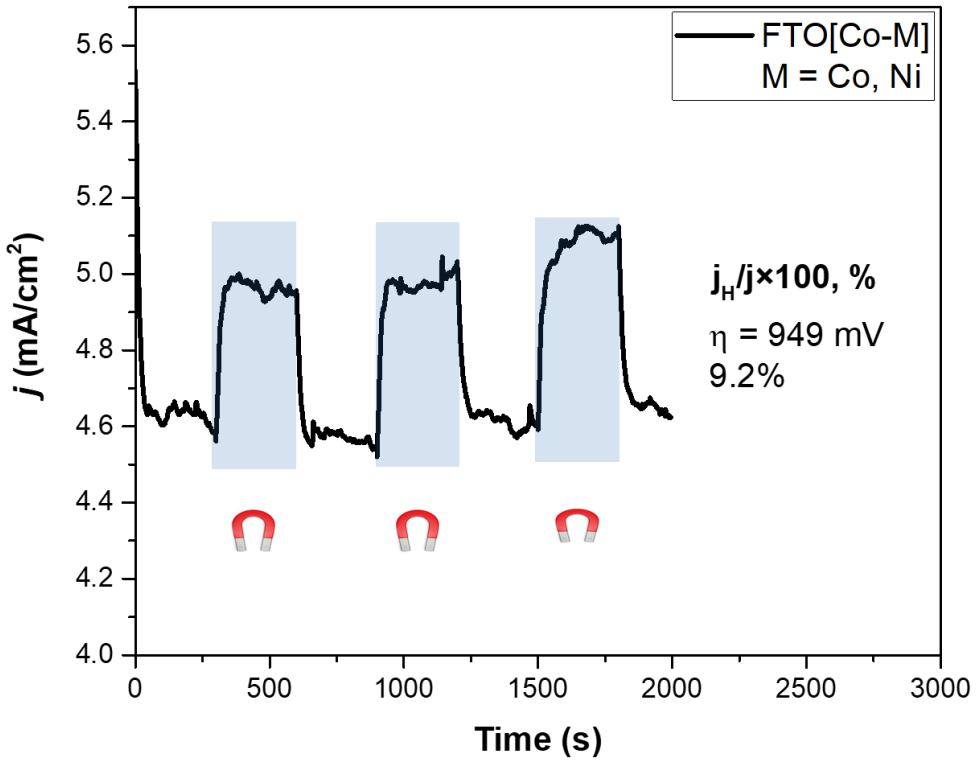

Fig 6. 8 CA profile obtained for FTO/[Co-Co] W/WS and FTO/[Co-Ni] C for OWS.

The chronoamperometric (CA) profile was thoroughly explored after the aforementioned investigations, this time with different overpotentials, while maintaining a constant magnetic field intensity of 200 mT. The relationship between overpotential values and the relative increase in current density was assessed. This showed a direct relationship where the overpotential values were systematically decreased, and a corresponding decrement in relative enhancement was observed as shown in Fig 6.9. The dependence of enhancement on overpotential suggests that complex mechanisms (spin crossover effect) that control the interaction between the magnetic field and electrocatalytic processes exist which is not similar to what we observed in solar light irradiated experiment.

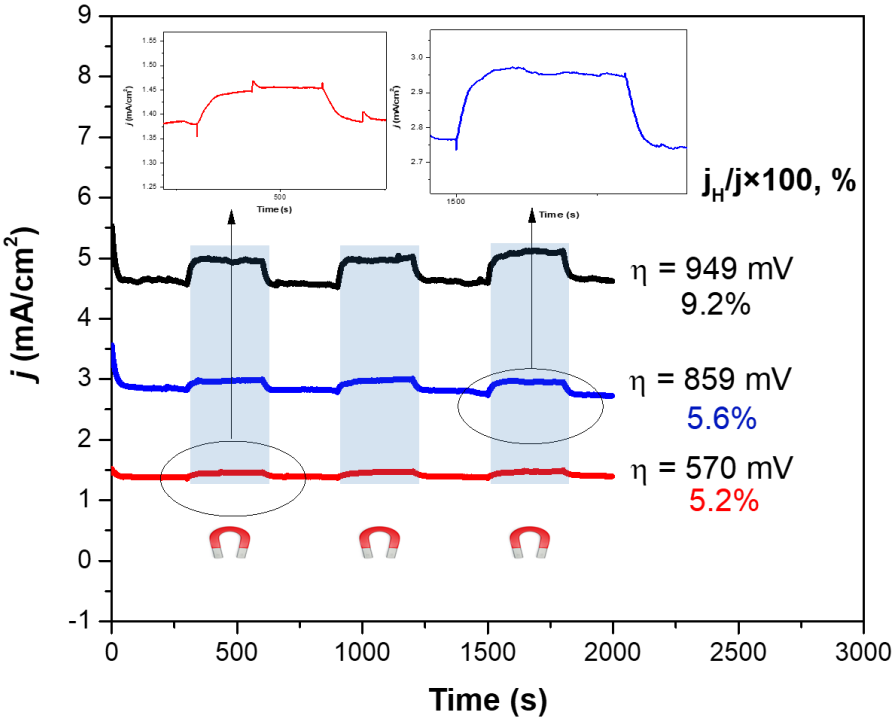

Fig 6. 9 CA profile obtained for FTO/[Co-Co] as W/WS and FTO/[Co-Ni] as C for OWS at various overpotentials (inset: Magnified picture of lower enhancements in the main graph).

Subsequent to this analysis, a comprehensive chronoamperometric (CA) measurement profile was achieved encompassing distinct magnetic field strengths. As visually represented in Fig 6.10. This experiment revealed a conspicuous and direct relationship between the magnitude of the applied magnetic field and the resulting current density. The observable pattern generated by these experiments highlights the potential for manipulating the magnetic field to enhance and regulate catalytic performance.

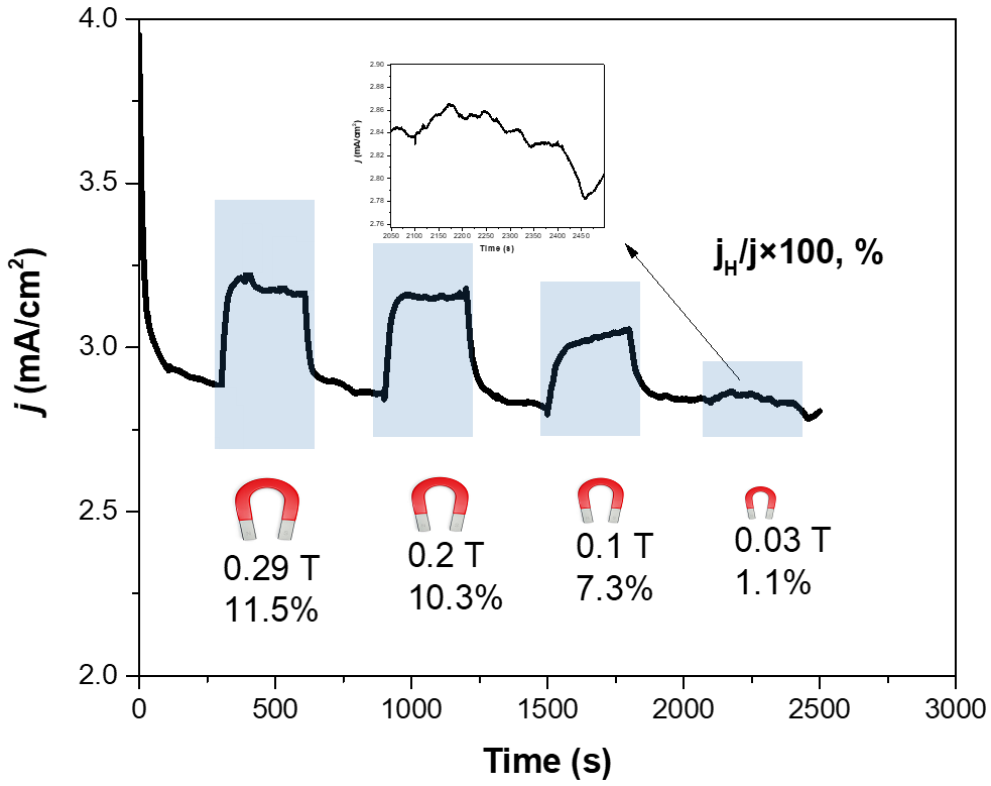

Fig 6. 10 CA profile obtained for FTO/[Co-Co] as W/WS and FTO/[Co-Ni] as C for OWS at various magnetic field strengths (inset: Magnified picture of lower enhancements in the main graph).

6.3. Solar Light Irradiated Studies

6.3.1. Chronoamperometric Studies

In order to investigate thoroughly the stability and the extended performance of solar light irradiation CA profile was obtained. This experiment was conducted using FTO/[Co-Co] as the working electrode for OER, and FTO/[Co-Ni] as the counter electrode for HER reaction. 859 mV of overpotential was applied as shown in Fig 6.11 to achieve 36 % of the enhancement mentioned in Fig 6.9. As shown by the figure, the CA profile, following a well-defined stabilization period of an initial 500 seconds, underwent a significant transformation upon exposure to solar light irradiation. The profile was recyclable and very stable in nature.

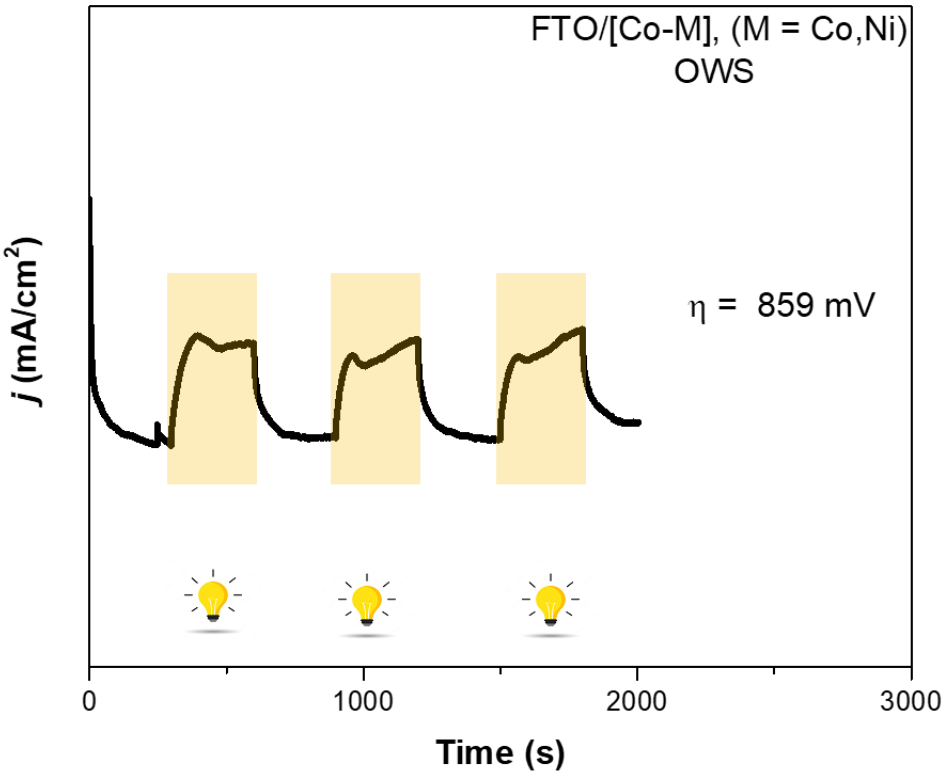

Fig 6. 11 LSV profile obtained for FTO/[Co-Co] as W/WS and FTO/[Co-Ni] as C for OWS.

Similar to our previous studies, (CA) experiments were conducted with a diverse range of overpotentials to investigate the effect of overpotential on the catalytic performance as shown in Fig 6.12. These experiments yielded a discernible pattern illustrating an inverse relationship between the overpotential and relative enhancement in the current density. Significantly, this effect was conspicuously opposite, when the catalyst was subjected to the influence of the magnetic field, underscoring the distinct nature of these two external stimuli and their differential impact on the electrochemical landscape.

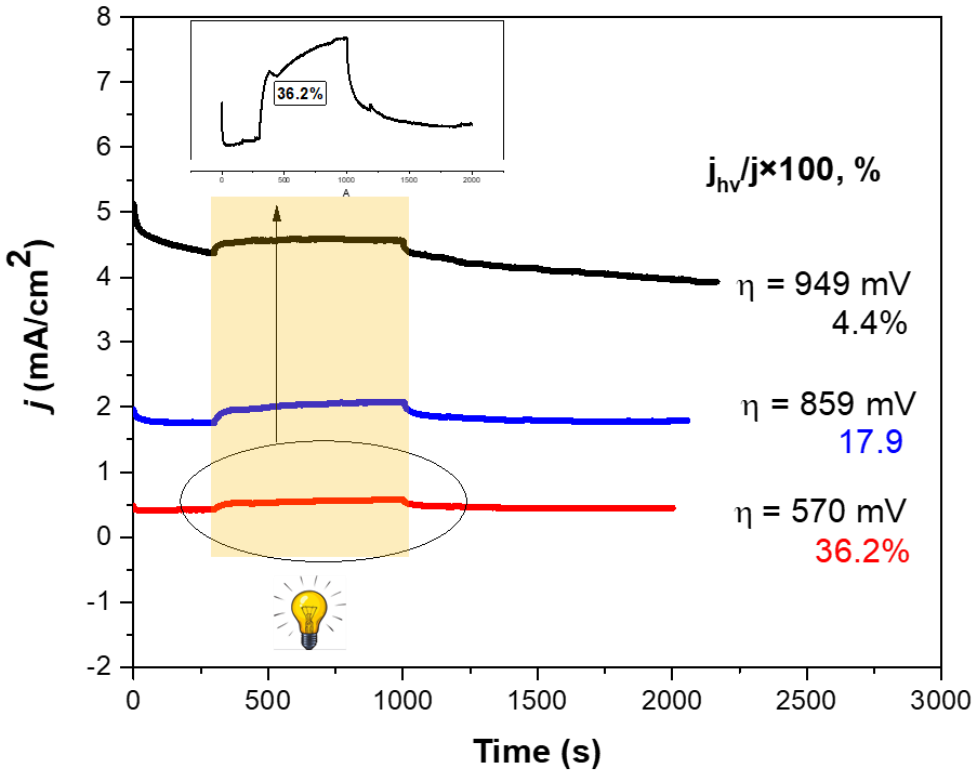

Fig 6. 12 CA profile obtained for FTO/[Co-Co] as W/WS and FTO/[Co-Ni] as C for OWS at various overpotential under solar light irradiation (inset: Magnified picture of lower enhancements in the main graph).

Table 6.1 summarizes the FTO/[Co-Ni] + FTO/[Co-Co] OWS activity depicting the direct relation between overpotential and % enhancement and negative trend in overpotential vs solar light irradiated catalytic performance.

Table 6. 1 Summary of solar irradiated and under magnetic field OWS studies.

Ƞ (mV/cm^2)	***j*$_m$ mA/cm^2**	***j*$_m$/*j*×100, %**	***j*$_s$ mA/cm^2**	***j*s/*j*×100, %**
949 (CA)	5.1	9.2	4.6	4.4
859 (CA)	3.0	5.6	2.0	17.9
570 (CA)	1.6	5.2	0.6	36.2

Chapter 7: Conclusion

In conclusion, the search for long-lasting and potent catalysts is of utmost importance in the effort to create a world with sustainable energy resources and clean environment. Prussian Blue Analogues (PBAs), a thoroughly researched class of substances, offer a flexible toolkit for designing powerful catalysts with exceptional functionality and reusability. This thesis explores novel findings resulting from the use of FTO/[Co-M], (M = Co-Ni), PBAs to hasten the overall water splitting (OWS) process while subjected to previously unresearched external stimuli.

The important work by Alsac et al. who carefully assessed the (OER) activity of various PBAs, served as the foundation for this investigation. They came up with the conclusion that Co-Co exhibits highest performance as an OER catalyst. The (HER) was then explored by Ahmad et al. who identified Co-Ni as the top performer in this context. By exploring the effect of magnetic fields on OER catalytic activity within the framework of PBA Co-Fe electrodeposited on the FTO surface, Ramadan et al. added to this discussion by expanding it to new levels. Their research revealed an increased magnetic field-catalyzed catalytic activity.

This study advances the conversation by gathering these investigations and exploring OWS in the context of external stimuli. This was accomplished by using FTO/[Co-Co] for OER reactions and FTO/[Co-Ni] as the catalyst for HER reactions. These electrodes were meticulously characterized using methods like SEM, EDAX, P-XRD, XPS, and ATR-FTIR after being carefully synthesized using a two-step electrodeposition procedure. The fascinating flower-like morphology of FTO/[Co], thread like growth of FTO/[Co-Co] and needle-like dimensions of FTO/[Co-Ni] respectively, showed uniform particle of 1-2 µm in size. Additionally, EDAX analysis confirmed an equimolar ratio of 3.21% Co and 3.34% Ni in FTO/[Co-Ni], confirming the presence of the respective elements in the expected ratios. P-XRD analyses confirmed the samples with their characteristic peaks.

The electrochemical studies performed on these catalysts revealed the following results.

Through LSV, the OER performance of FTO/[Co-Co] was revealed, and the enhancement peaks in response to external stimuli painted a clear picture. Solar light produced a stronger 7.1% enhancement while the magnetic field produced a 3.3% augmentation. Fascinatingly, CA profiles under the influence of varying overpotentials and magnetic field strengths revealed a direct correlation between the overpotential and the magnetic field strength. On the contrary,

the CA profile under solar light irradiation, in sharp contrast, showed a trend that was the opposite of the magnetic fields. The enhancement under magnetic fields was attributed to the spin crossover effect, while the enhancement under solar light irradiation was attributed to the semiconducting effect, according to the studies and insights from the body of existing literature.

Under the influence of solar light irradiation and magnetic fields, the HER efficacy of FTO/[Co-Ni] was examined. The LSV profile revealed enhancement only under solar light irradiation, the unanticipated boost was not brought about by magnetic fields. Similar to OER, the FTO/[Co-Ni] CA profiles showed the opposite trend in terms of the applied overpotential. Surprisingly, the magnetohydrodynamic effect resulted in a marginal 1.4% improvement in the HER CA profile.

Both a two- and a three-electrode setup was used for the investigation into overall water splitting. FTO/[Co-Co] served as the working electrode in the two-electrode configuration, and FTO/[Co-Ni] served as the counter electrode. For the system to produce a current density of 1 mA, a significant 1013 mV overpotential (2 V against Ag/AgCl) was required. Then, by analysing the various voltage contributions from each electrode, this phenomenon was explained. Notably, HER required 0.6 V while the OER process used about 1.3 V.

The working electrode in the three-electrode configuration, however, was FTO/[Co-Co], the counter electrode was FTO/[Co-Ni], and the reference electrode was Ag/AgCl. In this configuration, the profile clearly showed a significant improvement when both solar light and magnetic fields were present.

Based on PBA properties, we concluded that It's possible that the energy from photons could excite the electrons in the PBAs during solar light irradiation, resulting in improved charge transfer and reactivity. The PBAs' semiconducting characteristics might enable them to absorb and use solar energy for catalysis. On the other hand, the spin crossover effect could certainly play a role in the OER enhancement under magnetic fields, as it can influence the electronic and magnetic properties of the catalyst. Magnetic fields can alter the spin states of the metal ions in the PBAs, potentially affecting their reactivity and catalytic performance.

In conclusion, this study supports the idea that catalysis offers unexplored opportunities for improvement through subtle changes to reaction conditions that add an external stimulus dimension. This study should serve as a springboard for future research projects that explore cutting-edge technological techniques like Mott-Schottky analysis, Electrochemical Impedance Spectroscopy (EIS), and the use of in-situ characterization methods. These

analytical methods are intended to offer thorough understandings of the specific contributions of magnet-related phenomena, such as magnetohydrodynamic effects, spin polarization effects, or spin crossover effects, to the overall catalytic enhancement seen in this investigation. Furthermore, our prospective investigations should encompass an expanded spectrum of catalytic applications, subjecting the catalyst to diverse external stimuli. This multifaceted approach seeks to uncover novel techniques for manipulating catalysis and harnessing its potential in various domains. In essence, the future work outlined here underscores the need for a deeper understanding of the intricate mechanisms at play within catalytic systems, thereby advancing the frontiers of catalysis research. The current thesis advances the field by raising the bar and adding a new level of complexity to the effort of using PBAs in catalytic applications while building on earlier efforts.

References

[1] Lewis, N. S. (2016). Research opportunities to advance solar energy utilization. Science, 351(6271), aad1920.

[2] Mikulčić, H., Baleta, J., Zhang, Z., & Klemeš, J. J. (2023). Sustainable development of energy, water and environmental systems in the changing world. *Journal of Cleaner Production*, 135945.

[3] Chen, P. C., Chen, C., Yang, Y., Maulana, A. L., Jin, J., Feijoo, J., & Yang, P. (2023). Chemical and Structural Evolution of AgCu Catalysts in Electrochemical CO2 Reduction. *Journal of the American Chemical Society*, *145*(18), 10116-10125..

[4] Garin, F. (2004). Environmental catalysis. *Catalysis Today*, *89*(3), 255-268.

[5] Rasheed, T., & Anwar, M. T. (2023). Metal organic frameworks as self-sacrificing modalities for potential environmental catalysis and energy applications: Challenges and perspectives. *Coordination Chemistry Reviews*, *480*, 215011.

[6] Cook, T. R., Dogutan, D. K., Reece, S. Y., Surendranath, Y., Teets, T. S., & Nocera, D. G. (2010). Solar energy supply and storage for the legacy and nonlegacy worlds. *Chemical reviews*, *110*(11), 6474-6502.

[7] Chu, S., & Majumdar, A. (2012). Opportunities and challenges for a sustainable energy future. *nature*, *488*(7411), 294-303.

[8] Kerr, R. A., & Service, R. F. (2005). What can replace cheap oil--and when?. *Science*, *309*(5731), 101-101.

[9] Friend, C. M., & Xu, B. (2017). Heterogeneous catalysis: a central science for a sustainable future. *Accounts of chemical research*, *50*(3), 517-521.

[10] Roduner, E. (2014). Understanding catalysis. *Chemical Society Reviews*, *43*(24), 8226-8239.

[11] Takahashi, K., Ohyama, J., Nishimura, S., Fujima, J., Takahashi, L., Uno, T., & Taniike, T. (2023). Catalysts informatics: paradigm shift towards data-driven catalyst design. *Chemical Communications*, *59*(16), 2222-2238.

[12] Vogiatzis, K. D., Polynski, M. V., Kirkland, J. K., Townsend, J., Hashemi, A., Liu, C., & Pidko, E. A. (2018). Computational approach to molecular catalysis by 3d transition metals: challenges and opportunities. *Chemical reviews*, *119*(4), 2453-2523.

[13] Venkatesh, L., Logeshkumar, R., Jayaprakash, G., & Dinesh, N. (2017). Control and reduction of emissions using catalytic converter. *International Research Journal of Engineering and Technology (IRJET)*, *4*(11), 788-794.

[14] Gómez-López, P., Puente-Santiago, A., Castro-Beltrán, A., do Nascimento, L. A. S., Balu, A. M., Luque, R., & Alvarado-Beltrán, C. G. (2020). Nanomaterials and catalysis for green chemistry. *Current Opinion in Green and Sustainable Chemistry*, *24*, 48-55.

[15] Chen, P. C., Chen, C., Yang, Y., Maulana, A. L., Jin, J., Feijoo, J., & Yang, P. (2023). Chemical and Structural Evolution of AgCu Catalysts in Electrochemical CO2 Reduction. *Journal of the American Chemical Society*, *145*(18), 10116-10125.

[16] Hayler, J. D., Leahy, D. K., & Simmons, E. M. (2018). A pharmaceutical industry perspective on sustainable metal catalysis. *Organometallics*, *38*(1), 36-46.

[17] Ahmad, W., Khan, A., Ali, N., Khan, S., Uddin, S., Malik, S., ... & Bilal, M. (2021). Photocatalytic degradation of crystal violet dye under sunlight by chitosan-encapsulated ternary metal selenide microspheres. *Environmental Science and Pollution Research*, *28*, 8074-8087.

[18] Nocera, D. G. (2017). Solar fuels and solar chemicals industry. *Accounts of chemical research*, *50*(3), 616-619.

[19] Sun, X., Jiang, S., Huang, H., Li, H., Jia, B., & Ma, T. (2022). Solar energy catalysis. *Angewandte Chemie International Edition*, *61*(29), e202204880..

[20] Dash, S. K., Chakraborty, S., Roccotelli, M., & Sahu, U. K. (2022). Hydrogen fuel for future mobility: Challenges and future aspects. *Sustainability*, *14*(14), 8285.

[21] Hassan, Q., Abdulateef, A. M., Hafedh, S. A., Al-samari, A., Abdulateef, J., Sameen, A. Z., ... & Jaszczur, M. (2023). Renewable energy-to-green hydrogen: A review of main resources routes, processes and evaluation. *International Journal of Hydrogen Energy*.

[22] Rejeb, O., Alirahmi, S. M., Assareh, E., Assad, M. E. H., Jemni, A., Bettayeb, M., & Ghenai, C. (2022). Innovative integrated solar powered polygeneration system for green Hydrogen, Oxygen, electricity and heat production. *Energy Conversion and Management*, *269*, 116073.

[23] Faye, O., Szpunar, J., & Eduok, U. (2022). A critical review on the current technologies for the generation, storage, and transportation of hydrogen. *International Journal of Hydrogen Energy*, *47*(29), 13771-13802.

[24] Shi, Y., & Zhang, B. (2016). Recent advances in transition metal phosphide nanomaterials: synthesis and applications in hydrogen evolution reaction. *Chemical Society Reviews*, *45*(6), 1529-1541.

[25] Oni, A. O., Anaya, K., Giwa, T., Di Lullo, G., & Kumar, A. (2022). Comparative assessment of blue hydrogen from steam methane reforming, autothermal reforming, and natural gas decomposition technologies for natural gas-producing regions. *Energy Conversion and Management*, *254*, 115245.

[26] Matamba, T., Iglauer, S., & Keshavarz, A. (2022). A progress insight of the formation of hydrogen rich syngas from coal gasification. *Journal of the Energy Institute*.

[27] Jiao, Y., Zheng, Y., Jaroniec, M., & Qiao, S. Z. (2015). Design of electrocatalysts for oxygen-and hydrogen-involving energy conversion reactions. *Chemical Society Reviews*, *44*(8), 2060-2086.

[28] Murthy, A. P., Madhavan, J., & Murugan, K. (2018). Recent advances in hydrogen evolution reaction catalysts on carbon/carbon-based supports in acid media. *Journal of Power Sources*, *398*, 9-26.

[29] Yan, Y., Xia, B. Y., Zhao, B., & Wang, X. (2016). A review on noble-metal-free bifunctional heterogeneous catalysts for overall electrochemical water splitting. *Journal of Materials Chemistry A*, *4*(45), 17587-17603.

[30] Zhou, L., Lu, S. Y., & Guo, S. (2021). Recent progress on precious metal single atom materials for water splitting catalysis. *SusMat*, *1*(2), 194-210.

[31] Bodhankar, P. M., Sarawade, P. B., Kumar, P., Vinu, A., Kulkarni, A. P., Lokhande, C. D., & Dhawale, D. S. (2022). Nanostructured metal phosphide based catalysts for electrochemical water splitting: a review. *Small*, *18*(21), 2107572.

[32] Dong, G., Yan, L., & Bi, Y. (2023). Advanced oxygen evolution reaction catalysts for solar-driven photoelectrochemical water splitting. *Journal of Materials Chemistry A*, *11*(8), 3888-3903.

[33] Yan, Y., Xia, B. Y., Zhao, B., & Wang, X. (2016). A review on noble-metal-free bifunctional heterogeneous catalysts for overall electrochemical water splitting. *Journal of Materials Chemistry A*, *4*(45), 17587-17603.

[34] Al-Naggar, A. H., Shinde, N. M., Kim, J. S., & Mane, R. S. (2023). Water splitting performance of metal and non-metal-doped transition metal oxide electrocatalysts. *Coordination Chemistry Reviews*, *474*, 214864.

[35] Rodríguez-Jiménez, S., Song, H., Lam, E., Wright, D., Pannwitz, A., Bonke, S. A., ... & Reisner, E. (2022). Self-assembled liposomes enhance electron transfer for efficient photocatalytic CO2 reduction. *Journal of the American Chemical Society*, *144*(21), 9399-9412.

[36] Cao, L. M., Lu, D., Zhong, D. C., & Lu, T. B. (2020). Prussian blue analogues and their derived nanomaterials for electrocatalytic water splitting. *Coordination Chemistry Reviews*, *407*, 213156.

[37] Zhou, Y., Guan, X., Wu, R., Dang, Y., Yu, S., Zhou, Y., & Tang, J. (2023). An electrochemical biosensor based on CuFe PBA/MoS2 nanocomposites for stable and sensitive detection of hydrogen peroxide and carcinoembryonic antigen. *Journal of Electroanalytical Chemistry*, 117592.

[38] Elgrishi, N., Rountree, K. J., McCarthy, B. D., Rountree, E. S., Eisenhart, T. T., & Dempsey, J. L. (2018). A practical beginner's guide to cyclic voltammetry. *Journal of chemical education*, *95*(2), 197-206.

[39] Yu, M. Q., Li, Y. H., Yang, S., Liu, P. F., Pan, L. F., Zhang, L., & Yang, H. G. (2015). Mn 3 O 4 nano-octahedrons on Ni foam as an efficient three-dimensional oxygen evolution electrocatalyst. *Journal of Materials Chemistry A*, *3*(27), 14101-14104.

[40] Mabayoje, O., Shoola, A., Wygant, B. R., & Mullins, C. B. (2016). The role of anions in metal chalcogenide oxygen evolution catalysis: electrodeposited thin films of nickel sulfide as "pre-catalysts". *ACS Energy Letters*, *1*(1), 195-201.

[41] Cheng, X., Fabbri, E., Nachtegaal, M., Castelli, I. E., El Kazzi, M., Haumont, R., ... & Schmidt, T. J. (2015). Oxygen evolution reaction on La1–x Sr x CoO3 perovskites: a combined experimental and theoretical study of their structural, electronic, and electrochemical properties. *Chemistry of Materials*, *27*(22), 7662-7672., pp. 7662-7672, 2015.

[42] Chung, D. Y., Lopes, P. P., Farinazzo Bergamo Dias Martins, P., He, H., Kawaguchi, T., Zapol, P., ... & Markovic, N. M. (2020). Dynamic stability of active sites in hydr (oxy) oxides for the oxygen evolution reaction. *Nature Energy*, *5*(3), 222-230.

[43] Wang, J., Kim, S. J., Liu, J., Gao, Y., Choi, S., Han, J., ... & Lim, J. (2021). Redirecting dynamic surface restructuring of a layered transition metal oxide catalyst for superior water oxidation. *Nature Catalysis*, *4*(3), 212-222.

[44] Shi, Y., Zhang, D., Miao, H., Zhang, W., Wu, X., Wang, Z., ... & Wang, L. (2021). A simple, rapid and scalable synthesis approach for ultra-small size transition metal selenides with efficient water oxidation performance. *Journal of Materials Chemistry A*, *9*(43), 24261-24267.

[45] Hu, H., Wang, Z., Cao, L., Zeng, L., Zhang, C., Lin, W., & Wang, C. (2021). Metal–organic frameworks embedded in a liposome facilitate overall photocatalytic water splitting. *Nature Chemistry*, *13*(4), 358-366.

[46] Zhao, J. W., Shi, Z. X., Li, C. F., Ren, Q., & Li, G. R. (2021). Regulation of perovskite surface stability on the electrocatalysis of oxygen evolution reaction. *ACS Materials Letters*, *3*(6), 721-737.

[47] Swathi, S., Yuvakkumar, R., Ravi, G., Shanthini, M., Al-Sehemi, A. G., Thambidurai, M., ... & Velauthapillai, D. (2022). Effect of sodium dodecyl sulfate surfactant concentrations on the novel strontium copper oxide nanostructures for enriching hydrogen evolution reaction electrochemical activity in alkaline solution. *Journal of Alloys and Compounds*, *928*, 167001.

[48] Xie, Q., Zhou, D., Li, P., Cai, Z., Xie, T., Gao, T., ... & Sun, X. (2019). Enhancing oxygen evolution reaction by cationic surfactants. *Nano Research*, *12*, 2302-2306.

[49] Hanusa, T. P. (2011). Cyanide complexes of the transition metals. *Encyclopedia of Inorganic and Bioinorganic Chemistry*.

[50] Griffith, W. P. (1962). Cyanide complexes of the transition metals. Quarterly Reviews, Chemical Society, 16(2), 188-207.

[51] Bonaccorsi, R., Petrongolo, C., Scrocco, E., & Tomasi, J. (1968). SCF Minimal Basis Set Calculations and Exclusive Orbitals for CN−, HCN, N3−, HN3, NCO−, and HNCO. *The Journal of Chemical Physics*, *48*(4), 1500-1508.

[52] Dunbar, K. R., & Heintz, R. A. (1997). Chemistry of transition metal cyanide compounds: Modern perspectives. *Progress in inorganic chemistry*, *45*, 283-392.

[53] Itaya, K., Uchida, I., & Neff, V. D. (1986). Electrochemistry of polynuclear transition metal cyanides: Prussian blue and its analogues. *Accounts of Chemical Research*, *19*(6), 162-168.

[54] Nakamoto, K. (2009). *Infrared and Raman spectra of inorganic and coordination compounds, part B: applications in coordination, organometallic, and bioinorganic chemistry*. John Wiley & Sons.

[55] Hong, S. F., & Chen, L. C. (2012). Nano-Prussian blue analogue/PEDOT: PSS composites for electrochromic windows. *Solar energy materials and solar cells*, *104*, 64-74.

[56] Zhou, Y., Guan, X., Wu, R., Dang, Y., Yu, S., Zhou, Y., & Tang, J. (2023). An electrochemical biosensor based on CuFe PBA/MoS2 nanocomposites for stable and sensitive detection of hydrogen peroxide and carcinoembryonic antigen. *Journal of Electroanalytical Chemistry*, 117592.

[57] Singh, B., & Indra, A. (2020). Prussian blue-and Prussian blue analogue-derived materials: progress and prospects for electrochemical energy conversion. *Materials Today Energy*, *16*, 100404.

[58] Alsaç, E. P., Ülker, E., Nune, S. V. K., Dede, Y., & Karadas, F. (2018). Tuning the electronic properties of prussian blue analogues for efficient water oxidation electrocatalysis: experimental and computational studies. *Chemistry–A European Journal*, *24*(19), 4856-4863.

[59] Ahmad, A. A., Ghobadi, T. G. U., Ozbay, E., & Karadas, F. (2022). 2D Network overtakes 3D for photocatalytic hydrogen evolution. *Chemical Communications*, *58*(67), 9341-9344.

[60] Goberna-Ferron, S., Hernandez, W. Y., Rodriguez-Garcia, B., & Galán-Mascarós, J. R. (2014). Light-driven water oxidation with metal hexacyanometallate heterogeneous catalysts. *ACS catalysis*, *4*(6), 1637-1641.

[61] Gono, P., & Pasquarello, A. (2020). Oxygen evolution reaction: Bifunctional mechanism breaking the linear scaling relationship. *The Journal of chemical physics*, *152*(10).

[62] Li, J., Ma, J., Ma, Z., Zhao, E., Du, K., Guo, J., & Ling, T. (2021). Spin effect on oxygen electrocatalysis. *Advanced Energy and Sustainability Research*, *2*(8), 2100034.

[63] Hegner, F. S., Galán-Mascarós, J. R., & López, N. (2022). Lowering the Water Oxidation Overpotential by Spin-Crossover in Cobalt Hexacyanoferrate. *The Journal of Physical Chemistry Letters*, *13*(18), 4104-4110.

[64] Dempsey, J. L., Brunschwig, B. S., Winkler, J. R., & Gray, H. B. (2009). Hydrogen evolution catalyzed by cobaloximes. *Accounts of chemical research*, *42*(12), 1995-2004.

[65] Gómez-García, C. J. (2015). Magnetochemistry: An Old Discipline with New Opportunities. *Magnetochemistry*, *1*(1), 1.

[66] Zhang, Y., Guo, P., Niu, S., Wu, J., Wang, W., Song, B., ... & Xu, P. (2022). Magnetic field enhanced electrocatalytic oxygen evolution of NiFe-LDH/Co3O4 p-n heterojunction supported on nickel foam. *Small methods*, *6*(6), 2200084.

[67] Ragsdale, S. R., Lee, J., Gao, X., & White, H. S. (1996). Magnetic field effects in electrochemistry. Voltammetric reduction of acetophenone at microdisk electrodes. *The Journal of Physical Chemistry*, *100*(14), 5913-5922.

[68] Luo, S., Elouarzaki, K., & Xu, Z. J. (2022). Electrochemistry in magnetic fields. *Angewandte Chemie International Edition*, *61*(27), e202203564.

[69] Cai, L., Huo, J., Zou, P., Li, G., Liu, J., Xu, W., ... & Wang, J. Q. (2022). Key role of Lorentz excitation in the electromagnetic-enhanced hydrogen evolution reaction. *ACS Applied Materials & Interfaces*, *14*(13), 15243-15249.

[70] Elias, L., & Chitharanjan Hegde, A. (2017). Effect of magnetic field on HER of water electrolysis on Ni–W alloy. *Electrocatalysis*, *8*, 375-382.

[71] Monzon, L. M., Rode, K., Venkatesan, M., & Coey, J. M. D. (2012). Electrosynthesis of iron, cobalt, and zinc microcrystals and magnetic enhancement of the oxygen reduction reaction. *Chemistry of Materials*, *24*(20), 3878-3885.

[72] Garcés-Pineda, F. A., Blasco-Ahicart, M., Nieto-Castro, D., López, N., & Galán-Mascarós, J. R. (2019). Direct magnetic enhancement of electrocatalytic water oxidation in alkaline media. *Nature Energy*, *4*(6), 519-525.

[73] Zhang, Y., Guo, P., Li, S., Sun, J., Wang, W., Song, B., ... & Xu, P. (2022). Magnetic field assisted electrocatalytic oxygen evolution reaction of nickel-based materials. *Journal of Materials Chemistry A*, *10*(4), 1760-1767.

[74] Gono, P., & Pasquarello, A. (2020). Oxygen evolution reaction: Bifunctional mechanism breaking the linear scaling relationship. *The Journal of chemical physics*, *152*(10).

[75] Gabrielli, C., Huet, F., & Nogueira, R. P. (2005). Fluctuations of concentration overpotential generated at gas-evolving electrodes. *Electrochimica Acta*, *50*(18), 3726-3736.

[76] Newman, J. (1969). Ohmic potential measured by interrupter techniques.

[77] Iida, T., Matsushima, H., & Fukunaka, Y. (2007). Water electrolysis under a magnetic field. *Journal of the electrochemical society*, *154*(8), E112.

[78] Ren, X., Wu, T., Sun, Y., Li, Y., Xian, G., Liu, X., ... & Xu, Z. J. (2021). Spin-polarized oxygen evolution reaction under magnetic field. *Nature Communications*, *12*(1), 2608.

[79] Mtangi, W., Kiran, V., Fontanesi, C., & Naaman, R. (2015). Role of the electron spin polarization in water splitting. *The journal of physical chemistry letters*, *6*(24), 4916-4922.

[80] Gatard, V., Deseure, J., & Chatenet, M. (2020). Use of magnetic fields in electrochemistry: a selected review. *Current Opinion in Electrochemistry*, *23*, 96-105.

[81] Li, J., Ma, J., Ma, Z., Zhao, E., Du, K., Guo, J., & Ling, T. (2021). Spin effect on oxygen electrocatalysis. *Advanced Energy and Sustainability Research*, *2*(8), 2100034.

[82] Ghosh, S., Bloom, B. P., Lu, Y., Lamont, D., & Waldeck, D. H. (2020). Increasing the efficiency of water splitting through spin polarization using cobalt oxide thin film catalysts. *The Journal of Physical Chemistry C*, *124*(41), 22610-22618.

[83] Zhang, L., Jackson, C. B., Mou, H., Ojha, A., Peng, H., Quinlan, B. D., ... & Choe, H. (2020). SARS-CoV-2 spike-protein D614G mutation increases virion spike density and infectivity. *Nature communications*, *11*(1), 6013.

[84] Garcés-Pineda, F. A., Blasco-Ahicart, M., Nieto-Castro, D., López, N., & Galán-Mascarós, J. R. (2019). Direct magnetic enhancement of electrocatalytic water oxidation in alkaline media. *Nature Energy*, *4*(6), 519-525.

[85] Chalil Oglou, R., Ulusoy Ghobadi, T. G., Hegner, F. S., Galán-Mascarós, J. R., López, N., Ozbay, E., & Karadas, F. Manipulating Intermetallic Charge Transfer for

Switchable External Stimulus-Enhanced Water Oxidation Electrocatalysis. *Angewandte Chemie*, e202308647.

[86] Qiao, X., Kang, H., Li, Y., Cui, K., Jia, X., Wu, X., & Qin, W. (2022). Novel FeNi-Based Nanowires Network Catalyst Involving Hydrophilic Channel for Oxygen Evolution Reaction. *Small*, *18*(10), 2106378.

[87] Luo, W., Wang, Y., Luo, L., Gong, S., Wei, M., Li, Y., ... & Li, Z. (2022). Single-atom and bimetallic nanoalloy supported on nanotubes as a bifunctional electrocatalyst for ultrahigh-current-density overall water splitting. *ACS Catalysis*, *12*(2), 1167-1179.

[88] Zhang, B., Wu, Z., Shao, W., Gao, Y., Wang, W., Ma, T., ... & Zhao, C. (2022). Interfacial Atom-Substitution Engineered Transition-Metal Hydroxide Nanofibers with High-Valence Fe for Efficient Electrochemical Water Oxidation. *Angewandte Chemie*, *134*(13), e202115331.

[89] Liu, Z., Li, X., Yang, M., Zhang, S., Wang, L., Niu, C., & Lv, Y. (2023). Facile Hydrothermal Synthesis of Prussian Blue Films Using Hydrobromic Acid and their Electrochromic Properties. *International Journal of Nanoscience*, *22*(01), 2350007.

[90] Oglou, R. C., Ghobadi, T. G. U., Ozbay, E., & Karadas, F. (2021). Electrodeposited cobalt hexacyanoferrate electrode as a non-enzymatic glucose sensor under neutral conditions. *Analytica Chimica Acta*, *1188*, 339188.

[91] Ulusoy Ghobadi, T. G., Ghobadi, A., Buyuktemiz, M., Yildiz, E. A., Berna Yildiz, D., Yaglioglu, H. G., ... & Karadas, F. (2020). A Robust, Precious-Metal-Free Dye-Sensitized Photoanode for Water Oxidation: A Nanosecond-Long Excited-State Lifetime through a Prussian Blue Analogue. *Angewandte Chemie*, *132*(10), 4111-4119.

[92] Ghobadi, T. G. U., Ghobadi, A., Demirtas, M., Buyuktemiz, M., Ozvural, K. N., Yildiz, E. A., ... & Karadas, F. (2021). Building an iron chromophore incorporating prussian blue analogue for photoelectrochemical water oxidation. *Chemistry–A European Journal*, *27*(35), 8966-8976.

[93] Gundogdu, G., Ghobadi, T. G. U., Akbari, S. S., Ozbay, E., & Karadas, F. (2021). Photocatalytic water oxidation with a Prussian blue modified brown TiO 2. *Chemical Communications*, *57*(4), 508-511.

[94] Zheng, H. B., Chen, H. H., Wang, Y. L., Gao, P. Z., Liu, X. P., & Rebrov, E. V. (2020). Fabrication of magnetic superstructure NiFe2O4@ MOF-74 and its derivative for electrocatalytic hydrogen evolution with AC magnetic field. *ACS Applied Materials & Interfaces*, *12*(41), 45987-45996.

[95] Chen, J., Ling, Y., Qu, D., Huang, L., Li, J., Tang, P., ... & Xu, Q. (2021). Enhanced electrocatalysis of NiMnIn Heusler alloy films for hydrogen evolution reaction by magnetic field. *Journal of Alloys and Compounds*, *877*, 160271.

[96] DeGroot, H. P., & Hanusa, T. P. (2011). Cyanide complexes of the transition metals. *Encyclopedia of Inorganic and Bioinorganic Chemistry*, 1-13.

[97] Seh, Z. W., Kibsgaard, J., Dickens, C. F., Chorkendorff, I. B., Nørskov, J. K., & Jaramillo, T. F. (2017). Combining theory and experiment in electrocatalysis: Insights into materials design. *Science*, *355*(6321), eaad4998.